University of Modena and Reggio Emilia
Department of Engineering Sciences and Methods
Doctorate School in Industrial Innovation Engineering

RATIONALLY DESIGNED LATTICE STRUCTURE FOR HUMAN CANCELLOUS BONE VERTEBRAL IMPLANTS

A dissertation submitted for the degree of Doctor of Philosophy

Tutor:
Prof. Ing. **Davide Castagnetti**

Candidate:
Andrea Sorrentino

Co-Tutor:
Dott. Ing. **Fulvia Taddei**

Ph.D. Program Coordinator:
Prof. Ing. **Franco Zambonelli**

XXXIII Cycle (2017-2020)

“Per aspera ad astra”

ABSTRACT

This thesis describes the method and the results of the design and experimental validation of a new porous lattice structure for a lumbar vertebral prosthesis. Unstable vertebral body compression fractures, spinal tumors and post-traumatic deformities require a total vertebral body replacement (VBR). The reconstruction of the vertebral segment consists of a spinal arthrodesis, where a vertebral implant, also called cage, is inserted after a total corpectomy in combination with an internal spinal fixation device. Recently developed additive manufacturing techniques allow the production of titanium biomaterials (e.g. gyroid lattice structures) with interconnected porosity which ensures high tissue ingrowth and vascularization. However, these implants show several complications, including a localized contact between prosthetic and vertebral endplates, and higher modulus of elasticity which increases stress shielding and potential subsidence of the cage. In this work a novel porous lattice structure was developed for human cancellous bone vertebral implants. The work focuses on the design and experimental validation of a new 3D printed titanium-based lattice structure, with the aim to develop a porous biomaterial with similar mechanical properties to that of the human trabecular bone. The proposed solution is an innovative meta-biomaterial that consists of a high porous auxetic rotating cubes geometry with negative value of Poisson's ratio. The structural design of this structure is based on an efficient and robust design process, which considers the most critical factors of the vertebral body resection and the lumbar spinal fatigue loading. In order to evaluate the mechanical response of the VBR lattice structure for different rotating auxetic configurations, 2D and 3D finite element models of the system were used. The optimization identified some peculiar configurations of the auxetic lattice system that can reduce the maximum stresses for global strains up to 3%. To assess the structural response of the proposed architecture, we manufactured a prototype in titanium alloy material (Ti6Al4V ELI) through the selective laser melting (SLM) 3D-printing technique and performed a compressive test by measuring the global strain field of the specimen through digital imagine correlation (DIC). The experimental results confirmed the numerical predictions in terms of Poisson's ratio and mechanical properties. By comparing the proposed solution with the actual VBR lattice structures from the literature, it appears a noticeable stress reduction with improved elastic properties combined with an easy manufacturing.

SOMMARIO

La presente tesi descrive il metodo e i risultati relativi alla progettazione e validazione sperimentale di una nuova struttura reticolare porosa per protesi vertebrali di tipo lombare. Fratture vertebrali, tumori spinali e deformità post-traumatiche comportano molto spesso la rimozione del corpo vertebrale danneggiato, nota come *Total Vertebral Body Replacement* (VBR). La ricostruzione della colonna vertebrale consiste in un'artrodesi spinale, dove un impianto vertebrale, denominato "gabbia", viene inserito dopo una corpectomia totale in combinazione con un sistema di fissazione secondario. Tecniche di produzione additiva di recente sviluppo consentono la produzione di differenti strutture trabecolari in titanio ad elevata porosità (ad es. strutture giroidali), in grado di assicurare elevati livelli di fusione ossea e vascolarizzazione. Tuttavia, questi tipi di impianto mostrano numerose complicazioni, tra le quali contatti localizzati tra le placche terminali protesiche e le placche terminali vertebrali, e valori del modulo elastico della struttura molto elevati che aumentano il rischio di ipo-sollecitazione ossea (*stress shielding*) e i fenomeni di subsidenza della struttura. In questo lavoro viene presentata un'originale struttura porosa per impianti ossei vertebrali trabecolari. Il lavoro si focalizza sulla progettazione e la convalida sperimentale di una nuova struttura in titanio in stampa 3D, con lo scopo di realizzare un biomateriale poroso che possiede proprietà meccaniche molto simili a quelle dell'osso trabecolare umano. La soluzione proposta è un'innovativa struttura in metamateriale reticolare biocompatibile composta da una geometria a cubi auxetici altamente porosa che presenta un valore del coefficiente di Poisson negativo. La definizione della struttura ottimale si basa su un processo di progettazione efficiente e robusto che considera le problematiche operative in fase di resezione del corpo vertebrale e le sollecitazioni critiche che agiscono lungo il tratto spinale. Allo scopo di valutare la risposta strutturale del sistema per differenti configurazioni dell'architettura proposta, vengono utilizzati modelli 2D e 3D agli elementi finiti della struttura. L'ottimizzazione identifica specifiche combinazioni dei parametri geometrici della struttura auxetica in grado di ridurre la tensione massima sul sistema per deformazioni fino al 3% della struttura. Al fine di verificare la risposta strutturale della soluzione proposta, è stato realizzato un prototipo della geometria in lega di titanio (Ti6Al4V ELI) tramite la tecnica di stampa 3D a fusione laser SLM, eseguendo una prova di compressione quasi-statica sul provino e monitorando il campo di deformazione globale della struttura con un sistema di correlazione d'immagini digitale (DIC). I risultati sperimentali confermano le previsioni numeriche in termini di coefficiente di Poisson e caratteristiche meccaniche. Confrontando la soluzione proposta con le strutture presenti in letteratura, si nota una notevole riduzione delle sollecitazioni puntuali sul sistema poroso con eccellenti proprietà elastiche in combinazione con una buona facilità di realizzazione.

TABLE OF CONTENTS

This page intentionally left blank

1 INTRODUCTION

1.1 Motivation and research objectives

This work focuses on the design and experimental validation of a new lattice structure for human cancellous bone vertebral implants. The vertebral body replacement (VBR) is the major spinal surgery approach in case of spinal tumors and bone degenerative pathologies [1].

Usually, vertebral prosthetics are produced by additive manufacturing (AM) techniques [2]. The additive manufacturing of prosthetic implants offers a promising route to the development of porous biomaterials with a variety of lattice geometries, which prove a feasible solution for bone reconstruction [3]. This is particularly pertinent in the case of titanium prosthetic implants [4] based on powder-bed methods, such as electron beam melting (EBM) and selective laser melting (SLM) techniques [5, 6]. Specifically, the interbody implant of a VBR, namely cage, was extensively studied in recent years [7].

The internal part of the cage consists of a three-dimensional trabecular geometry with different interconnected porosities [8]. The titanium cage determines the fatigue behavior and the functionalities of the implant, such as the stiffness, porosity and compressive strength, which are crucial to the successful implantation of the device for long bone reconstruction [9, 10]. Most of the works found in literature concerns the design of non-stochastic lattice structure, such as cubic, diamond, rhombic dodecahedron and triply periodic minimal surface (TPMS) structures [11, 12].

A well-known TPMS is the gyroid structure, manufactured using EBM technique, which represents the most used solution as scaffold in vertebral bone implant [13]. The gyroid lattice structures show high values of stiffness (i.e. apparent Young's modulus) and of compressive strength for a porosity in the range from 75% up to 90% [14]. However, the mechanical response of these systems strongly depends on the main direction of the load in the implantation site and by the volume fraction of the unit cell [15]. Specifically, the strut diameter and the angle between the surface of the unit cell determines the deformation behavior of the lattice structure and the peak stress along the nodal points between surfaces [5].

Then, gyroid structures may lead to two different problems: high rate of plasticity and brittle layer-by-layer collapse [13]. In particular, for specific combinations of the trigonometric functions of the gyroids, high plastic strains occur in the lattice system for very low load cases: consequently, prior analyses must be performed to consider the bone area and the spinal segment where the vertebral implant must be placed.

On the other hand, the crack initiation is primarily affected by the load orientation and by the magnitude of the stresses, especially in case of shear loadings and for weight-bearing case. Thus, the stability of whole implant is obtained by enclosing the internal scaffold in a small shell (1 mm thickness), which leads to increased elastic modulus of the system, and subsequently to stress shielding phenomena [16]. Therefore, the titanium cage limits the beneficial bone ingrowth [13].

In addition, the use of 3D printing demands the support of robust design solutions to integrate the structural support function and the regenerative capacity of tissue engineering into a single implant [17]. As shown in literature, vertebral lattice structures fabricated via SLM can reduce the stress concentrations along the scaffold which is responsible of a remarkable fatigue life reduction of this component [18].

The aim of this work is to design, prototype and validate a new porous titanium vertebral lattice structure fabricated via AM in case of large segmental bone defects. The present work has been carried out in collaboration with the *BIC Laboratory* ("*Laboratorio di Bioingegneria Computazionale"*) of the *Istituto Ortopedico Rizzoli* in Bologna.

The design of this new lattice structure takes into account the most critical pre/and post-operative VBR factors, with the aim to develop a minimally invasive and easy to implant vertebral prosthetic, with better biomechanical response in terms of spinal stabilization and fatigue life resistance.

The identified solution consists of a titanium auxetic lattice structure with an improved strain tolerance and with an apparent Young's modulus similar to that of the human trabecular bone [19]. The modelling and optimization of the auxetic system is carried out by employing 2D and 3D numerical models of the geometry with different bio-inspired lattice configurations of the auxetic structure.

The auxetic geometry was manufactured in titanium alloy material through SLM 3D-printing fabrication and experimental tests were conducted.

The proposed solution shows a great potential for three main reasons. First, this new lattice structure allows an overall 3% elastic strain of the system which ensure lower stress concentrations due to normal loads with an increase of fatigue life of the implant. Second, the elastic modulus of the system is similar to the Young's moduli of human trabecular vertebral bones, which allows to reduce the stress shielding phenomena. Third, the proposed solution is flexible enough to mimic the cancellous bone behavior, with great pore size that increase the bone tissue regeneration inside the scaffold. The proposed auxetic lattice structure represents an innovative solution for VBR implant, with the possibility to integrate different type of vertebral shell around the central body, like titanium and/or PEEK systems.

1.2 Thesis outline

The thesis is divided into seven main chapters which are briefly described as below.

Chapter 2 Firstly, the vertebral biomechanics of the spine and vertebral body surgery approach are presented. Secondly, the chapter reports a literature review of the different types of vertebral implants in case of total vertebral body replacement (VBR).

Chapter 3 This chapter presents the systematic approach and the method used to identify new design solutions for the lattice geometry of a 3D printing VBR implant made of titanium alloy.

Chapter 4 The optimal lattice structure configuration of new VBR prosthetic is presented. The chapter describes the concept of rotating auxetic structures as vertebral scaffold.

Chapter 5 The chapter concerns the modelling and the numerical optimization analysis of different 2D configurations of the lattice structure.

Chapter 6 Firstly, the chapter describes the analysis and optimization of novel 3D lattice structure for vertebral implant. Secondly, the mechanical properties of the system investigated are then discussed and the optimal solution is selected.

Chapter 7 In this chapter, the additive manufacture and validation of the new lattice structure is described. Specifically, the results of the experimental tests are presented and discussed.

Chapter 8 General discussion is presented in this chapter. In particular, numerical and experimental results are compared and discussed.

Finally, conclusions are presented in *Chapter 9*.

2 STATE OF ART

2.1 Biomechanics of vertebral bone

2.1.1 Anatomy of the spine

The vertebral column, also called spine or backbone, is a complex structure made up of approximately thirty-three small bones, known as vertebrae, separated by cartilaginous intervertebral discs, which provide both structural and nervous system support for the entire human body, Figure 1.

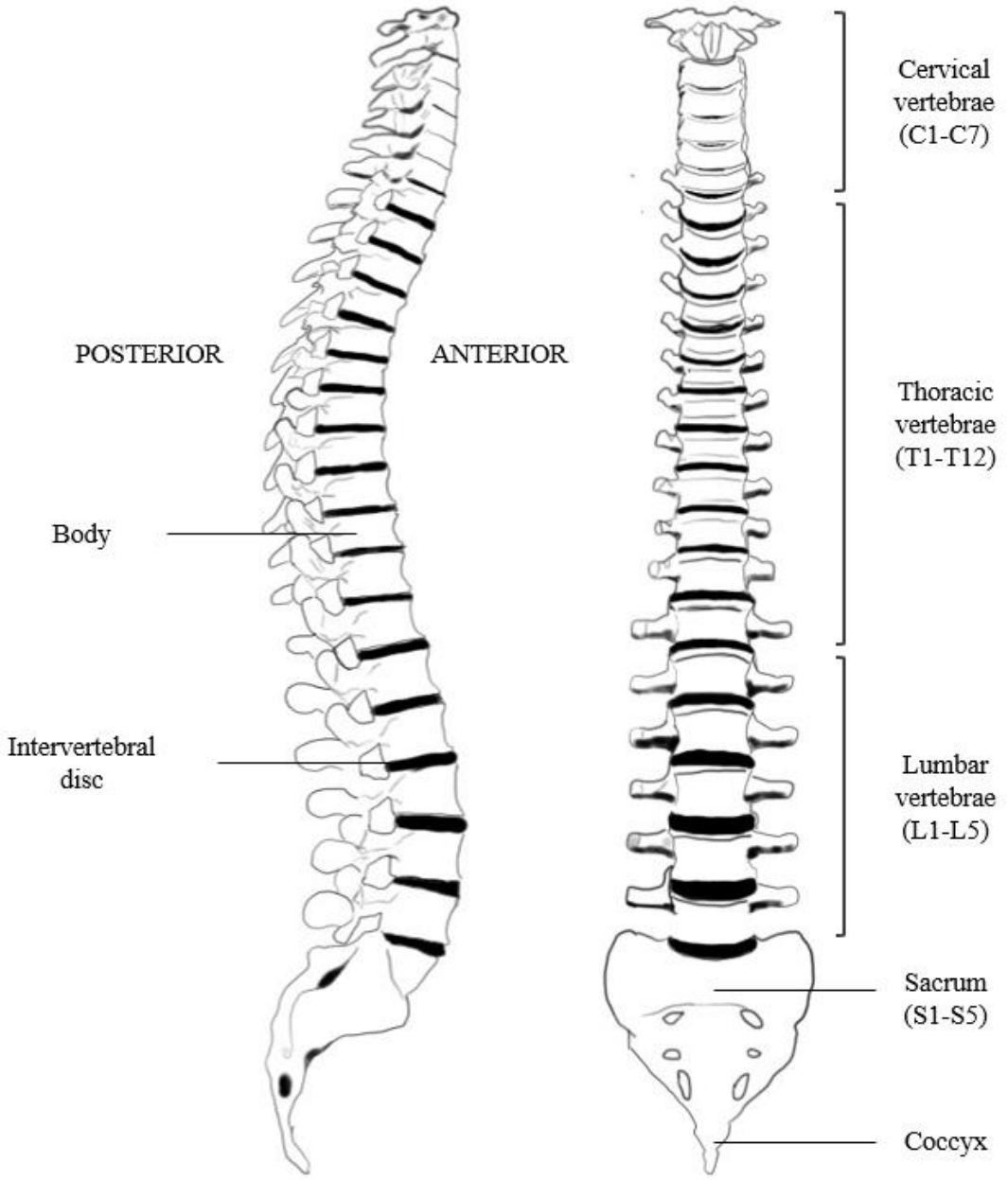

Figure 1 Schematic of the vertebral column.

The vertebral column has three fundamental physiological functions [20]. First of all, it protects the spinal cord from potentially damaging motions. In addition to that, it transfers body weight and the resultant bending moments to the pelvis. Finally, it allows physiologic motions between the head, trunk and the pelvis by providing stiffness for the body and the attachment for the pectoral and pelvic girdles and any muscles.

The spine can be separated into five different regions, each one region characterized by a different vertebral macro-structure. In particular, the spine consists of seven cervical vertebrae, twelve thoracic vertebrae, five lumbar vertebrae, five fused sacral vertebrae, and three to four fused coccygeal segments, Figure 1.

However, all vertebrae share a basic common structure. Specifically, each vertebra consists of a vertebral body, or centrum, situated anteriorly, and of a posterior Y-shaped vertebral neural arch (see Figure 2).

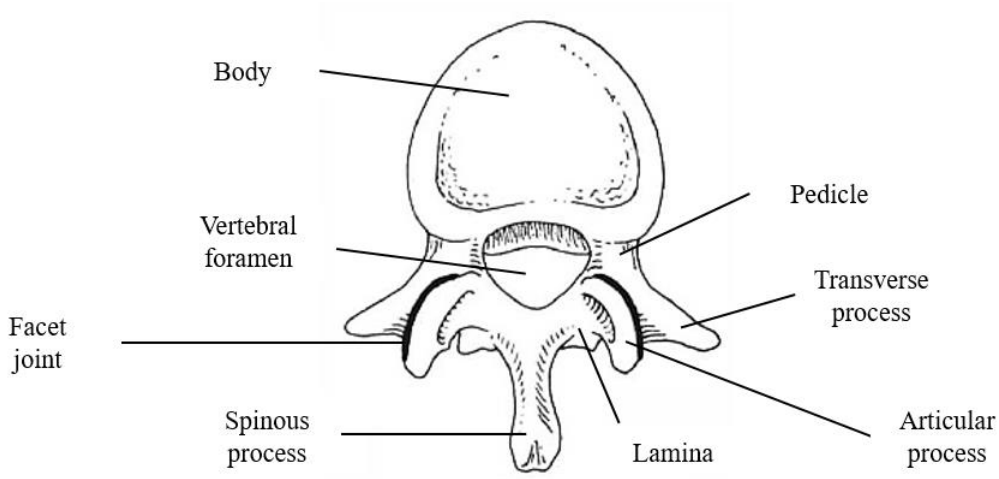

Figure 2 Superior view of lumbar vertebra.

The centrum is a roughly quasi-cylindrical mass of cancellous bone contained in a thin shell of cortical bone. The vertebral body represents the weight-bearing component of the vertebra, and its size increases as the as the vertebral column descends to accommodate the increasing body weight [21].

As shown in Figure 2, the vertebral arch extends a single spinous process downward and backward, a paired transverse process, one to either side, and the articular processes, superior and inferior, which articulate with the articular processes of the vertebrae above and below. In the thoracic vertebrae, the transverse processes articulate with the ribs.

Additional bony prominences are: the lamina, which represents the bone conjunction between the transverse and the spinous process; and the pedicles, which posteriorly meeting the flatter laminae (see Figure 2). With the vertebral body, the vertebral arch surround an opening, called the vertebral foramen (or spinal canal), which encloses the spinal cord and the nerve roots.

In the lateral, or sagittal plane, the vertebral column is characterized by four normal curves: convex anteriorly in cervical and lumbar regions and convex posteriorly in the thoracic and sacral segments (see Figure 1).

To maintain its double S-shape curve, whilst simultaneously maintaining adequate stiffness and stability at the intervertebral joint level, the vertebral column relies on a number of supports and ligaments structures.

First, the spinal discs, called intervertebral discs. These discs act as interbody spacers and shock absorbers. They are similar to a fibrous pad of tissue, called fibrocartilage, and anchored in place by vertebral end-plates. The intervertebral discs consist of three distinct parts: the nucleus pulposus, the annulus fibrosus, and the cartilaginous end-plates, Figure 3.

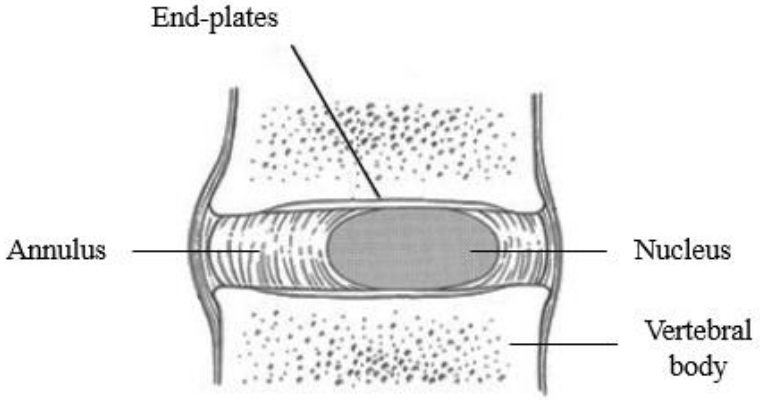

Figure 3 Intervertebral disc.

Second, each vertebra presents articulations which also forms a joints. The vertebral bodies indirectly articulate with each other, and the articular processes also form joints. The vertebral body joints are cartilaginous joints, covered by hyaline cartilage on the surfaces and connected by a vertebral disc. The joints between the articular facets are called facet joints, which are paired, left and right side, at the back side of the vertebral body from C3 to L5 (see Figure 1 and Figure 2).

These joints stabilize the spine while allowing gliding motions between the vertebrae, such as flexion, extension and twisting movement.
Third, various spinal ligaments connect the vertebrae, discs and facet joints, that acts like stretchy-like tension cords in order to stabilize and support the spinal column.
In addition, there are two ligaments that strengthen these joints, the anterior and posterior longitudinal ligaments. Spinal muscles and tendons regulate and stabilize the vertebral column while limiting extreme movements.

2.1.2 Vertebral bone structure

Vertebral bones are a specialized highly heterogeneous tissue with a complex microstructure and an optimum mass-to-strength ratio. The calcified vertebral bone matrix is composed by two different part: the organic matrix and the mineral substance. The physiological properties of vertebral bones are dependent from the presence of non-osseous structures such as blood vassels and nerve fibers. Bone structure and properties vary so much across individuals and over time and with disease [22].
Design of orthopaedic implants for the vertebral column is particularly challenging because vertebral trabecular bone is so weak and the cortices are so thin, in view of their different microstructures and mineral densities [23].
Vertebral bones have a hierarchical structure. As mentioned above, the vertebral segments consist of an outer layer of compact bone, namely cortical bone, and an inner zone, defined as medulla, which contains bone marrow, Figure 4. The medulla mostly consists of a frame of porous, irregular and spongy tissue material, namely trabecular or cancellous bone [21].

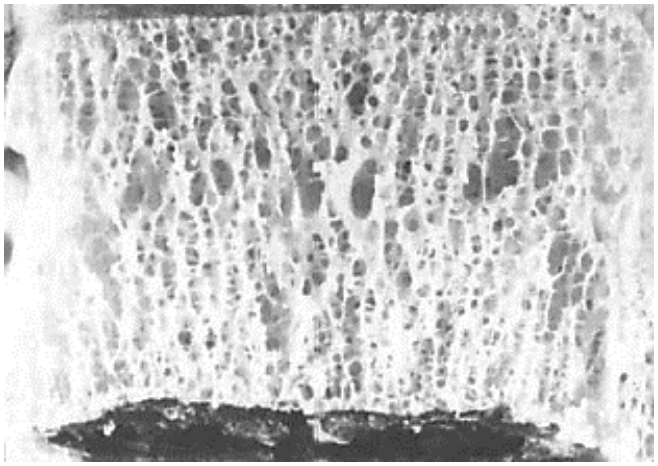

Figure 4 Longitudinal section of the body of a lumbar vertebra [20].

The area covered by the medulla is much greater than the covered by the cortical bone. The cortical bone is structured in three main concentric systems: an outer circumferential system, an intermediate osteonic area, and an inner circumferential system.

2.1.3 Mechanical behavior of vertebral bone

Determination of the biomechanical behavior of vertebral bones is also required in order to design robust implants. The strength capacity of the cortical shell is a controversy research topic [24]. However, recent literature suggest that the cortical shell may take a significant portion of the spinal loads, but the trabecular centrum seems to take the most load close to the end-plates [25, 26]. Furthermore, the spongy bone of vertebrae shows interesting properties.

The microstructural struts, or trabeculae, are the fundamental units of the cancellous vertebral bone. The cancellous bone can be seen as a 3D interconnected open porous system with random architecture composed by horizontal and vertical trabeculae which joining the two end-plates of the vertebral body, Figure 5.

Figure 5 Volume rendering of human vertebral trabecular bone [23].

The scale of the pore is in order of 1 mm, and the trabecular thickness is about one order of magnitude lower [23].

However, the connections and the orientation of the trabeculae are found to have precise patterns which are related to specific mechanical properties and to the principal direction of loading [27].

The spongy bone of vertebrae undergoes large compressive deformations before to fail [28].

By contrast, the recent work of Kopperdahl [29] shows that fracture in trabecular bones occur at strains of about 1.5% for tensile loading, Figure 6.

As shown in Figure 6, the behaviors in tension and compression are different, especially in the post-yield regions.

Clearly, the structural heterogeneity of vertebral bones affects its mechanical properties, such as strength, elasticity and stiffness.

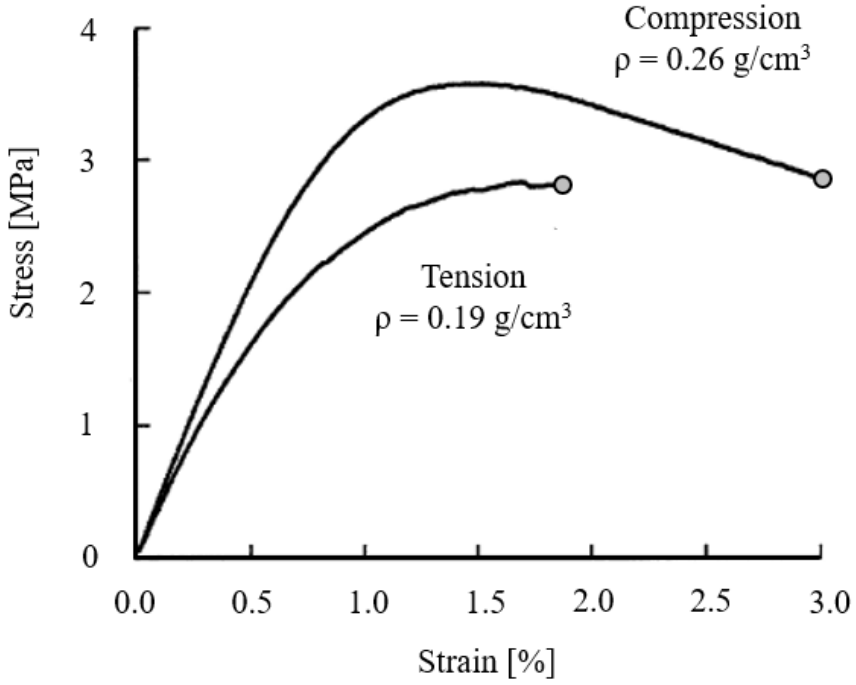

Figure 6 Typical tension and compression stress-strain curves for two vertebral trabecular bone specimens of different apparent density (ρ) [29].

In particular, the mechanical properties of vertebral bones can be related to its component phases, which are different between them at the various levels of hierarchical structural organization [30]. These properties include cortical and cancellous bone at the level of whole bone, defined as macro-structure level. Structural properties are important for global stress analyses, while material properties are important for characterizing various bone pathologies, micro-level stress analyses, and bone adaptation around implants.

Thus, the following two main issues must be address:

- The determination of the elastic modulus of vertebral segments;
- The evaluation of spinal loads acting on the vertebral body considered.

2.1.4 Elastic modulus

The elastic properties of vertebral body are obtained through numerical simulations, *in vitro* and/or *in vivo* measurements, and with inverse methodology techniques [30, 31].

In cortical bones, the mechanical properties are influenced by the porosity, the mineralization level and by the structural organization of the solid matrix. The mechanical properties of cortical bone depend on loading directions of the testing method. However, it is not possible to assess the mechanical properties of the vertebral cortical bone *in vivo* because the cortical thickness is below the resolution of the medical imaging capability [19]. In this sense, the majority of the work found in literature concerning the estimation of the elastic modulus of vertebral cortico-cancellous bone through computational models obtained from computed tomography (CT) scan, Figure 7.

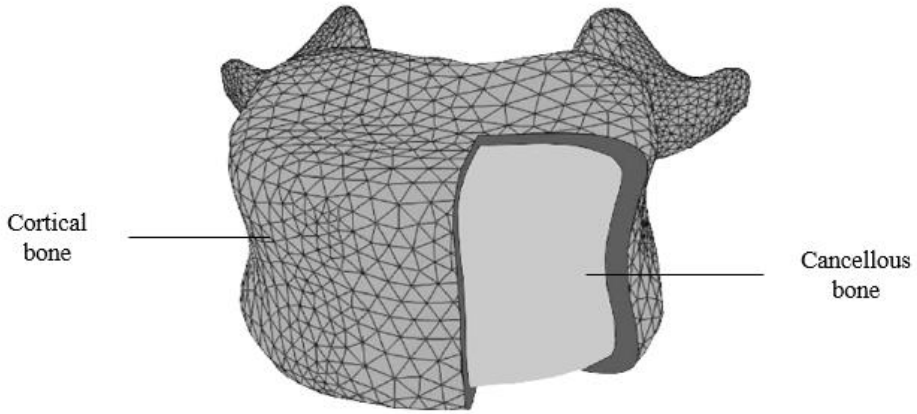

Figure 7 Finite element (FE) model of a lumbar vertebra [32].

Despite this, the mechanical properties of cancellous vertebral bone were extensively studied in the last years [33, 34].

The elastic modulus of the spongy bone is commonly measured by compression, tensile, or bending tests. As mentioned in Kurtz [23], the elastic modulus, namely apparent Young's modulus, can vary by more than an order of magnitude, from as low as 50 MPa to over 700 MPa. These different properties can occur in different portions of the vertebral body, or in relation to aging and pre-existent diseases of the individual considered. There is a strong correlation between the mechanical properties of cancellous bone, both for strength and stiffness, and its apparent density and mineral (or ash) density.

This heterogeneity is a key concept in trabecular bone biomechanics.

2.1.5 Spinal loads

In order to prevent damages in vertebral bones, the knowledge about spinal loading is required for designing and preclinical testing of spinal implants. Damage refers to the reduction in vertebral strength and stiffness due to static and cyclic loading conditions which involve the loss of modulus, indicating the presence of micro-fracture mechanisms.

Apart the fatigue behavior of vertebral body under cycling loading conditions, the recent works found in literature focused on the estimation of the spinal loading acting at the various vertebral segments [35]. Most of these works are based on measurement of *in vivo* changes of the intradiscal pressure [36], body height or forces and moments transmitted *via* instrumented vertebral implants [37]. However, computational models have been employed to estimate the muscle forces and spinal loads under different static and dynamic conditions [38–40].

Of particular interest is the recent work of Han *et al.* [41] which investigates the magnitude of spinal loads for different postures and activities by employed a validate musculoskeletal model of the thoracolumbar spine for various combinations of body height and weight. The body height considered in this study varies from 150 cm to 200 cm, and the weight from 50 kg to 120 kg.

From the work of Han, it comes that the resultant forces have a nearly linear increase with body weight, and a similar trend is observed in all the spinal levels for all the activities considered. On the other hand, changing in the body height produced only small changes to the spinal loading.

Moreover, the resultant moments were largely influenced by simultaneous increases to body weight and body height, but not all the spinal level considered showed an increased in the joint moments.

In summary, Table 1 reports the maximum force and moment for the different tasks and body features investigated by Han [41].

Table 1 Maximum force and moment acting on the spine [41].

	Resultant	**Activity**	**Level**	**Weight** [kg]	**Height** [cm]
Maximum force [N]	1888	Flexion	L5	120	150
Maximum moment [Nm]	16	Extension	L5	120	200

2.2 The vertebral body replacement

2.2.1 Vertebral resection and reconstruction

Total vertebral body replacement, also known as VBR, is generally practiced as a treatment for primary and metastatic spinal tumors and highly degenerative diseases with the aim to provide immediate stability [42, 43]. The spinal stabilization of the anterior vertebral segment injured is carried out after an en bloc resection of the whole vertebral body and adjacent intervertebral discs and necessitates of reconstruction.

Restoring support to the spine includes autograft bone such as iliac crest or rib, allograft bone such as femoral shaft, and static and expandable titanium interbody cages [7, 44].

Specifically, interbody cages are spinal implants consisting of a small hollow cylindrical or oval-shaped device with perforated thin shell around it [45]. Various implants are available in the operative treatment of spinal tumors and in the correction of malalignment and the stabilization of pathological fractures [46]. These implants are made for example of titanium, ceramic material and carbon (see Section 2.3 and Section 2.4).

The complete stabilization can be achieved by additional anterior plating or posterior stabilization by a rod and screw transpedicular fixation system, Figure 8.

Figure 8 Radiographic image of titanium VBR cage with an internal fixator [47].

Alternatively, a direct fixation of the cages with fixation wings is possible, a combination of two systems in one-cage and fixation system. However, posterior stabilization with an internal fixator is seen as a standard by most authors [48].

Anyway, expandable and non-expandable cages have gained acceptance for replacement of the vertebral body. Ideally, a VBR system should be stable, resist axial load-bearing, have a large interbody-bone interface to facilitate fusion and prevent migration, and restore height and sagittal alignment [49]. In addition, VBR cages should provide an optimal mechanical and biologic environment for fusion with the double aims to: first, reduce stress-shielding phenomena; second, to increase the bone ingrowth between bone-implant interface.

In this context, several surgical methods are described in combination with different fixation devices [50], but limited evidence exists regarding one being superior to another [51]. Especially in patients with neoplastic events, it is not important to achieve solid bony fusion, and there is a considerable risk of pseudarthrosis, implant settling and loosening [52].

The unique nature of spinal surgery makes complication assessment difficult.

2.2.2 Complications and critical factors in vertebral resection

2.2.2.1 Clinical aspects

En bloc resection of the whole vertebral body in a single piece is a challenging topic, still debated, in spine surgery literature [47]. In some cases, i.e. in chondrosarcoma, the resection includes the removal of adjacent vertebral bodies. Removal of one or more vertebral bodies followed by spinal column reconstruction continues to evolve. In oncologic events, the length of the resected specimens varies from 33 mm up to 77 mm, but strongly depend on the nature and by the extension of the neoplasia treated [47]. In this specific case, the aim of the surgery is to obtain a tumor-free margin that has proven the to be the major factor affecting long-term survival of the patients. This surgical treatment, together with chemotherapy and radiotherapy (RT), is an effective procedure for the treatment of primitive spine tumors.

Preoperative and postoperative radiological scans available were used to determine the height correction attained, restoration of sagittal alignment and subsidence of the vertebral implant. Modern surgical procedures employ more sophisticated techniques, which permit vertebral body removal from the anterior column and subsequent reconstruction [7].

Regarding surgical techniques, the side of the approach was chosen according to the vertebral level and the location of the replacement [53].

Sufficient stabilization depends on adequate anterior column reconstruction and by the typology of resection performed on the patient.

Correct positioning of the cages can be challenging. Accurate positioning of the anterior and posterior stabilizing implants is required to prevent secondary dislocation of the implant, especially in the use of expandable vertebral prosthetics. Some distraction forces and shaping of the endplates may be necessary to insert a rigid implant. However, clinical and radiological mid-term results have not shown any significant advantages compared to the implantation of non-expandable vertebral body replacement systems, allogenous or autogenous bone grafts [54].

Each reconstruction option is associated with its unique benefits and challenges.

2.2.2.2 Cage failure

One of the main complications of the VBR surgery is postoperative subsidence and collapse of the vertebral implant into the adjacent vertebral bodies [55], Figure 9.

Figure 9 Image of a titanium mesh cage with subsidence and fracture in adjacent vertebral bodies [55].

Despite the lack of evidence, three main factors responsible for VBR cage subsidence have been highlighted by literature [56, 57]:

- Excessive insertional force of the vertebral implant *in situ* replacement;
- Osteoporosis of adjacent vertebral bodies;
- Points of contact between prosthetic endplate and vertebral endplate.

Consequently, the creation of mismatch between prosthetic and bone endplate sometimes plays a role in catastrophic VBR subsidence, which leads to point contact that will strong decrease the ability of the bony vertebrae to resist of the prosthetic endplates.

Even then, the position of the implant can be inadequate, endplates can weaken with consequent subsidence, and restoring sagittal alignment can be insufficient.

Thus, the ability of the prosthesis/bone interface to resist vertebral loading is paramount to the successful implantation of any of the vertebral implants.

This fact highlights the direct relevance to fields such as tissue engineering in which the ideal goal would be to replace damaged trabecular bone with a substitute having appropriate mechanical properties specific to that individual considered [23].

2.2.2.3 Rods and screws failure of posterior internal fixator

Generally, in VBR, the prosthesis is connected to the posterior pedicle screw-rod fixator by a screw-rod connector system adjustable in length and orientation and positioned in the same space of each removed pedicle (see Figure 8).

Different internal fixator systems are available, that are composed of pedicle screws, setscrews, rods and connectors which exhibits different biomechanical behaviors [58].

As for vertebral cages, posterior internal fixation systems are continuously subject to static and dynamic loads during their life.

Under specific conditions, the instrumentation (rods and pedicle screws) should loosen and moves from their original positions and or even break [59], Figure 10.

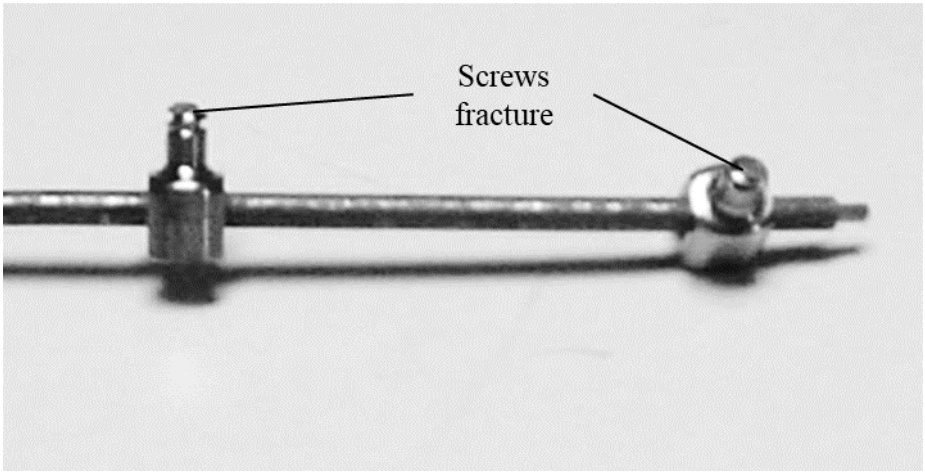

Figure 10 Typical fracture of screws in VBR.

The biomechanical performance of spinal fixator systems is directly affected by the properties of spinal rods, i.e. yield strength, stiffness and fatigue properties of screws. But even so, the most common in mechanical failure clinically is at the lower screws. The points of failure, i.e. points of maximum stress, are generally located at screw rod junction and between the tip of the screw and the rod. On the other hand, the rod diameter is a critical factor: maximum stress value decrease at the diameter increase. Furthermore, using a spinal fixation device may induce stress shielding in vertebral body, which refers to the reduction in bone density as a result of removing the typical stress from the bone by an implant [60]. In summary, the surgeon should attempt to distribute loads in a way that not a single portion of the vertebral implant or spine carries an excessive portion of the compressive load which acts on the spine.

2.3 Biomaterials and advances in spinal implants

2.3.1 Common biomaterials in spine surgery

The design of vertebral cages and implants in spinal surgery has undergone a dramatic evolution over the past 30 years from stainless steel to 3-dimensional (3D) printed metallic cages and expandable implants [61]. Various biomaterials for spinal implants are used in the reconstruction of the spine, which are briefly summarized in Figure 11.

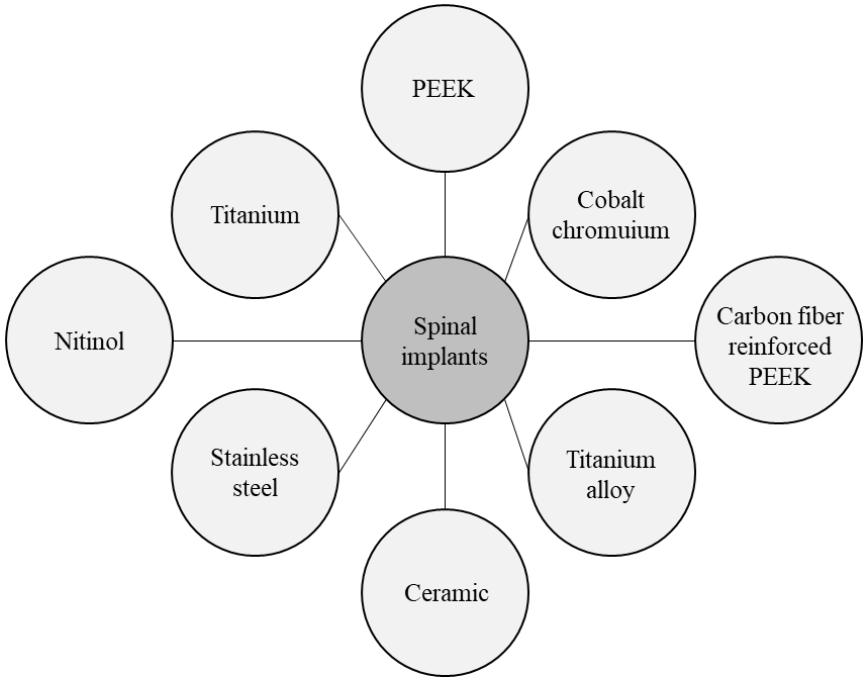

Figure 11 Common biomaterials used in spine surgery.

The materials that have been most commonly used include stainless steel, titanium and titanium alloys (i.e. Ti6Al4V) and polyetheretherketone (PEEK), which have different stiffness and mechanical properties, see Figure 12.

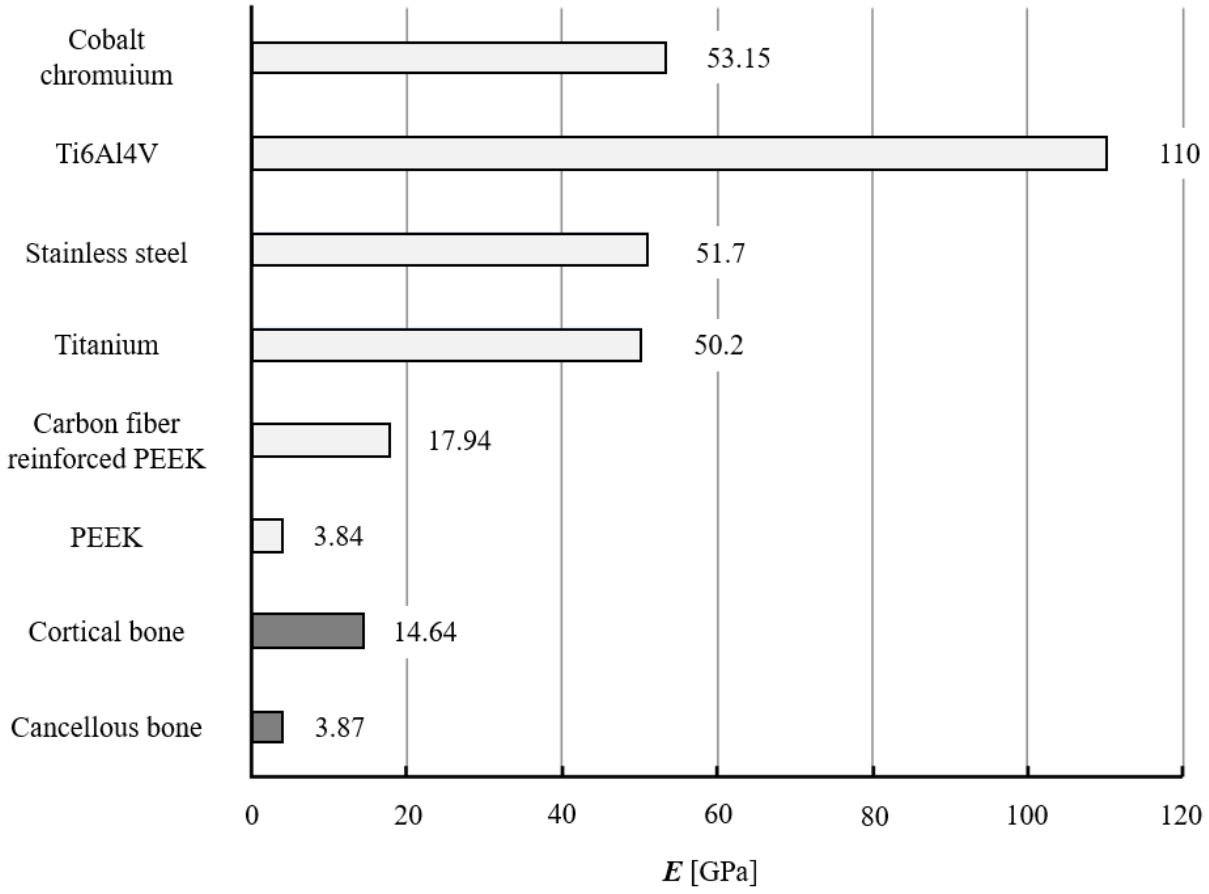

Figure 12 Elastic modulus (*E*) of common biomaterials compared to femoral cancellous and cortical human bone [61].

Required properties of biomaterials for general vertebral implant are the following:

- Biologically inert/biocompatible;
- An elastic modulus (Young's modulus) similar to that of the bone were it is implanted;
- High stiffness and fatigue strength;
- Low artifacts on scan imaging.

Thus, advanced technologies and materials are employed in spinal surgery with the double aim of meet the needs of the surgeons and to improve the biomechanical response of devices.
Specifically, for posterior internal fixator, the most commonly used materials are titanium and PEEK.

The use of titanium in secondary fixation systems increases the biomechanical response of the system with an improved biocompatibility and improvements of the stress shielding of lumbar pedicle instrumentation [62]. In addition, titanium alloys were chosen because they are protected from corrosion.

However, clinical performance, implant cost and fixation easiness are some parameters which are being considered by the surgeon [46].

Details on biomaterials of interbody cages are presented below (see Section 2.3.2).

2.3.2 Requirements and characteristics of biomaterials in interbody cages

The cages are typically made of metal, such as titanium (Ti) and titanium composite/alloys; usually bioinert polymers and similar.

Actually, most commonly used biomaterials for the interbody cage are titanium alloy Ti6Al4V and PEEK. Advantages and disadvantages of these two biomaterials are summarized in Table 2.

Table 2 Characteristics of titanium and PEEK biomaterials for interbody cages.

Materials	Pros	Cons
Titanium and its alloy	Biocompatible High Young's modulus Strong Flexible Lightweight	Relative expensive Some artifacts on imaging
PEEK	Biocompatible Lightweight Flexible Low cost Low artifacts on imaging	Low Young's modulus Some grafting issues

Titanium has a superior biocompatibility and Young's modulus compared to stainless steel (SS) and cobalt counterparts (see Figure 12).

On the other hand, PEEK has similar elastic modulus compared to bone (see Figure 12), and superior radiographic properties that allow surgeons to monitor possible migration of the implant.

PEEK has a significantly lower stress compression strength compared to titanium [63].
Then, requirements for biomaterials in vertebral interbody are the following:

- Optimal mass-to-strength ratio;
- High porosity (both internally and externally of the cage);
- Appropriate Young's modulus.

In order to meet specific requirements and surgeon guidance, hybrid Ti-PEEK vertebral cages were develop using 3D printing technologies.

2.3.3 Advances in spine surgery: 3D printing technologies

The additive manufacturing (AM), or three-dimensional printing (3DP), is an additional option for the spine surgery reconstruction. The 3D-construct is obtained through deposition of raw materials, or fused and/or melted, based on the material/design specifications [3].
3DP technology have been adopted for different applications, such as implantable devices and patient specific interbody cages [64, 65], Figure 13.

Figure 13 Three-dimensional printed titanium VBR [66].

General advantages and disadvantages of 3DP technologies in spine surgery are reported in Table 3.

Table 3 Advantages and disadvantages of 3DP technology for vertebral implants.

Advantages	Disadvantages
Precise implants shapes High porous lattice structure Better postoperative results Improved mechanical properties	Possible deviation between computer 3D model and the physical object Complex surgical procedure during the positioning of the implant High cost

The design of interbody implants and prosthetics starts on preoperative computed tomography (CT) considering shape and length of the bone loss produced and the resection defect.
Based on these data collected, the customized model of the implant can be fabricated using different fabrication techniques, such as:

- Electron beam melting (EBM);
- Selective laser melting (SLM);
- Direct metal laser sintering (DMLS).

Each technology option is associated with its unique benefits and challenges.
Titanium alloy Ti6Al4V is the most used materials in vertebral cages, but one study used PEEK [3]. Patient specific (PS) implants made of titanium alloys were implemented in all spine divisions: from sacral to cervical segment, especially in case of neoplasia and degenerative diseases. A significant component of the efficacy of PS implants was attributed to the customisation of the interbody cage surface topography to mimic the morphology of adjacent vertebral endplates [17].Osseointegration through bone ingrowth and ongrowth and adequate stiffness can be obtained using optimized lattice structure with different architecture. On the other hand, laser sintering (SLS) and fusion deposition method (FDM) are used for produce biopolymers and plastics components for the vertebral implants [67].
However, there is an increased research effort towards the 3DP biodegradable scaffolds using polyurethane to mimic the elasticity of vertebral bodies. Currently, titanium represents the most efficient solution in spine surgery, especially in the case of VBR.
Details on 3D-printed titanium-based lattice structures for vertebral cages are presented in Section 2.4.3.

2.4 Vertebral prosthetics

The section briefly describes the different types of interbody devices for vertebral reconstruction, with particular attention to the 3D-printed vertebral implants made of titanium.

2.4.1 Mesh cages and expandable implants

At first, vertebral implants consisted of a non-expandable titanium mesh cages, or *MOSS* systems, Figure 14.

Figure 14 Mesh cage made of titanium (Ti) [68].

Titanium mesh cages, namely *Harms* cages, were developed in order to eliminate the need to autogenous tricortical bone grafts. In addition, using PMMA cylinders equivalent load transmission can be reached, but there also exists a great dislocation tendency among those implants [68]. However, optimal placement of a non-expandable spacer can be demanding and challenging. Subsidence of the mesh cage into the vertebral body may also cause serious problems, such as recurrence of the spinal deformity or fusion failure [69].

In an attempt to overcome the technical problems of non-expandable cages, various expandable cages have been developed that can be adjusted *in situ* to the height of the corpectomy defect and spinal tumors. Several expandable cages, or vertebral distractor, can be traced in literature made of different materials, like Ti and PEEK. In particular, one of the most used system is the *Synex* vertebral interbody made of titanium [70], Figure 15.

Figure 15 *Synex* vertebral distractor [70].

The potential advantages of the expandable titanium cage (ETC) include the ability to use the implant to correct sagittal alignment, restore vertebral height, as well as ease of use.
Despite this, long-term subsidence of the cage into the vertebral body leading to instrumentation failure has been reported with the use of expandable cages [71]. Among the other problems encountered by the use of this plant we mention [72]:

- Poor bone-implants interface and bone ingrowth;
- High stiffness of the device implanted;
- Bony fractures of adjacent vertebral bodies;
- High stress concentrations on vertebral end-plates.

Then, critical aspects and intra/post-operative complications must be evaluated on the use of these devices.

2.4.2 PEEK interbody cages

PEEK cage is a good alternative to classic Ti expandable cages in case of VBR, Figure 16. This type of devices have a significantly lower loss of Cobb's angle [20] and lower cages subsidence rate compared to titanium ones [73].

Figure 16 PEEK expandable cage with modular elements [73].

PEEK devices have shown other superior abilities such as [74]:

- Young's modulus similar to that the cortical bones;
- High radiolucent rate;
- Good intraoperative applicability and individual adaptability.

Similarly, an improved version of this implant is the carbon fiber reinforced PEEK (CFRP) system [75].

However, it is not possible to obtain the same biomechanical performances of that metallic implants ones with this type of polymers.

2.4.3 3D-printed titanium implant

2.4.3.1 The biomimetic 3D-printed custom made vertebral prosthesis

Reconstruction of anterior column after en bloc resection in the thoracolumbar spine can be performed using custom made metallic prosthesis made of titanium alloy Ti6Al4V, Figure 17. This type of prosthetic is the same implanted at the *Istituto Ortopedico Rizzoli* of Bologna (Italy) [47]. The design of this implant is obtained from CT scan images which are used to generate the CAD model and the finally construct which will be realized through AM.

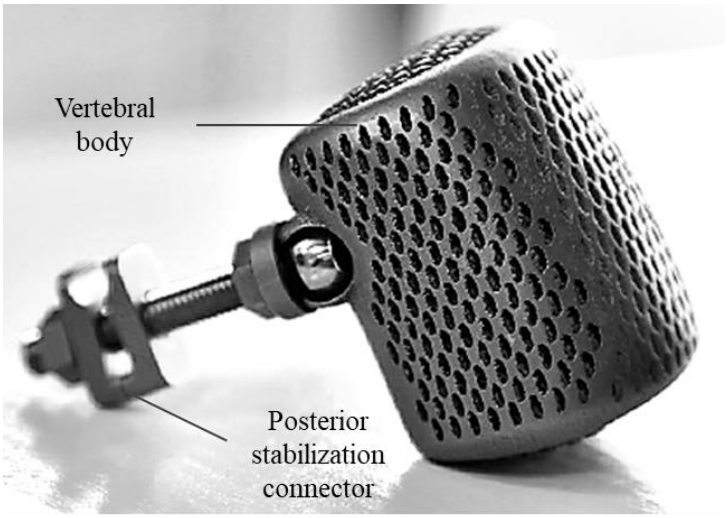

Figure 17 Biomimetic titanium cage [47].

As shown in Figure 17, the vertebral body of this prosthetic is composed by two main parts:

- An innermost 3D porous lattice structure that mimic cancellous bone;
- An outer porous thin shell that mimic the cortical bone.

The shape of the construct is very similar to the original framework of human vertebra of the spine segment considered.

The prosthesis is produced through EBM technology at a public research center [14].

Moreover, the prosthesis is connected to the posterior pedicle screw-rod instrumentation made of Ti by a screw-rod connector system adjustable in length and orientation and housed in the same space of each removed pedicle, Figure 18.

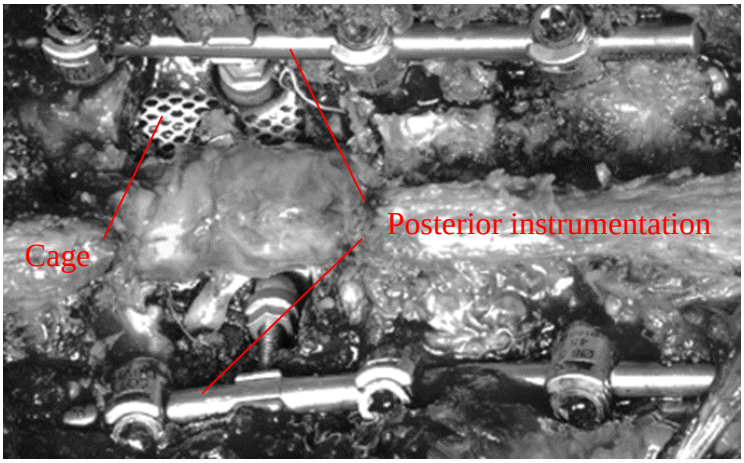

Figure 18 Resection and reconstruction of lumbar segment with biomimetic cage and posterior instrumentation.

Generally, the duration of the reconstruction varied from 18 to 68 min.
Benefits and disadvantages of this type of implants are reported in Table 4.

Table 4 Advantages and disadvantages on the use of biomimetic titanium cage.

Advantages	Disadvantages
	High insertional force required
Biocompatible	High stiffness of the structure
Patient-specific implant	No deformation admitted on vertebral body
High porous system	No fatigue life information available
Absence of postoperative complications	Possible subsidence of the cage
	Monolithic system due to outer shell

Up to now, the clinical follow-ups of this type of surgery have not revealed any neurological complications.

2.4.3.2 Lattice structures in VBR

Actual therapies in VBR may be improved with regard to certain characteristics such as stability, functionality, durability, costs and osteointegration, especially in cases of low bone quality [76].
AM techniques have the main advantages to manufacture interconnected porous biomaterials with predictable and predetermined unit cells (lattices structures).
In this sense, the use of specific lattice structures for 3D-printed titanium cages has the following aims:

- Increase the tissue ingrowth and vascularization;
- Mimic the behavior of the spongy bone;
- Obtain a mechanical properties similar to those of human bone (i.e. Young's modulus);
- Reduce stress shielding phenomena.

Thus, a variety of works can be found in literature for biomedical applications in order to optimize designs [2, 8, 77].
The current trend in vertebral joint replacement is to fabricate non-stochastic lattice structures with different interconnected porosity, such as cubic, diamond, rhombic dodecahedron and triply periodic minimal surface (TPMS) structures [11, 12].

In particular, one of the most studied TPMS structure for VBR lattice structure is the gyroid scaffold, Figure 19.

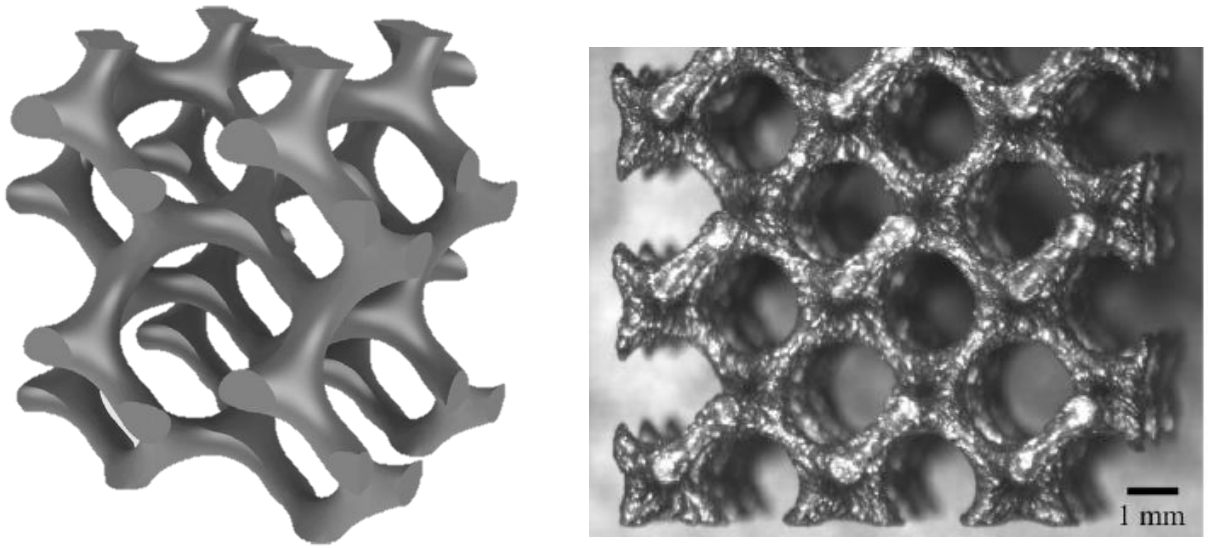

(a) (b)

Figure 19 Gyroid structure [5]: CAD model (a) and manufactured scaffold via SLM (b).

Normal and modified gyroids fabricated *via* EBM have been investigated as a versatile solution for human cancellous bone vertebral implant [12–14, 76], and implemented in the design and fabrication of the above presented biomimetic titanium cage implanted at *Istituto Ortopedico Rizzoli* (see Section 2.4.3.1). These type of structures show high values of elastic modulus and of compressive strength for different values of porosity in the range from 75% to 90% [14].

However, its mechanical behavior is strongly affected by the AM process and by the direction of loading acting on the scaffold. Additional critical aspects and complications associated to gyroid produced via EBM are the following:

- High peak of stresses located at nodal points;
- Excessive elastic modulus in some configurations (high stiffness);
- Low elastic deformation of the scaffold;
- Brittle fracture events;
- Increased stress shielding phenomena along adjacent vertebral end-plates.

In short, the design and the optimization of lattice structure in vertebral bone defects still remain as a challenge.

2.5 Concluding remarks

Critical aspects and general considerations about vertebral body replacement, which are helpful for the design process, are summarized as follows:

- Vertebral bones are complex structure showing anisotropic mechanical behavior. A specific assessment of the mechanical properties for the vertebral segment considered is necessary;
- Under certain assumptions, i.e. in the macro-scale, vertebral bones showed general characteristic and mechanical properties;
- Vertebral body replacement (VBR) represents the most common surgical procedure adopted in case of primary spinal tumors and hard degenerative diseases;
- Clinical and design aspects must be considered in VBR surgery;
- Advanced 3D printing technologies and biomaterials can support the role of the designer and of the surgeon;
- Titanium alloy cage systems produced *via* additive manufacturig represents the most popular solution used as VBR;
- Lattice structures reveal crucial aspects: meet patient-specific solutions and biomechanical features is a complex asset;
- New design solution must be considered in order to improve fatigue life of the implants and the biomimetic of the actual devices.

3 THE CONCEPTUAL DESIGN OF VERTEBRAL STRUCTURE

3.1 Planning for the design and development

In this work we rationally design and experimentally validate a novel lattice system for lumbar vertebral interbody cages which mimics the spongy behavior of human vertebral bones.

The work aims to develop an optimize mechanical system with desired combination of biomechanical and tissue regeneration properties in order to avoid the major limitations of the actual trabecular scaffolds.

Since the gyroids structure and others bio-structures are mainly used for bone defect reconstruction, the work reveals that new porous lattice system with conventional and unconventional specifications can be designed to exhibit specific mechanical properties and advances functionalities.

The design process of this new mechanical object consists of three macro-steps, which are summarized as below (see Figure 20).

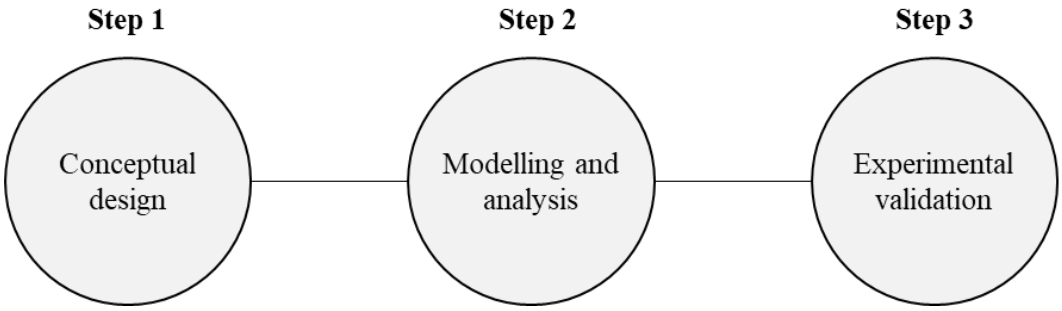

Figure 20 Main steps for design and development new VBR lattice structure.

Specifically, this chapter focuses on the conceptual design of a new lattice structure for a titanium vertebral prosthesis ("*Step 1*" in Figure 20).

The chapter discuss the methodology and the employed design concepts which allow to generate new innovative solution based on the critical factors related to lumbar VBR and titanium interbody implants. Then, the chapter presents the final concept selected for the design of a new lattice structure for vertebral prosthetics.

In particular, the method intends to exploit the use of three main types of knowledge: first, knowledge to structure the design process; second, knowledge to generate ideas; and third, knowledge to evaluate ideas and make decisions [78].

3.2 The conceptual design process

Designing new porous VBR lattice structure regards certain techniques that can be used during the design process to help ensure satisfactory results. This design is based on the mechanical design methodology presented in the works of Ullman [78] and Dragoni [79].

Specifically, the main steps of the conceptual design method implemented in the work are outlined as in Figure 21.

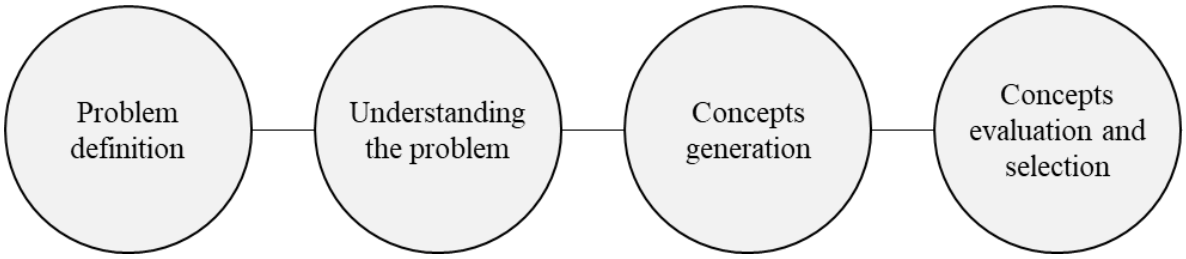

Figure 21 Schematic of the conceptual design method implemented.

As shown in Figure 21, efficient product design requires planning for the process to be followed. Specifically, general conceptual design starts from defining the system and the objectives of the design (the "*Problem definition*" section).

Hence, engineering specifications are evaluated (the "*Understanding the problem*" section). Techniques for generating new concepts are then presented (the "*Concepts generation*" section). Finally, evaluation and selection of new concepts are presented and discussed (the "*Concepts evaluation and selection*" section). These represent the crucial phases in the development of a product, since the decisions made here affect all the downstream phases.

However, specific considerations and issues about the single steps are presented in the corresponding sections.

3.3 Problem definition

3.3.1 Product proposal

The design process starts with the definition of the product proposal [79].

In particular, we define the mechanical device under investigation, the desired outputs and constraints of the system.

For this aim, we introduce the concept of function of the product which can be defined as the desired operation of the system (*what* the product does). Consequently, behavior and performances required are then evaluated (see Section 3.4).
Table 5 reports a general description and the product proposal of the system.

Table 5 General description of the system and product proposal.

Short description	A porous lattice structure for human cancellous bone vertebral implants
Function (purpose)	A system which ensure a minimally invasive vertebral stabilization after en bloc resection
Constraints	3D-printed (*via* SLM)
	Made of titanium alloy (Ti6Al4V)
Hypothesis	Applies to cases of lumbar vertebral body replacement (VBR)
	Exhibit peculiar biomechanical properties
	Promotes bone ingrowth (high porosity)
	Similar elastic modulus to that of the human trabecular bone
	Compatible with different cage systems or vertebral prosthetics
	Flexible and/or adaptable
	Easy to manufacture

3.3.2 System definition

The design process of this particular product concerns the redesign of an existing devices.
To change the lattice structure to an existing implant (e.g. for a 3D-printed prosthesis) may require something more extensive.
The modification of an existing product to meet new objective functions can lead additional difficulties, that varies based on the different types of prosthetics considered.
For example, a general titanium 3D-printed vertebral implant (see Section 2.4.3) consists of three main parts, Figure 22.

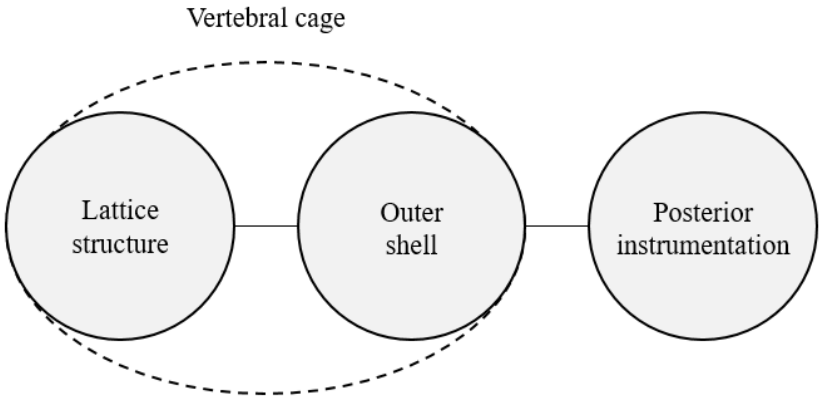

Figure 22 Basic system decomposition of a 3D-printed vertebral implant.

As shown in Figure 22, the design and modelling of the VBR lattice structure is strongly correlated to the others parts that compose the overall vertebral implant (i.e. the cage).
As a result, the generation of new concept must considerer the whole structure and the interactions between its different parts (see Section 3.5).

3.4 Understanding the problem

3.4.1 Customers' requirements

At this stage, we need to generate the requirements [78], which are then used to evaluate the performance and to generate engineering specifications.
In particular, requirements refer to specific customer(s), which in this case are represented by the surgeon and by the patients.
Finding requirements for our device (i.e. the vertebral cage) involve the following aspects:

- The surgeon needs;
- Observing customer (the surgeon) during using actual devices (e.g. during the implantation of a 3D-printed implant);
- Patients follow-ups from *Rizzoli*'s data collection;
- Clinical aspects related to VBR resection and stabilization found in literature.

The requirements are organized in a hierarchical structure (number in the list) and evaluated in order of importance by generating a weighting factors, Table 6.
Specifically, the relative order of the weighting factors ranging from 1 to 5, where 1 = "low importance" and 5 = "high importance".
The weighting will give an idea of how much effort and time to invest in achieving each requirement.
Hence, the customers' requirements must be translated into measurable design specifications to identified critical parameters (see Section 3.4.2).

Table 6 Requirements of the system.

N°	Requirement	Importance
1	Bear different loading conditions	5
2	Durable	5
3	Easy to position	5
4	Ensures correct stabilization	5
5	Minimally invasive	5
6	Patient specific	5
7	Easy to implant	5
8	Promotes bone ingrowth	4
9	Prevents concentrated contacts with vertebral endplates	4
10	Has a minimum size	3
11	Complies with the standards	2
12	Maintenance-free	1
13	Avoids damage adjacent tissues	1
14	Lightweight	1
15	Cheap	1

3.4.2 Target specifications

Here, we must develop a set of target (or engineering) specifications that quantifies the customers' requirements have been met [78, 79].

These specifications are the restatement of the design problem in terms of parameters that can be measured. Engineering specifications consist of two items: first, the parameters of interest; second, the target value for parameters, Table 7.

Final target values are then defined later (see Section 3.6.4).

Table 7 Target specifications of the system.

Requirement	Parameters	Unit	Target value
Bear to different loading conditions	Maximum spinal loads	list	See [41]
	Fatigue strength	years	≥ 10
Durable	No corrosion phenomena	binary	Yes
	Biocompatible	binary	Yes
Easy to position	Elongation	%	3 ÷ 5
	Compression	%	3 ÷ 5
Ensures correct stabilization	Deviation from the restored sagittal axis	mm	≤ 1
	Subsidence of the terminal endplates	mm	≤ 1
Minimally invasive	Elastic modulus	list	See [19, 23]
Patient specific	Height of the prosthesis	mm	45 ÷ 60
	Width of the prosthesis	mm	≤ 54
	Depth of the prosthesis	mm	≤ 44
	Connection supports for internal spinal fixator	list	See [14]
Easy to implant	Handy	binary	Yes
	Deployment time	minutes	≤ 80
Promotes bone ingrowth	Porosity	%	70 ÷ 90
Prevents concentrated contacts with vertebral endplates	Area of maximum contact	list	See [80, 81]
Has a minimum size	Cage area	list	See [80, 81]
Complies with the standards	Standards	list	See [82]
Maintenance-free	No	binary	No
Avoids damage adjacent tissues	Reoperation	binary	No
	Not interfering with the spinal cord	binary	No
	Shell thickness	mm	≤ 1
Lightweight	Mass	kg	minimum
Cheap	Cost	€	minimum

3.5 Concepts generation

3.5.1 Defining functions and sub-functions

In order to develop the specifications and requirements of the product, we must define the functions of the system [78].

Specifically, the main function of the device can be outlined as in Figure 23; where the fine, bold and dotted lines represent the energy, the materials and the information flows, respectively.

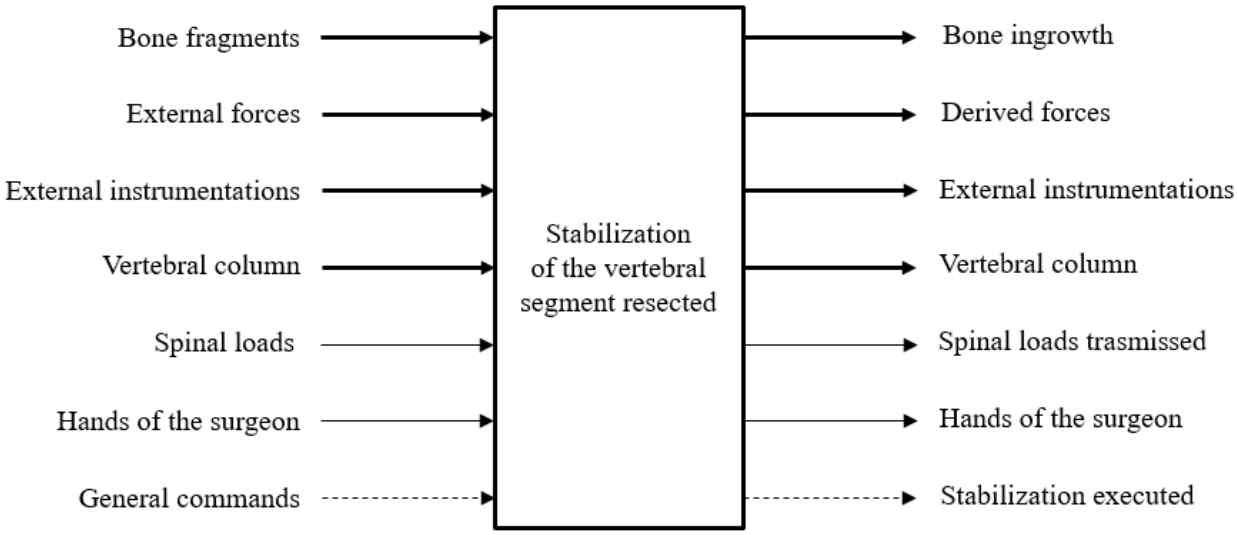

Figure 23 Main function of the system.

Thus, we must decompose the main function of the system in order to identify the sub-functions needed, Figure 24.

However, in keeping to the planning scheme and to the objective function of the work, we need to clarify two main aspects related to the decomposition technique shown in Figure 23 and Figure 24:

- Due to the complexity of the problem, the main function of the system is related to the entire vertebral implant which can lead various alternatives for generating new concepts in the design of a new lattice structure;
- Height adjustment can be referred both to the surgeon manipulation and to the use of a distractible system.

Thus, these issues will address and clarified in the following sections.

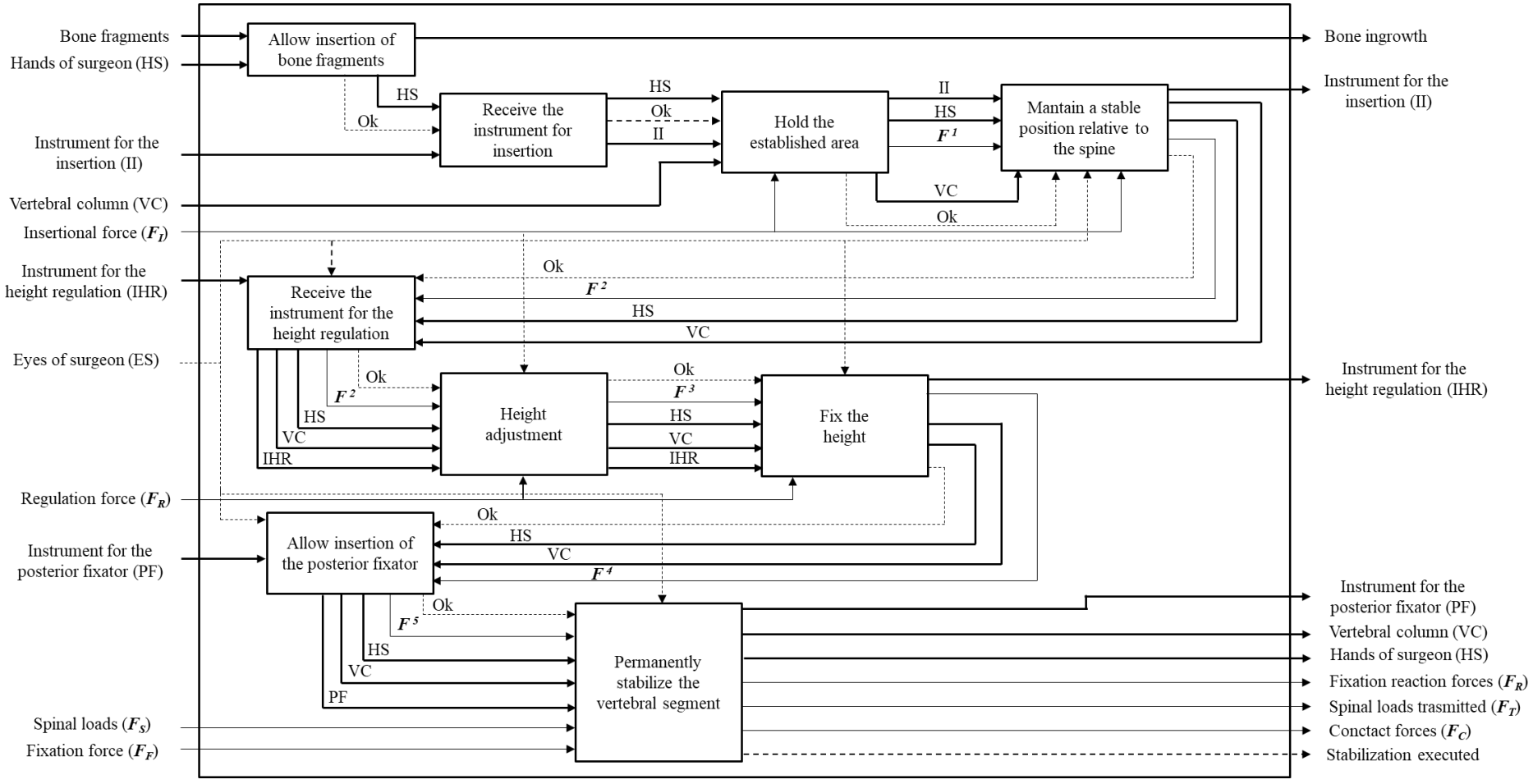

Figure 24 Functional decomposition of the system.

3.5.2 Critical sub-functions

Identify the critical sub-functions of the system is a crucial step in order to develop new design solution [78].
With reference to Figure 24, critical sub-functions are shown in Figure 25.

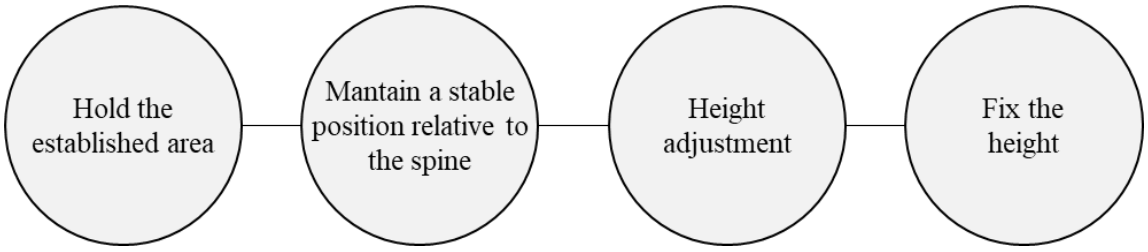

Figure 25 Critical sub-functions of the system.

As shown in Figure 25, the height adjustment is a critical step, especially during the intra-operative phase.
Maintaining a stable position it is crucial in order to prevent the subsidence and collapse of the vertebral implant into the adjacent vertebral bodies, which is performed by the surgeon. Consequently, the increasing insertional force can give rise of high stress concentrations between the vertebral end-plates and the prosthetic end-plates.
In general, all these actions relative to the VBR surgery approach, lead to increased misalignment of the spine.

3.5.3 Generating concepts

3.5.3.1 Concepts generation: what and how?

As we known, the design of a new lattice structure must consider certain specific objective and constrains, as defined in Section "*Problem definition*", which are summarized in Figure 26.
Form, material and production techniques have been considered in conceptual design while develop concept for the function and sub-functions (see Figure 26). Then, constrains and components of the system play a fundamental role in the design process: feasible solutions are strongly correlated to the customers' requirements and to the manufacturing techniques. Design a new the lattice geometry on its own may lead poor design solutions.

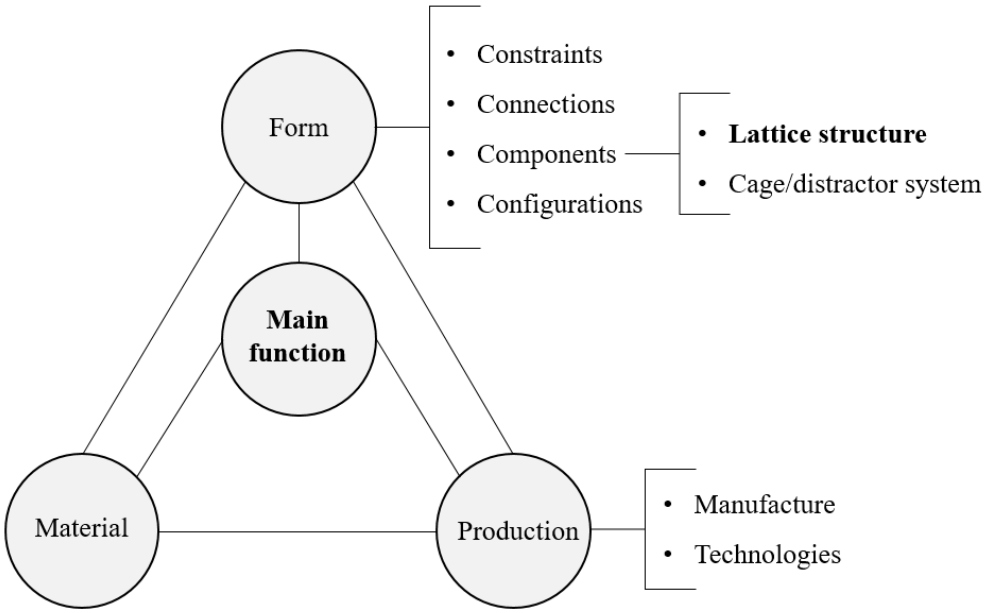

Figure 26 Basic elements of vertebral implant design.

Hence, in order to find original solutions for developing new lattice structure, we must consider the following aspects:

- The form of the lattice structure is roughly defined by the spatial constraints and by product constraints defined earlier;
- Optimal solution (the "trade-off") for our macro-engineering problem is defined as a configuration of connected components (e.g. the lattice structure and the outer shell).

Then, concept generations focus on the two items: first, generation of new lattice structure solutions; second, generation of ideas for the corresponding connection components.

3.5.3.2 The morphology matrix

Table 8 shows the corresponded morphology matrix developed [78, 79]. As shown in Table 8, there are few functions that can be fulfilled in only one way (e.g. hold the established area - height adjustment). Furthermore, the concepts generated for each sub-functions are strictly related to the constraints of our engineering objective (the lattice structure).

Table 8 Morphology matrix.

		Concepts				
		1	**2**	**3**	**4**	**5**
Sub-functions	**Hold the established area**	Conventional scaffold	Modular components	Expandable device	Auxetic scaffold/shell	Mesh cage
	Maintain a stable position relative to the spine	High size end-plates	Anatomical end-plates	Adjustable end-plates	Deformable end-plates	High porous end-plates
	Height adjustment	Surgeon manipulations	Distractible system	Linkage mechanism	Auxetic scaffold	Auxetic foam
	Fix the height	Surgeon manipulations	Conventional scaffold	Ratchet mechanism	Expandable system locking	Spacers
	Permanently stabilize the vertebral segment	Posterior fixator connection	Clamp system	Body screws	Lateral plates	
	Allow insertion of bone fragments	High porous scaffold	Opening on the cage			
	Receive the instrumentation for insertion	Pliers system	Magnetic elements	Locations for the fixator	Surgeon manipulations	
	Receive the instrument for height regulation	Pliers system	Magnetic elements	Surgeon manipulations		
	Allow insertion of the posterior fixator	Screws and rods	Locations for the fixator			

3.5.4 Combining concepts

The final design solution can be obtained by combining the individual concepts [78, 79] from the morphology matrix (see Table 8).
However, the method raises two problems:

- Frequently, different functions can be simultaneously satisfied by the same concept (relationship between the same sub-functions);
- Results may not make any sense.

In addition, in order to decrease the number of ideas, combining concepts must regard that:

- The combinations must be made by focusing on the critical sub-function(s) (see Section 3.5.2);
- The combinations should consider the relations between the critical sub-functions.

In particular, the combined concepts are referred especially to the lattice structure, with regard to all the possible promising solutions related to the entire vertebral implant (rational design). Then, the combinations are followed by sketches.
The results of the combinations are reported in Table 9.
The goal is only to develop concepts and that effort must not be wasted worrying about details.
Thus, choosing best concept is the subject of the next section (the "*Concept evaluation and selection*" section).

Table 9 Matrix of the combined solutions.

	Critical sub-functions				
N° of solution	Hold the established area	Maintain a stable position	Height adjustment	Fix the height	**Sketch**
1	Conv. scaffold	High porous end-plates	Auxetic scaffold	Surgeon manipul.	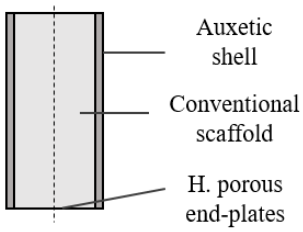
2	Auxetic shell	High porous end-plates	Surgeon manipul.	Conv. scaffold	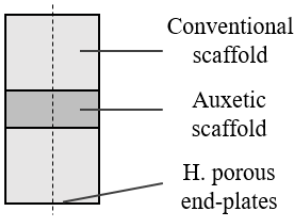
3	Modular components	High porous end-plates	Surgeon manipul.	Surgeon manipul.	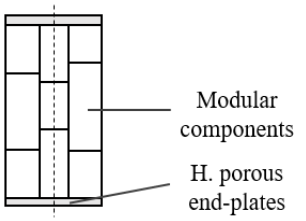
4	Modular components	Adjustable end-plates	Surgeon manipul.	Surgeon manipul.	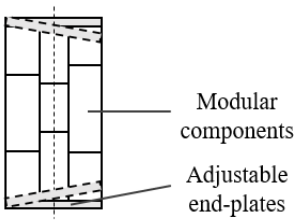
5	Conv. scaffold	Adjustable end-plates	Distractible system	Expandable system locking	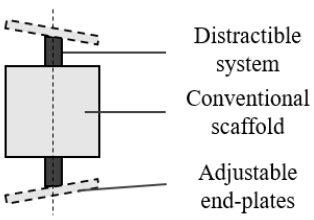

3.6 Concepts evaluation and selection

Once the concepts generating process is complete, we explore techniques for choosing which concept has the highest potential for becoming a quality product.
The robust decision making consider:

- Evaluation of the information on alternatives: greater the knowledge, the less the uncertainty;
- Evaluation on feasibility;
- Comparing the alternatives with the state-of-the-art for analogous products.

Then, decision making matrices are employed, which are:

- The screening matrix;
- The scoring matrix.

The matrices are based on the Pugh's method [78, 79].

3.6.1 Screening matrix

Screening matrix evaluates the product alternatives (see Table 9) based on the customers' requirements (see Table 6).
In particular, we generate a simple qualitative list of the generating concepts by assigning a relative score in relation to a reference product, defined as:

- "-1" = worst;
- "0" = equal;
- "+1" = better.

Specifically, the reference model of vertebral implant choose is the 3D-printed custom made cage implanted at the *Rizzoli* Institute (see Section 2.4.3).
Screening matrix rapidly identifies the strongest design solutions (and the alternatives to be rejected) and helps foster new alternatives, see Table 10.

Table 10 The screening matrix.

.

Requirements	Import.	Reference	1	2	3	4	5
			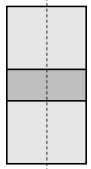	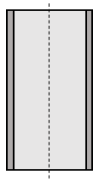	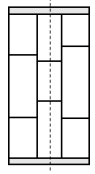	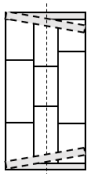	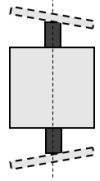
Bear to different loading conditions	5	0	0	0	-1	-1	-1
Durable	5	0	0	0	0	0	0
Easy to position	5	0	+1	0	+1	0	-1
Ensures correct stabilization	5	0	0	0	0	0	0
Ensures correct sagittal alignment of the spine	5	0	0	0	0	+1	+1
Patient specific	5	0	0	0	+1	+1	+1
Easy to implant	5	0	+1	+1	+1	-1	-1
Promotes bone ingrowth	4	0	0	+1	-1	-1	-1
Prevents concentrated contacts with vertebral endplates	4	0	0	0	0	0	0
Has a minimum size	3	0	0	0	0	0	0
Comply with the standards	2	0	0	0	0	0	0
Maintenance-free	1	0	0	0	0	0	0
Avoids damage adjacent tissues	1	0	+1	-1	0	0	0
Lightweight	1	0	0	+1	-1	-1	-1
Cheap	1	0	-1	0	0	0	-1
Sum of “+1”		0	3	3	3	2	2
Sum of “0”		15	11	11	10	9	7
Sum of “-1”		0	1	1	2	4	6
Total		**0**	**+2**	**+2**	**+1**	**-2**	**-4**
Ranking		**4**	**1**	**1**	**3**	**5**	**6**
Conclusion		**Reject**	**Combine**	**Combine**	**Reconsider**	**Reject**	**Reject**

As shown in Table 10, three are the solutions that needs to be combined or reconsider:

- Solutions n°*1* and n°*2*: which in part involve an auxetic structure (internal or external);
- Solution n°*3*: the modular device.

Then, in order to improve each design solution, scoring matrix was employed in the following section.

3.6.2 Scoring matrix

Scoring matrix evaluates the combinations of the best design alternatives found from the screening matrix in the previous section [78].
Specifically, the matrix provides a means of scoring each alternative concept relative to the others in its ability to meet the criteria (the customers' requirements).
Score ranging from 1 to 5, where 1 = "bad" and 5 = "excellent".
Hence, for each score was associated a weighted factor, that is equal to the value of importance of each customers' requirements (see Table 6).
With reference to Table 10, three combined solutions are evaluated:

- A^{123}: combination of solutions n° *1+2+3*;
- $A1^{2}$: combination of solutions n° *1+2*;
- A^{13}: combination of solutions n° *1+3*.

Then, the corresponding scoring matrix is shown in Table 11.
Once the matrix was compiled, an optimal design solution can be selected. However, details on the final design product are shown in the following sections.

Table 11 The scoring matrix.

	A^{123}	A^{12}	A^{13}
	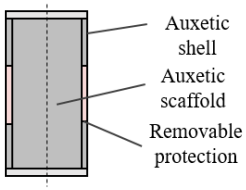	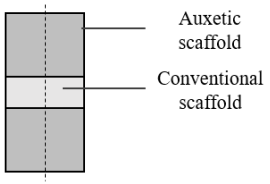	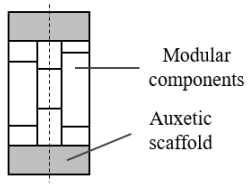

Requirements	**Importance**	Score	Weighted S.	Score	Weighted S.	Score	Weighted S.
Bear to different loading conditions	5	4	20	4	20	4	20
Durable	5	4	20	4	20	4	20
Easy to position	5	5	25	5	25	4	20
Ensures correct stabilization	5	4	20	4	20	4	20
Ensures correct sagittal alignment of the spine	5	4	20	4	20	4	20
Patient specific	5	4	20	4	20	5	25
Easy to implant	5	5	25	5	25	5	25
Promotes bone ingrowth	4	5	20	4	16	4	16
Prevents concentrated contacts with vertebral endplates	4	5	20	4	16	4	16
Has a minimum size	3	4	12	4	12	4	12
Comply with the standards	2	4	8	4	8	4	8
Maintenance-free	1	4	4	4	4	4	4
Avoids damage adjacent tissues	1	5	5	4	4	3	3
Lightweight	1	5	5	4	4	2	2
Cheap	1	3	3	4	4	2	2
Total			**227**		**218**		**213**
Ranking			**1**		**2**		**3**
Conclusion			**Proceed**		**Reject**		**Reject**

3.6.3 Final concept selection

Referring to Figure 27, the final concept found from the decision making phase (Section 3.6.2) has three main characteristics:

- Ideally, the main parts are fully auxetic (see Chapter 4);
- It is partially a modular system composed by a removable posterior part that prevents the contact between the lattice structure and the adjacent tissues;
- The vertebral cage presents high porous end-plates between the implant and the adjacent vertebral bodies interface.

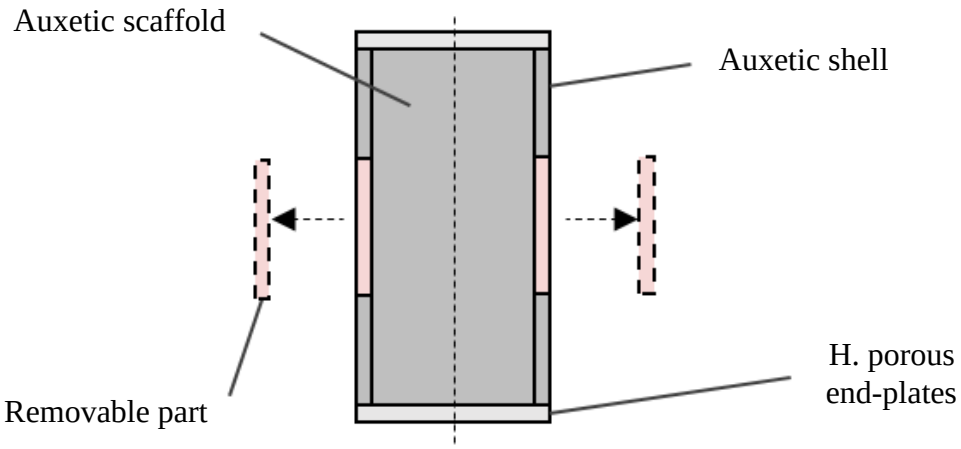

Figure 27 Schematic of the selected concept.

Since our scope is to develop new lattice structure, the design concept reveals two fundamental aspects. First, spatial constraints are crucial for the product development. Second, components can be separate, but configuration and architecture of the entire system needs to be considered.
However, only at this point the final target specifications of our system can be defined.

3.6.4 Final target specifications

At this stage, we fix the final target specifications of the system, Table 12.

Table 12 Final target specifications of the system.

Requirement	Parameters	Unit	Target value
Bear to different loading conditions	Maximum spinal loads	list	See [41]
	Fatigue strength	years	≥ 10
Durable	No corrosion phenomena	binary	Yes
	Biocompatible	binary	Yes
Easy to position	Elongation	%	3
	Compression	%	3
Ensures correct stabilization	Deviation from the restored sagittal axis	mm	≤ 1
	Subsidence of the terminal endplates	mm	≤ 1
Minimally invasive	Elastic modulus	list	See [19, 23]
Patient specific	Height of the prosthesis	mm	45 ÷ 60
	Width of the prosthesis	mm	≤ 54
	Depth of the prosthesis	mm	≤ 44
	Connection supports for internal spinal fixator	list	See [14]
Easy to implant	Handy	binary	Yes
	Deployment time	minutes	≤ 80
Promotes bone ingrowth	Porosity	%	≥ 70
Prevents concentrated contacts with vertebral endplates	Area of maximum contact	list	See [80, 81]
Has a minimum size	Cage area	list	See [80, 81]
Comply with the standards	Standards	list	See [82]
Maintenance-free	No	binary	No
Avoids damage adjacent tissues	Reoperation	binary	No
	Not interfering with the spinal cord	binary	No
	Shell thickness	mm	≤ 1
Lightweight	Mass	kg	minimum
Cheap	Cost	€	minimum

However, the target specifications reported in Table 12 are slightly different from the initial target values defined at the beginning of the design process.
In particular, two are the main parameters involved:

- The elongation/compression of the structure;
- Porosity.

The values of these parameters (i.e. the target values), have changed in order to accommodate the final concept identified (see Section 3.6.3).
After concepts have been generated and evaluated, it is time to refine the best concept found into actual product, which means:

- Defining the lattice structure geometry of the system (based on the final concept identified);
- Planning for modelling the form of the structure.

Moreover, before starting the modelling of the structure, one most take into account of which are the target value of our engineering problem, i.e. the lattice structure of the implant. These parameters are strongly correlated to those one of Table 12, but in some case (i.e. Young's modulus), quite different in magnitude. Given this, defining the form of the structure is the subject of the following chapters.

3.7 Concluding remarks

In this chapter, the conceptual design process for new vertebral lattice structure was presented and discussed.
The method employed and the results are summarized as follows:

- Design of new lattice structure for vertebral prosthetics regards the design and the analysis of the entire vertebral implant and the complex interactions between its parts;
- New design solutions are developed based on certain target specifications and on customers' requirements;
- Evaluation and selection of new concepts means to rationally compare the different product alternatives in relation to the customers' requirements and to the feasibility of the solution;
- Decision making matrices are employed for a robust design method;
- Final target specifications of the system are then fixed which are related to certain engineering parameters, such as modulus of elasticity, dimensions of the system and maximum loads.

4 OPTIMAL LATTICE STRUCTURE DEFINITION

The aim of the chapter is to identify the optimal lattice structure that performs the desired functions for the final design concept found previously (see Section 3.6.3). Specifically, this transformation phase represents the basic structure for the modelling and analysis of the lattice architecture of vertebral implant.

The chapter is divided into two sub-sections. First, the concept of auxetic mechanical metamaterials is presented. Second, optimal geometry for the VBR lattice structure was selected and discussed.

4.1 Overview on auxetic metamaterials

Negative Poisson's ratio (NPR) materials, also known as auxetics metamaterials [83–87], exhibit the counter-intuitive property of expanding laterally upon the application of a uniaxial tensile strain and other advanced functionalities including higher shear stiffness [88], indentation resistance [89, 90], energy dissipation [91, 92], fracture toughness [93] and synclastic behavior [94].

Auxetic structures have been widely used in a number of applications, particularly in the biomedical [95, 96], personal protection [97] and electronics sectors [98].

The unusual mechanical behavior of these materials originates primarily from their geometry, which makes auxeticity scale-independent.

Based on deformation mechanisms and their geometry, three main classes of auxetic structures can be identified: re-entrant structures, chiral structures and rotating (semi-) rigid structures, see Figure 28.

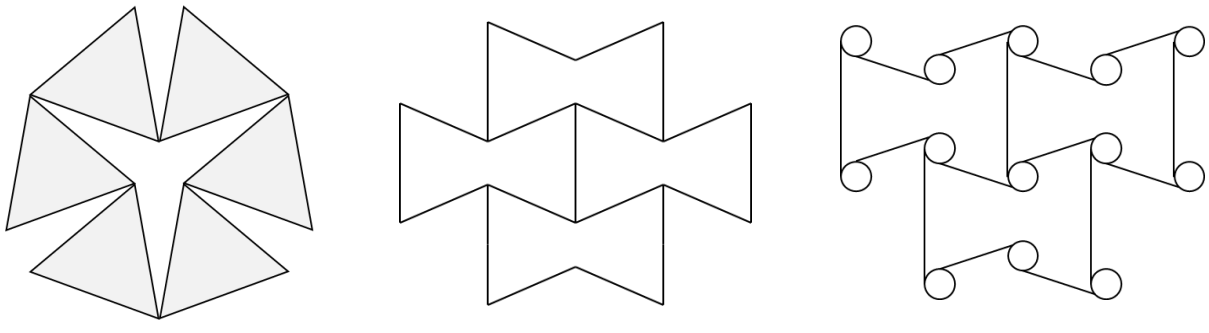

(a) (b) (c)

Figure 28 Planar auxetic metamaterials: a rotating structure (a), a re-entrant structure (b) and a chiral structure (c).

In particular, geometrical features of these structure affects their mechanical properties in terms of Poisson's ratio (PR) and Young's modulus (E).

Specifically, re-entrant structures outperform the chiral and rotating rigid structures in terms of PR and corresponding stiffness (E) [99]. Otherwise, the rotating rigid structures seem to offer a relatively high Young's modulus.

The emerging concept of mechanical metamaterials has attracted growing attention due to increased additive manufacturing (AM) technologies. In particular, advances AM enables the fabrication of complex metallic structures with specific mechanical properties.

However, the majority of works found in literature concerning the design of titanium alloy-based auxetic metamaterials for use in biomedical devices such as implants and scaffolds has focused mainly on the design, fabrication and characterization of ligament-based structures [99], while there have also been other studies on re-entrant [100], chiral [101] and triangle-square-wheels metallic auxetic systems [102].

On the other hand, there are very few studies centered on the design of metal-based rotating units systems.

As highlighted by Kolken *et al.* [99], simple design and fabrication solutions for the rotating structures manufactured *via* AM have yet to be fully investigated, especially 3D printing metallic structures made of titanium alloy.

4.2 The rotating auxetic structures: a prospective solution

Rotating auxetic structures seem to be a valid alternative for the development of new additively manufactured titanium lattice structure for vertebral bone defect reconstruction.

An idealized rotating auxetic system is composed by rigid squares units connected through simple hinges at the vertices [99], Figure 29. This concept has been largely implemented using squares, rectangles, triangles, rhombi, and parallelograms.

Rotating unit mechanisms include both 2D (planar) auxetic system and 3D auxetic lattice structure. The 3D auxetic structure represents the natural transposition of the planar structure in the 3-dimensional space.

Understanding the planar behavior of these systems it is crucial for developing unconventional lattice structure with variable shapes and specific mechanical properties. However, limits of its fabrications and of its geometrical features are still unknown.

Given this, the modelling of a new lattice structure focuses on two auxetic mechanisms: first, the 2D rotating squares structure (see Section 4.2.1); second, the 3D rotating architecture with cuboids (i.e. the corresponding 3D configuration in Section 4.2.2), which are the subject of the following paragraphs.

4.2.1 The 2D rotating squares auxetic metamaterials

The 2D (planar) rotating squares system, first proposed by Grima *et al.* [103], was extensively studied in recent years [104], Figure 29.

The NPR mechanism with rotating squares is completely described by the following two geometrical parameters: the length of the unit, l, and the angle, θ (see Figure 29).

This mechanism ensures that when the system is loaded, the squares rotate, either contracting or expanding the overall system depending on whether a compressive or tensile load is applied.

As a result of this mode of deformation, the system exhibits in-plane isotropy with a Poisson's ratio (PR) of -1.

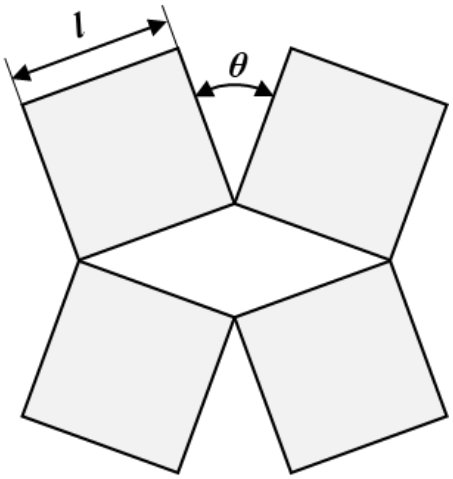

Figure 29 Representative unit cell (RUC) of rotating squares system.

Rotating squares systems have also been designed and manufactured using single-material systems, where the idealized 'joints' in the original model, were replaced by fused interconnections between the square units.

Thus, the mechanical properties of this structure are strongly affected by:

- The geometrical parameters of the unit cell (l and θ);
- The type of connection between the squares.

However, the interconnection regions of these systems are subjected to large stress concentrations during loading, which makes them unsuitable for large strain deformations in the case of systems made from materials with an inherently low strain tolerance.
Then, to improve the global strain tolerance of these systems some form of geometric optimization is required in these regions [105]. This is particularly pertinent in the case of metal-based auxetic systems, where the material reaches the plastic region at very low strains.

4.2.2 The 3D rotating cubes auxetic geometry as vertebral scaffold

General 3D configuration of auxetic structure with cuboids are based on the works of Attard [106] and Lakes [107], see Figure 30.
As shown in Figure 30, the representative unit cell (RUC) of the system consists of eight cuboids of side length l. Specifically, each cube of the unit cell is connected to the others as follows: the cube sharing two of its faces to the others on its lower and upper sides (e.g. point A in Figure 31.a), while the remaining four corners, are connected to each counterpart through simple hinges at vertices (e.g. point B in Figure 31.b).

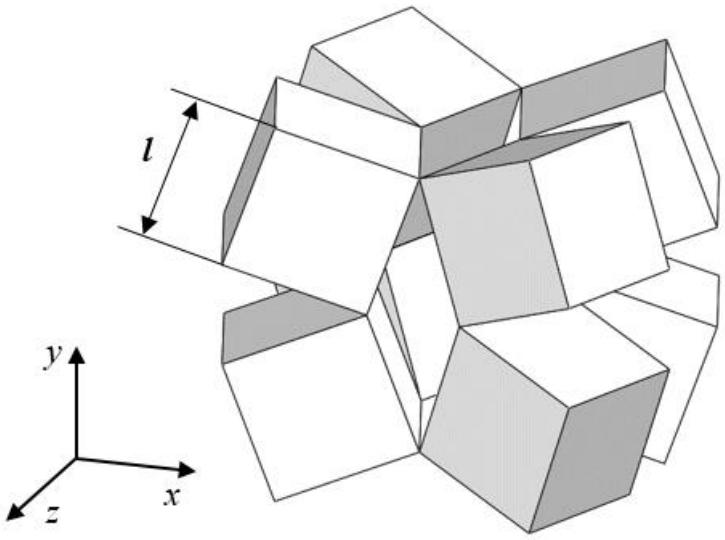

Figure 30 RUC of the 3D auxetic geometry with cubes.

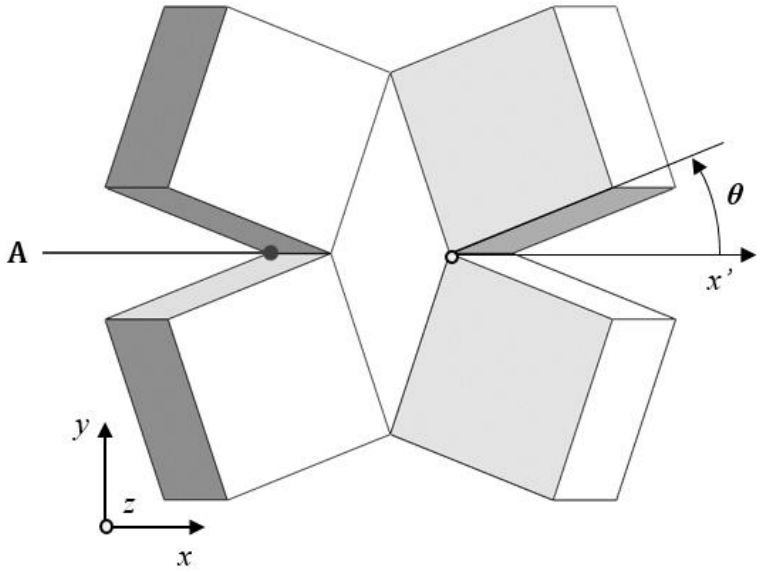

(a)

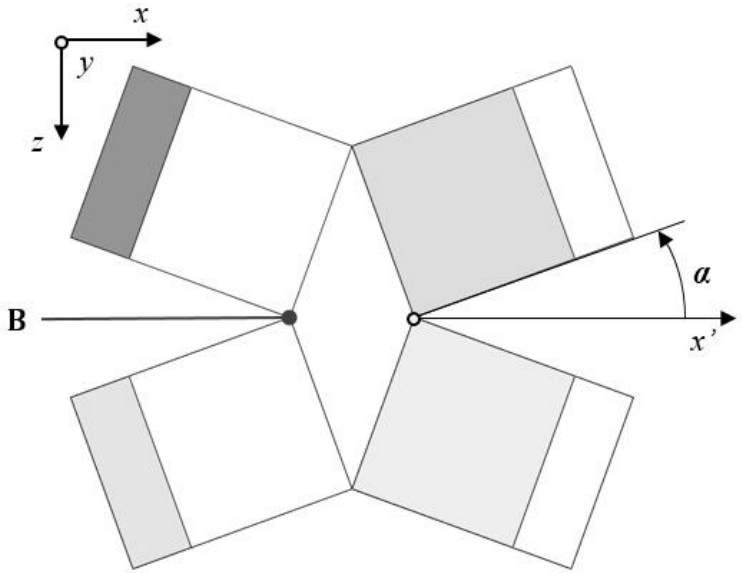

(b)

Figure 31 Front view (a) and upper view (b) of the unit cell.

The orientation of the cubes that composed each unit cell is described by two angles: first, the angle θ (resulting from a rotation around the *z*-axis in Figure 31.a); second, the angle α (resulting from a rotation around the *y*-axis in Figure 31.b).

The structure can be obtained by a composition of rotating cuboids, and in fact can be used as the basic unit cell to build the lattice structure of the vertebral implant, Figure 32.

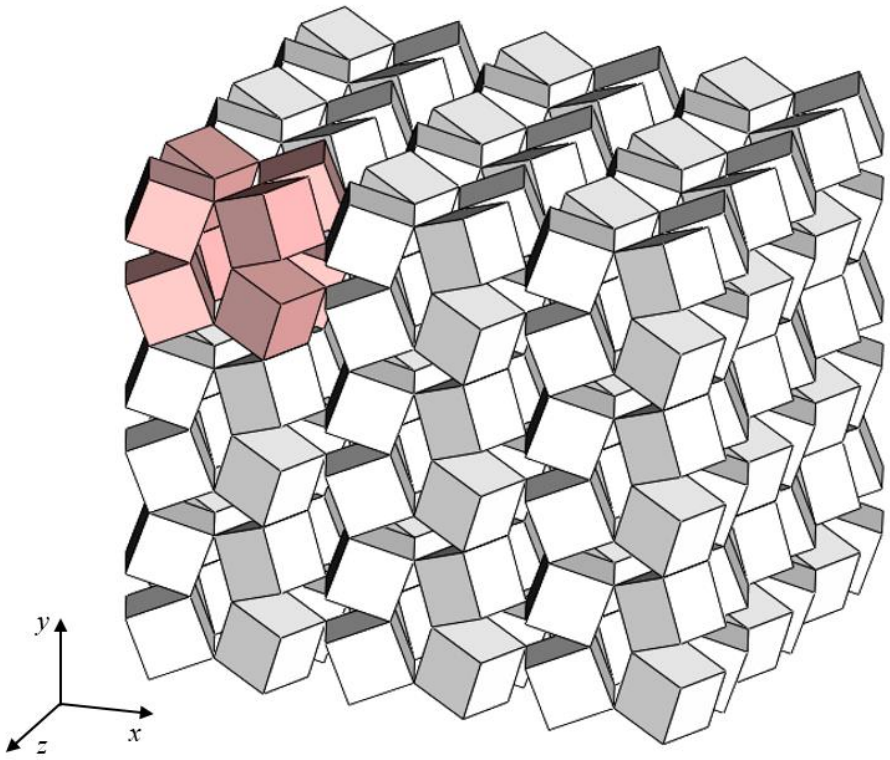

Figure 32 3D construct with cuboids.

As for the case of rotating squares auxetic systems, the mechanical properties of this structure, such as the PR and the E, are influenced by the geometrical parameters of the unit cell (l, α and θ) and by the types of connections between each cubes.

With this in mind, it is useful to underline that the 3D auxetic structure shares many geometrical features with its planar counterpart.

To be more specific, the idealized "joint-regions" in the upper and lower sides of the 3D construct (e.g. point A in Figure 31.a) are the same as in the planar rotating squares configuration.

4.3 Target specifications for the auxetic lattice structure

Once defined the basic lattice structure, it is necessary to fix the target specifications able to satisfy the targets defined for the designed implant (see Table 12). The target values for the auxetic scaffold are the basis of the modelling and analysis process of the next chapters.
However, these values are defined in relation to the customers' requirements.
Specifically, the main parameters and the corresponding target values are reported in Table 13.

Table 13 Target specifications of the lattice structure.

Requirement	Parameters	Unit	Target value
Bear to different loading conditions	Maximum compressive load	N	1888
	Maximum flexional load	Nm	16
Easy to position	Elongation	%	3
	Compression	%	3
Minimally invasive	Elastic modulus	MPa	≥ 75
Patient specific	Height of the structure	mm	45 ÷ 60
	Width of the structure	mm	≤ 54
	Depth of the structure	mm	≤ 44
Promotes bone ingrowth	Porosity	%	≥ 70
Has a minimum size	Cage area	mm^2	2376
Lightweight	Mass	kg	minimum

As highlighted in Table 13, three are the critical factors concern the development of the lattice structure, which are:

- The value of the elastic modulus (i.e. the Young's modulus);
- The strain tolerance of the structure (i.e. the elongation/compression function);
- The dimensions of the lattice structure (i.e. the geometrical features of the system).

Then, modelling and analysis of the lattice configuration is the subject of the following chapters.

4.4 Concluding remarks

In this chapter the basic lattice structure for the vertebral implant was identified and presented. Then, common characteristics and issues are summarized as follows:

- We proposed an innovative lattice structure configuration for the peculiar conceptual solution of the prosthesis;
- Rotating auxetic metamaterials represent a promising solution respect to other auxetic architecture;
- Rotating mechanisms include both planar auxetic system and 3D auxetic lattice structure;
- The 3D auxetic lattice geometry is obtained by the composition of rotating cuboids;
- Target specifications for the auxetic lattice structure have been defined.

5 MODELLING, ANALYSIS AND OPTIMIZATION OF 2D ROTATING SQUARES AUXETIC METAMATERIALS

5.1 Lattice structure optimization

In order to improve the mechanical properties of the vertebral lattice structure, the optimization process focuses on the following lattice geometries: first, a planar (2D) rotating squares auxetic mechanism; second, a 3D auxetic configuration of the planar system consist of cuboids (see Figure 33).

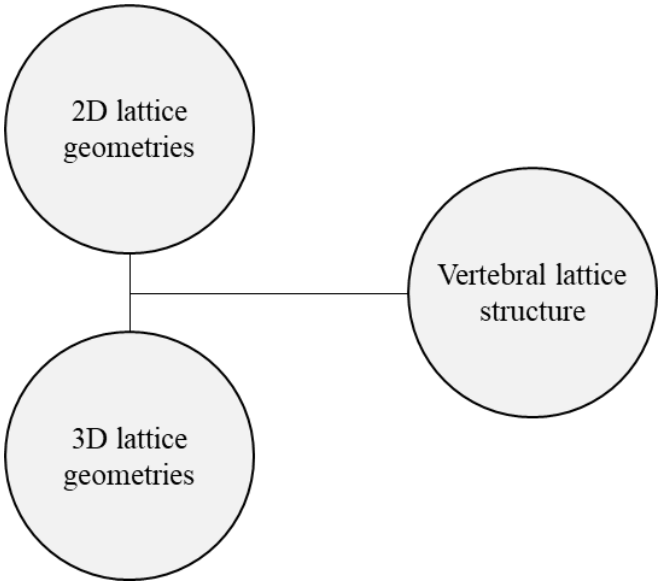

Figure 33 Schematic of the optimization process for vertebral lattice structure.

Specifically, we investigate and optimize a bio-inspired variable arcs fillets [108, 109] at the interconnection regions of the rotating units, where the stress concentrations also remarkably limit the fatigue life for these types of structures.

The optimization aims to identify some peculiar configuration of the auxetic lattice system that can be construct by combining different variable arcs fillet profiles (2D and 3D), and which have three main characteristics: first, a Young's modulus similar to that of cancellous bones; second, an improved strain tolerance; and third, with increased pore size and tissue regeneration properties.

Specifically, the chapter focuses on the modelling and the numerical analysis of a titanium alloy-based rotating squares auxetic metamaterials.

The aim is to optimize the structural response of metallic rotating auxetic metamaterials that accomplish the product concept and specifications defined in the conceptual design process.

5.2 Basic 2D lattice geometries

5.2.1 The variable arcs fillet geometries

In this section we investigate the planar rotating squares auxetic mechanism shown in Figure 29.
In order to avoid the structural limits of the region that connects the squares, the focus is on identifying the optimal shape of the interconnecting regions of the rotating units.
Two are the basic fillet curves investigated: first, a double circular arc fillet solution (Figure 34); second, a fillet that combines an elliptical arc and a circular arc (Figure 35).
The representative unit cell (RUC) of the rotating square model (Figure 34.a and Figure 35.a) is defined by the length of the square lattice, L, and the angle between the rigid units, θ, namely:

$$L = 2L_0 \tag{1}$$

$$\theta = 180° - \gamma \tag{2}$$

where L_0 is the side length of a quarter of the RUC (i.e. a rotating square), and γ is the supplementary (internal) angle of the structure.
For each solution proposed, Figure 34.b and Figure 35.b shown in detail the geometric configuration of a rotating square where, D, represents the side length of the rigid square, while $l_1 = D/2$ is the side length of the simulated structure.
Figure 34.c and Figure 35.c, show a close-up view of the two variable arcs fillet geometries proposed, where s represents the width of the ligament at the interconnection regions.
Specifically, the double arcs shape solution in Figure 34.c connects the ligament to the square with a double circular arcs fillet (radius R_1 and R_2).
Similarly, the solution in Figure 35.c, connects the ligament to the simulated structure through an elliptical arc combined with a circular arc fillet, where A and B in Figure 35.c are the two semi-axes of the elliptical arc, while R_2 is the radius of the circular arc.
Consequently, for both the solution, the dimensions l_2 and l_3, depend on the side length, l_1, of the simulated structure and from the fillet dimensions (see Figure 34.b and Figure 35.b).
To build the geometries, tangency conditions are imposed between the geometrical variables of the unit cell and the ligaments (i.e. points a, b, c and d in Figure 34.c and Figure 35.c).

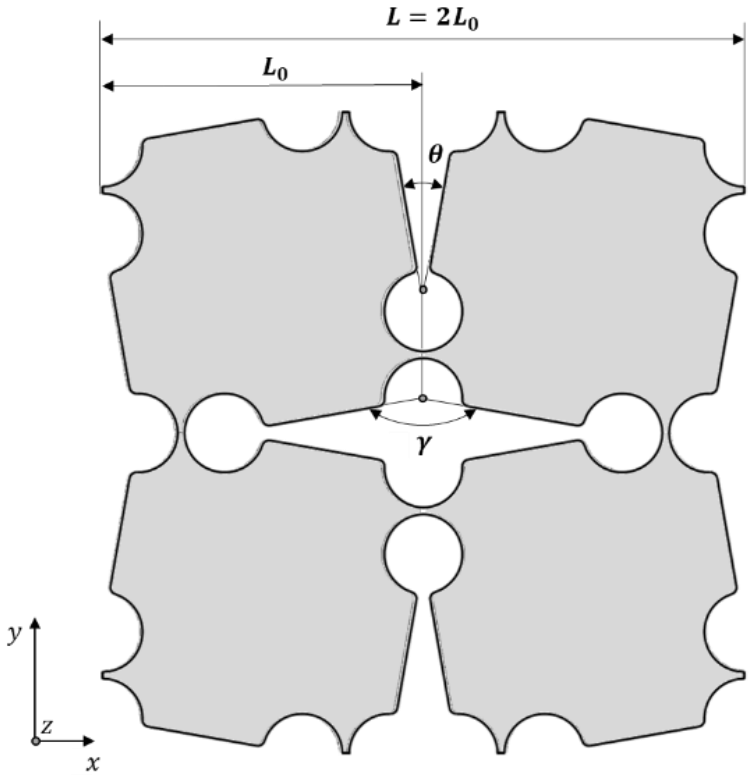

(a)

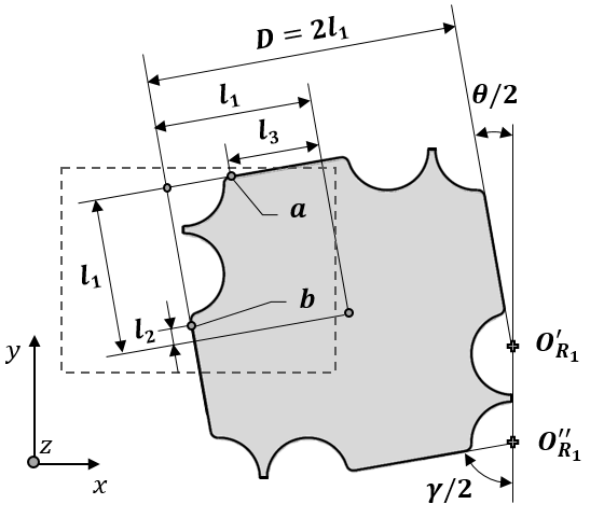

(b)

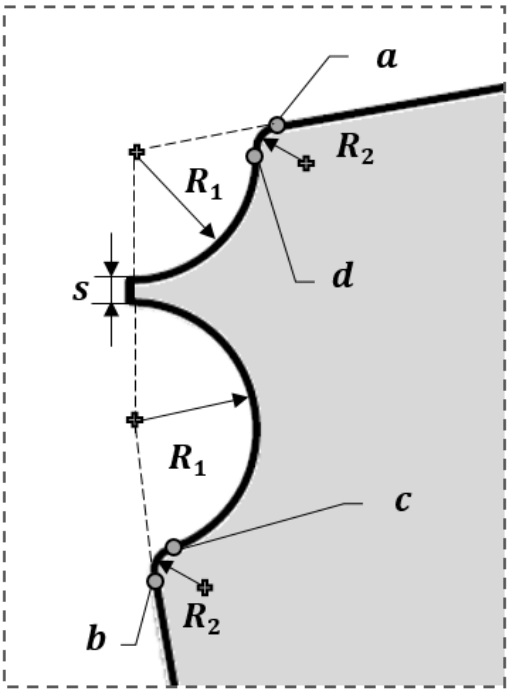

(c)

Figure 34 RUC of the rotating squares system with double circular arcs profile at the interconnection regions (a), unit cell (b) and detailed fillet geometry at the interconnection regions (c).

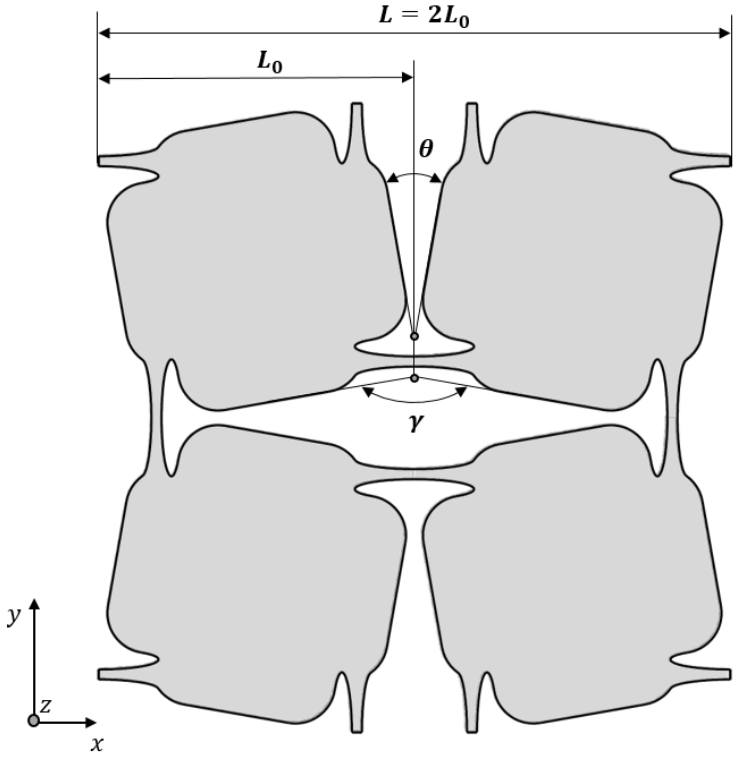

(a)

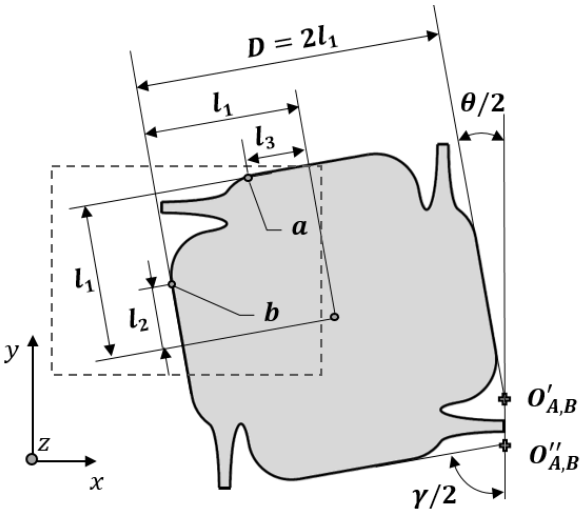

(b)

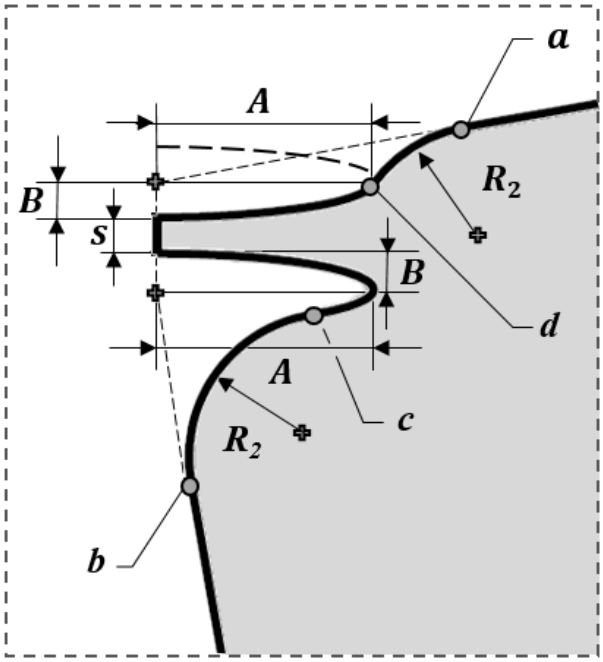

(c)

Figure 35 RUC of the rotating squares system with a combined elliptical and circular fillet profile at the interconnection regions (a), unit cell (b) and detailed fillet geometry at the interconnection regions (c).

5.2.2 The FE analysis

In order to investigate the structural response, we implemented a 2D finite element (FE) model of both the structures of the previous section, using the commercial FE software *Abaqus 6.20* [110]. Taking advantage of the highly symmetric nature of the rotating square system, the system was simulated as a quarter of the RUC, where s was set equal to 1 mm (see Figure 34 and Figure 35). The mesh consists of 2D plane-stress elements, with quadratic formulation (CPS8 [110]) and where the average element side length in the interconnecting regions was set equal to 0.05 mm, see Figure 36.

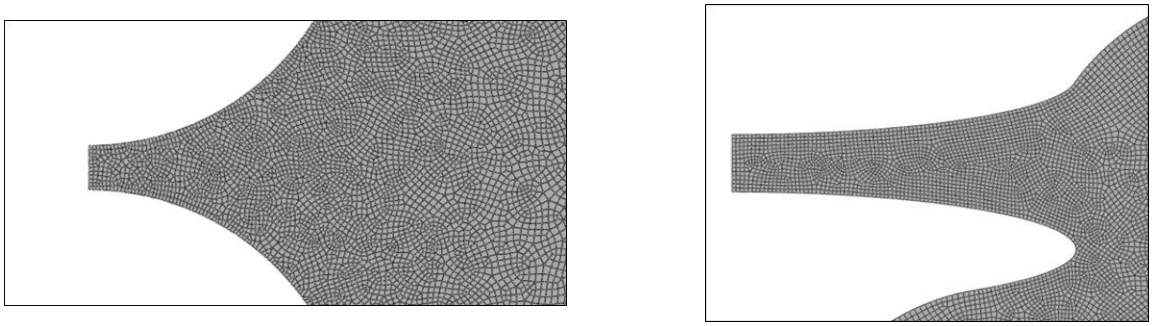

(a) (b)

Figure 36 Details on the FE model mesh with double circular arc fillet (a) and for the combined elliptical and circular fillet solution at the interconnection regions (b).

Since we focused on the maximum equivalent elastic stress in the auxetic system, the material used in the FE simulations was an isotropic elastic titanium alloy material (Ti6Al4V) produced by selective laser melting (SLM) [111]. Hence, the model applies a Young's modulus, E, equal to 110000 MPa, and a Poisson's ratio, ν, equal to 0.3; and considers a maximum allowable stress (i.e. yield stress), R_s, equal to 1013 MPa [111].

Figure 37 shows the boundary conditions and the applied load for the double circular arc solution [112, 113]. In particular, the rotating unit cell is simply supported in the nodes on the bottom edge (s_h^b in Figure 37) and on the left edge (s_v^l in Figure 37) of the cell. In addition, the nodes on the right edge (s_v^r in Figure 37) were coupled for equal displacement in the x-directions. The system was loaded through the application of a displacement, u_y, on the upper edge nodes (s_h^t in Figure 37). This displacement was proportional to the side length of the unit square, according to the following relationship:

$$u_y = L_0 \, \varepsilon_y \tag{3}$$

where $\varepsilon_y = 3\%$ is the global strain applied on the unit square in the y-direction, which corresponds to the target specification in Table 13.

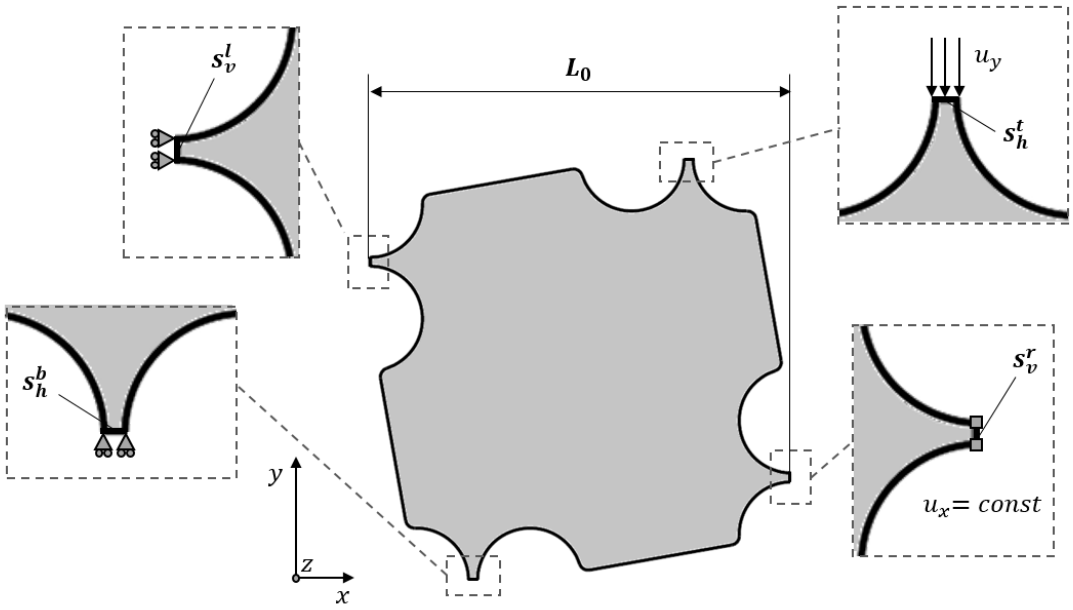

Figure 37 2D FE model of a quarter of the RUC with prescribed boundary conditions.

However, the same loading method was also applied for the combined elliptical and circular fillet systems.

To evaluate the mechanical response of the system, we performed a nonlinear static analysis, and calculated the apparent Poisson's ratio, v_{yx}^*, and the apparent Young's modulus, E_y^*, of the auxetic structure, assuming unit thickness, using [113]:

$$v_{yx}^* = -\frac{u_x}{u_y} \tag{4}$$

And

$$E_y^* = \frac{\sum RF_{y,i}}{L_0\ \varepsilon_y} \tag{5}$$

where u_x is the horizontal displacement of the nodes on the right vertical ligament (s_v^r in Figure 37) and $RF_{y,i}$ is the reaction force in the y-direction of the i-th node in the loaded edge ligament (s_h^t in Figure 37). In addition, the maximum von Mises stress in the system, σ_{vm}^{max}, was also measured.

5.2.2.1 The double circular arcs shape optimization

The first analysis focused on the design and optimization of a rotating squares auxetic system with a double circular arcs profile at the interconnection regions (see Figure 34).

The shape optimization problem involves four design variables: the angle θ, the two radii, R_1 and R_2, and the length, l_2, of the simulated cell (see Figure 34.b).

In order to increase the strain tolerance of the auxetic mechanism, the optimization aimed to: first, minimize the maximum von Mises stress, σ_{vm}^{max}, in the structure (usually occurring in the interconnection regions); second, maximize the apparent Young's modulus, E_y^*, of the system, while maintaining an apparent Poisson's ratio, v_{yx}^*, lower than -0.95.

Thus, the optimization problem can be defined as shown in Table 14.

Table 14 Specification of the optimization problem for the case of double circular arc fillet.

Geometry fillet	Design variables	Objective function	Constraints
Double circular arc	$20° < \theta < 160°$	$min\ \frac{\sigma_{vm}^{max}}{E_y^*}$	$s = 1$ mm
	1 mm $< l_2 < 10$ mm		$l_3 \geq s$
	1 mm $< R_1 < 10$ mm		$\varepsilon_y = 3\%$
	1 mm $< R_2 < 10$ mm		$v_{yx}^* < -0.95$

It is easy to observe that the length of the rotating square, $2l_1$, and the length of the RUC quarter of the system, L_0 (see Figure 34), are a function of the design variable l_2.

Specifically, we implemented an ad-hoc, automated shape optimization procedure that combines a genetic algorithm (i.e. the PSO algorithm [114]) managed though through the commercial optimization software *VisualDOC 8.0* [115], with a parametric, 2D FE model of the auxetic mechanism that runs the nonlinear stress analysis through the FE software *Abaqus* using *Python* language scripts [116].

In particular, at each iteration, the optimization solver sends the design variables to the *Abaqus* software, and computes the objective function and the constraints defined as in Table 14, where, E_y^* and v_{yx}^*, were calculated as shown in Eq. 4 and Eq. 5.

5.2.2.2 The combined arcs shape optimization

In a second step, we investigates the deformation behavior of a titanium rotating squares auxetic metamaterial with a double arc fillet at the interconnection regions by replacing the first circular arc (R_1 in Figure 34) with an elliptical shape solution (see Figure 35).

As for the case of double circular arc fillet solution, the analysis aims to: first, minimize the maximum von Mises stress in the structure, σ_{vm}^{max}; second, maximize the apparent Young's modulus, E_y^*, of the system, while keeping an apparent Poisson's ratio, v_{yx}^*, nearly -1.

However, by choosing small values of l_1 and θ, a further increase of the stiffness of the system can be obtained by reducing the dimensions of the minor semi-axis of the elliptical shape fillet, B, while keeping the relevant auxetic response of the rotating mechanism [117, 118].

Given the above assumptions, the variables of the optimization problem are two: first, the major semi-axis of the elliptical shape, A, and second, the radius of the circular arc, R_2 (Figure 35).

Due to the complexity of the geometry, the optimization was split in two steps (see Table 15).

Table 15 Specification of the optimization problem for the case of combined elliptical and circular arcs solution.

Geometry fillet	Step	Design variables	Objective function	Constraints
Combined elliptical and circular arcs	**1**	$6\ \text{mm} < A < 12\ \text{mm}$ $R_2 = 1\ \text{mm}$	$min\ \frac{\sigma_{vm}^{max}}{E_y^*}$	$B = 1\ \text{mm}$ $l_1 = 14\ \text{mm}$ $\theta = 20°$ $\varepsilon_y = 3\%$ $v_{yx}^* < -0.95$
	2	$A = 6\ \text{mm}$ $1\ \text{mm} < R_2 < 4\ \text{mm}$		

First, we fixed R_2 to a 1 mm value and found the *A* semi-axis that minimize the objective function in Table 15.

Second, from the optimal solution found in the first step, we examined the effect on the stress concentration at the interconnection regions of the radius of the circular arc, R_2.

Moreover, the nonlinear static analysis performed was the same described in Section 5.2.2.

5.2.3 Optimization results and discussion

5.2.3.1 Optimal lattice structures dimensions

Table 16 reports the optimal dimensions of the rotating units and of the ligaments at the interconnection regions for the two fillet geometries investigated through the FE analysis.

Table 16 Optimal dimensions of the unit cell and of the two fillet geometries investigated.

Geometry fillet	l_1 [mm]	L_0 [mm]	θ [deg]	R_1 [mm]	R_2 [mm]	A [mm]	B [mm]
Double circular arc	22.7	48.2	20	6	1	/	/
Combined elliptical and circular fillet	14	31.6	20	/	4	6	1

The optimal dimensions of the rotating unit with a combined elliptical and circular arcs shape fillet are significantly smaller than the ones of the double circular arc shape solution. This gives a RUC which is 34% smaller than the one with the double circular arc solution.
For both the solutions investigated, the optimization procedure suggests an angle, θ, between the rotating units, equal to 20°, in accordance with the theoretical models [117].

5.2.3.2 Mechanical properties

Table 17 compares the mechanical properties of the optimal metamaterial configurations identified through the FE analysis, where $R_s = 1013$ MPa is the yield stress of the titanium alloy [111].

Table 17 Mechanical properties of the optimal fillet geometries investigated.

Geometry fillet	v_{yx}^* [adm]	E_y^* [MPa]	σ_{vm}^{max} [MPa]
Double circular arc	−0.99	42.70	$> R_s$
Combined elliptical and circular fillet	−0.99	31.22	864

As shown in Table 17, the apparent Poisson's ratio, ν_{yx}^*, of the two optimized auxetic structures proposed is very close to -1, which corresponds to the maximum PR achieved from the theoretical predictions [103, 117].

Moreover, Table 17 highlights that the apparent Young's modulus, E_y^*, differs between the two geometries: 42.70 MPa for the double circular arc shape solution, and 31.22 MPa for the combined elliptical and circular arcs shape.

However, Table 17 shows that only in the combined elliptical and circular arcs solution the peak stress is lower (i.e. 864 MPa) than the elastic limit of the of the titanium alloy (i.e. 1013 MPa).

Specifically, the higher the major semi-axes of the elliptical arc, $A = 12$ mm, the lower are the values of the normalized apparent Young's modulus (with $E_y^* = 15.61$ MPa), and of the normalized peak von Mises stress, with σ_{vm}^{max} equal to 355 MPa (see Figure 38). On the other hand, by decreasing the value of A up to 6 mm, the value of E_y^* increases up to a value of 31.22 MPa, with a peak of the stress, $\sigma_{vm}^{max} = 864$ MPa (see Figure 38).

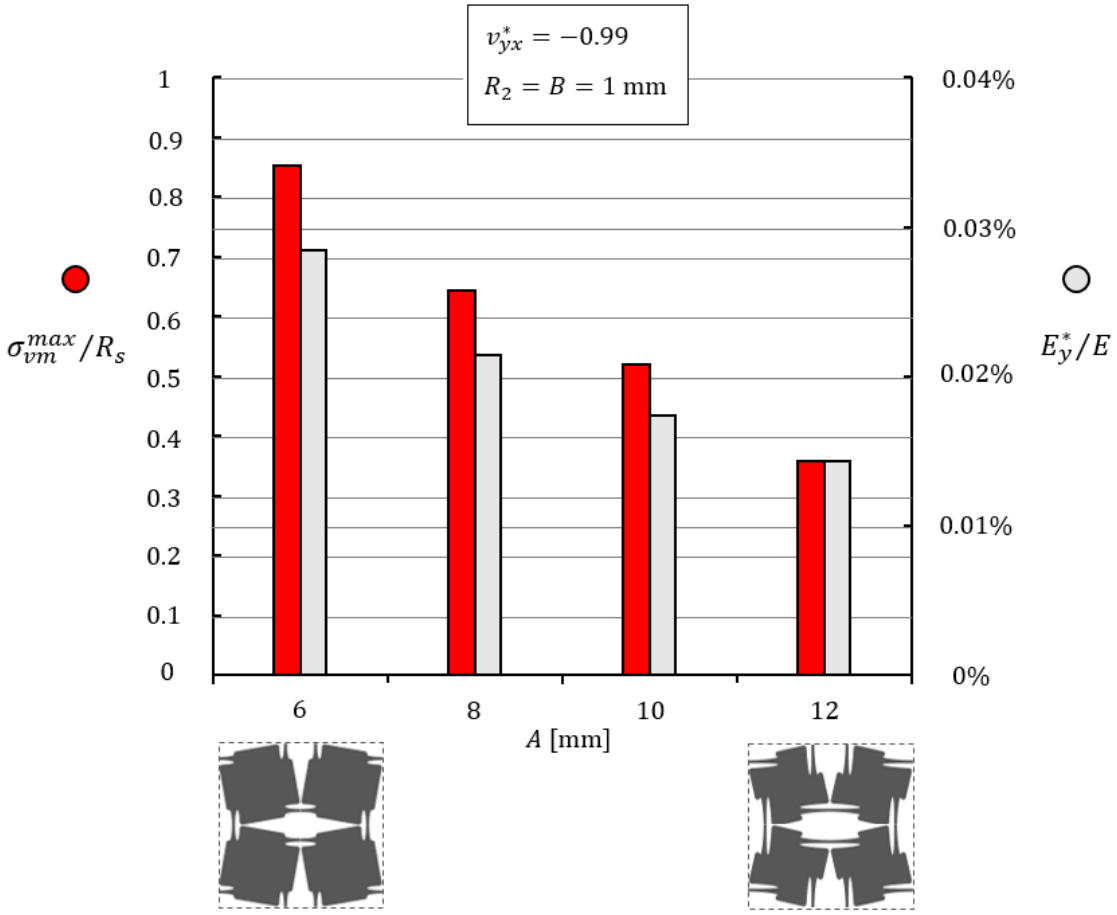

Figure 38 Normalized peak von Mises stress, σ_{vm}^{max}/R_s, and normalized apparent Young's modulus, E_y^*/E, for different levels of the major semi-axis of the elliptical arc, A, for the combined shape fillet.

Similarly, Figure 39 points out that, for a fixed configuration of the elliptical arc, the radius of the second arc, R_2, does not affect the auxetic response of the system, nor the peak stress: however, this circular fillet has a beneficial effect to avoids sharp corners on the geometry which are difficult to manufacturing, and to reduce the mass of the system.

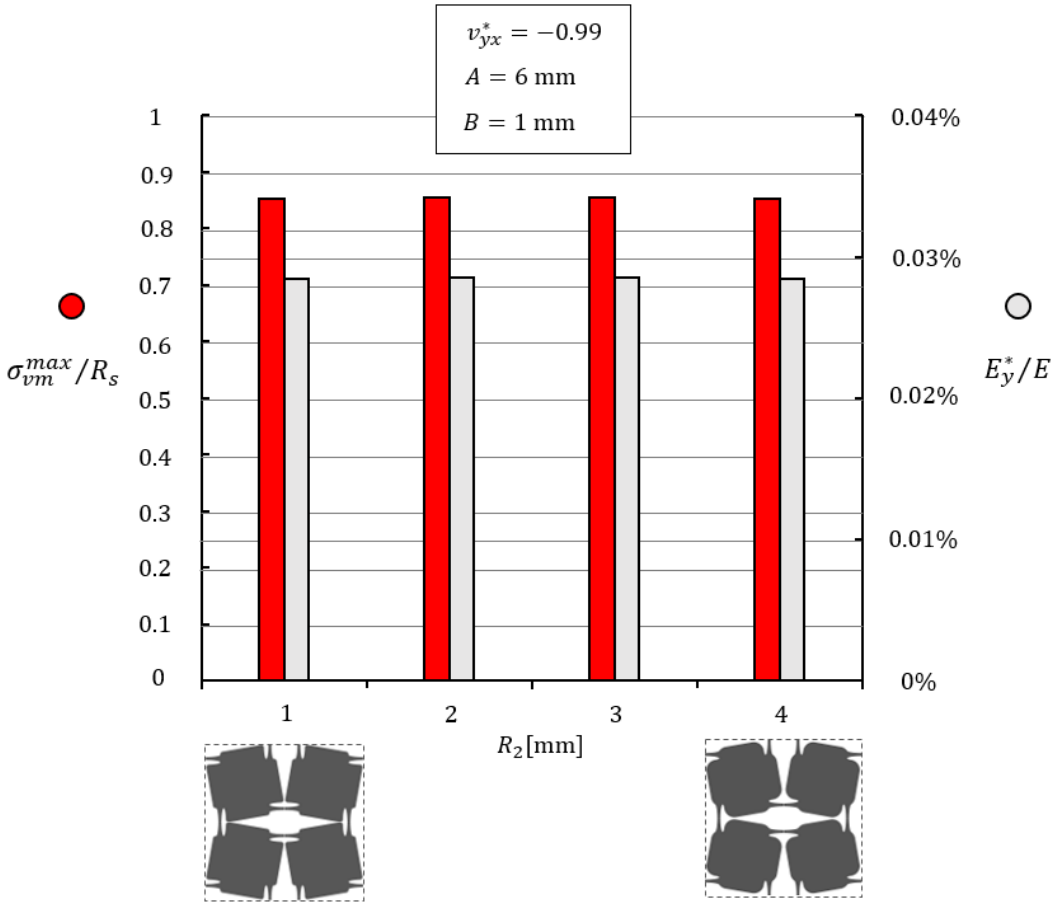

Figure 39 Normalized peak von Mises stress, σ_{vm}^{max}/R_s, and normalized apparent Young's modulus, E_y^*/E, for different levels of the circular arc, R_2, for the combined elliptical and circular shape fillet with fixed A.

In this regard, Figure 40 shows the von Mises stress contour acting on a unit cell for both the fillet geometries investigated.

As one may observe, the stress contours in Figure 40, highlight a stress concentration in the interconnection regions, which act as compliant joint and allow to obtain the peculiar kinematic response of the proposed auxetic structure.

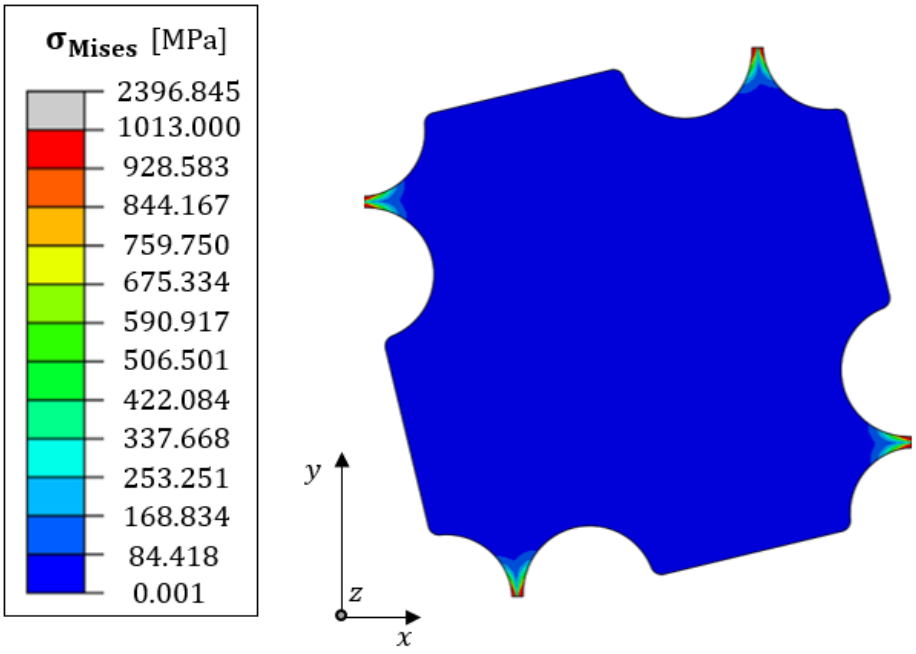

(a)

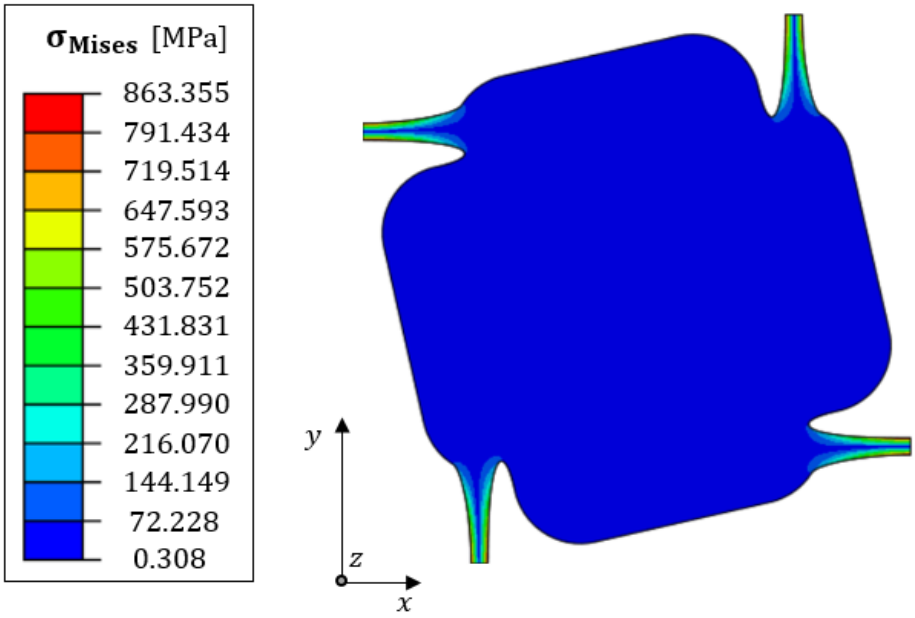

(b)

Figure 40 von Mises stress contour for the case of double circular arcs profile (a) and for the combined elliptical and circular shape solutions at the at the interconnection regions (b).

5.2.4 Experimental validation

5.2.4.1 Prototype development

The experimental validation focused on the combined elliptical and circular arc shape solution (Figure 35), since, according to the analysis in Section 5.2.3, it provides the best structural response.
Using the optimal dimensions of the RUC reported in the second row in Table 16, we built a prototype composed by a 3*x*3 RUC system (190 mm x190 mm), where the structure thickness in the out-of-plane direction was equal to 10 mm.
Since the deformation behavior of the structure is independent from its material, we manufactured the prototype using a fused filament fabrication (FFF) Markforged® 3D printing machine in Onyx material [119] (Figure 41.a).

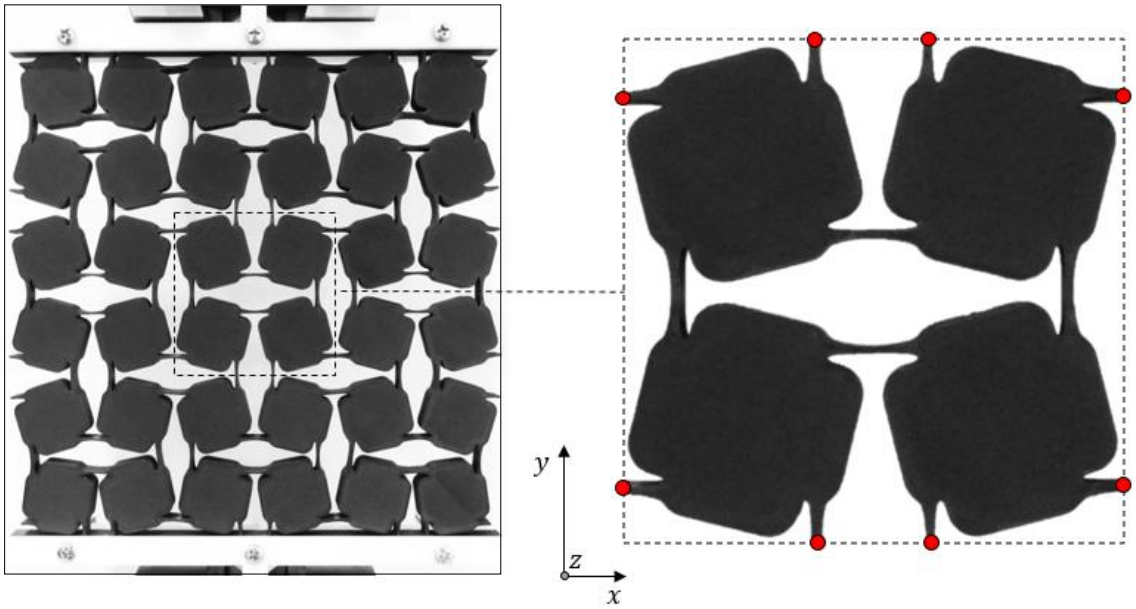

(a) (b)

Figure 41 Experimental prototype tested (a) and central RUC with the points used for tracking the displacements (b).

5.2.4.2 Test procedure

The prototype was uniaxially stretched using a *Galdabini SUN 500* electromechanical testing machine with a 5 kN loadcell, controlled by a PC equipped with the proprietary software *Graphwork*. The quasi-static tensile test applied a 5.7 mm stroke to the sample at a rate of 1 mm/min, which corresponds to an overall global strain of the sample equal to 3%.

In order to evaluate the Poisson's ratio of the structure, we measured the displacement field of the central RUC of the sample (Figure 41.b) using a *Dantec Dynamics Digital Image Correlation* system and analyzed the response through the *ISTRA 4D software*.

5.2.4.3 Experimental results and discussion

By tracking the displacement components of the eight marker points on the RUC (red dots in Figure 41.b), the DIC calculated the Poisson's ratio of the sample [120], see Table 18.

Table 18 Comparison between the numerical and experimental PR of the optimal auxetic system found with a combined arc fillet shape solution.

	Numerical	**Experimental**
$\boldsymbol{\nu_{yx}^{*}}$ [adm]	-0.99	-1.01

As reported in Table 18, the experimental PR obtained through the DIC analysis was equal to *ca.* -1 for strains up to 3% of the structure, in accordance with the FE results and with the theoretical predictions found from the literature [103, 118] for ideal rotating squares metamaterials.
However, as shown by numerical results (see Section 5.2.3), the only way to decrease the structure dimensions, and therefore to increase the stiffness of the whole structure, is to remove material from the semi-rigid part of the square; which leads to obtain a structure similar to a chiral system.
Then, the introduction of innovative ligaments at the "joint regions" is the subject of the next section.

5.3 Advanced 2D lattice geometry

5.3.1 A ligament-based rotating squares auxetic structure

In order to improve the mechanical properties of rotating squares auxetic mechanisms (i.e. *E)*, while reducing the dimensions of the system, we need to develop new design solutions which permit high deformation similar to the ones found in an anti-tetrachiral honeycombs and high stiffness similar to that of the rotating structures [120].

Based on previous optimization results, the introduction of "joint regions" with variable shape profiles at the interconnection regions of the mechanism reveals three fundamental aspects:

- The fillet shape introduced at the interconnection regions between the rotating units does not change the auxeticity of the structure;
- The stiffness of the system (i.e. the Young's modulus) is strongly dependent by the size of the square lattice and by the type of ligaments at the interconnection regions;
- The maximum stress along the geometry is affected by the type of connections, and at same time, by the dimensions of the rotating unit.

Ideally, the optimal structure involves a trade-off between metamaterial stiffness and strain tolerance, i.e. one can improve the Young's modulus of the system at the cost of lowering the maximum allowable deformation.

This means that in order to improve the strain tolerance of the overall system while retaining high stiffness, one must endeavor to produce an interconnection geometry which is partially a ligament and a "joint" at the same time.

By keeping in mind the biological solution of variable notch radius [121–123], a novel ligament-based rotating squares auxetic structure at the interconnection regions was developed.

The bio-inspired auxetic structure solution can be used for modelling the new 3D scaffold for vertebral implants, that is the goal of the thesis.

Moreover, two additional issues take into account:

- Type and limits of the additive manufacturing techniques;
- The design solution of the vertebral structure found previously (see Chapter 3).

Furthermore, it is worth noting that customers' requirements are the basic and the objective of our modelling and optimization.

5.3.2 The spline curves fillet geometry

A ligament-based rotating squares architecture is shown in Figure 42.
The geometrical parameters of the RUC of the rotating model (Figure 42.a) are defined as the previous case with the basic lattice geometries in Section 5.2, where L_0 is the side length of a quarter of the RUC and θ is the angle between the rotating units.
However, the ligaments of the simulated cell in Figure 42.b consists of three variables: s, l_a and l_b.
Each ligament connects to the square profile of each simulated cell *via* cubic spline curves, which are three and defined by its spline points, namely:

- Spline curve n°*1* (points P_1, P_2 and P_3);
- Spline curve n°*2* (points P_3, P_4, P_5 and P_6);
- Spline curve n°*3* (points P_7, P_8 and P_9).

To build the geometries, tangency conditions are imposed between the geometrical variables of the unit cell and the ligaments (i.e. points P_1, P_3, P_6, P_7 and P_9 in Figure 42.b).
In order to increase the porosity of the system, according to the target specifications in Section 4.3, the structure is perforated at its center through a circular hole (Figure 42).
Thus, the geometrical parameters of the system were chosen to be as small as possible to push the limits of the additive manufacturing process and obtain the highest mechanical properties possible.
With reference to Figure 42, the geometrical parameters of the unit cell and of the ligament profile are summarized in Table 19.

Table 19 Dimensions of the unit cell with a spline curves fillet at the interconnection regions.

Geometry fillet	l_1 [mm]	L_0 [mm]	θ [deg]	s [mm]	r [mm]	l_a [mm]	l_b [mm]
Spline curves fillet	1.5	3.26	20	0.35	0.45	0.95	0.35

In particular, the thinnest dimension achievable *via* laser sintering fabrication it is (ideally) nearly equal to 350 μm.
However, further consideration on the 3D printing process are given in the following sections.

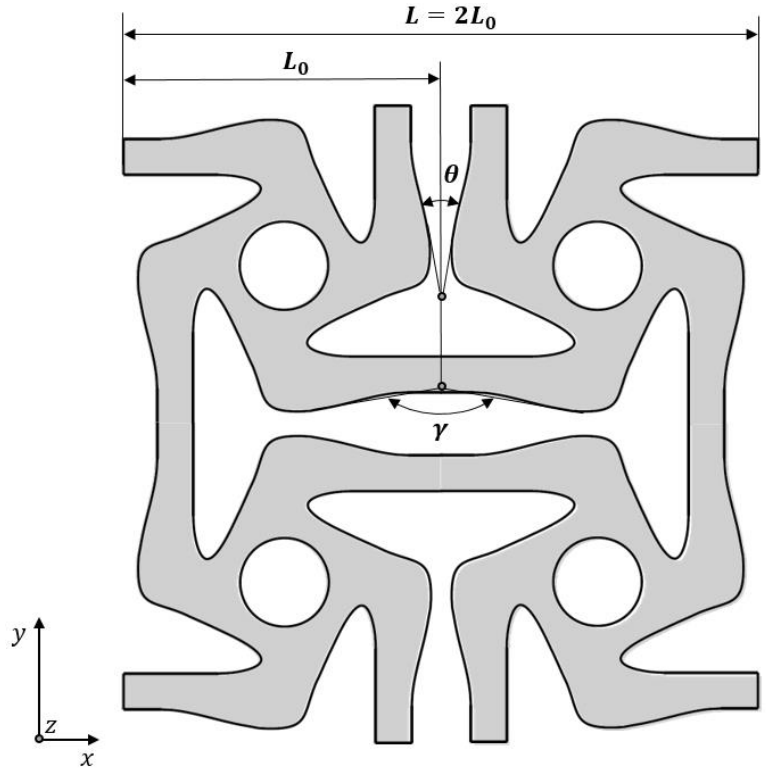

(a)

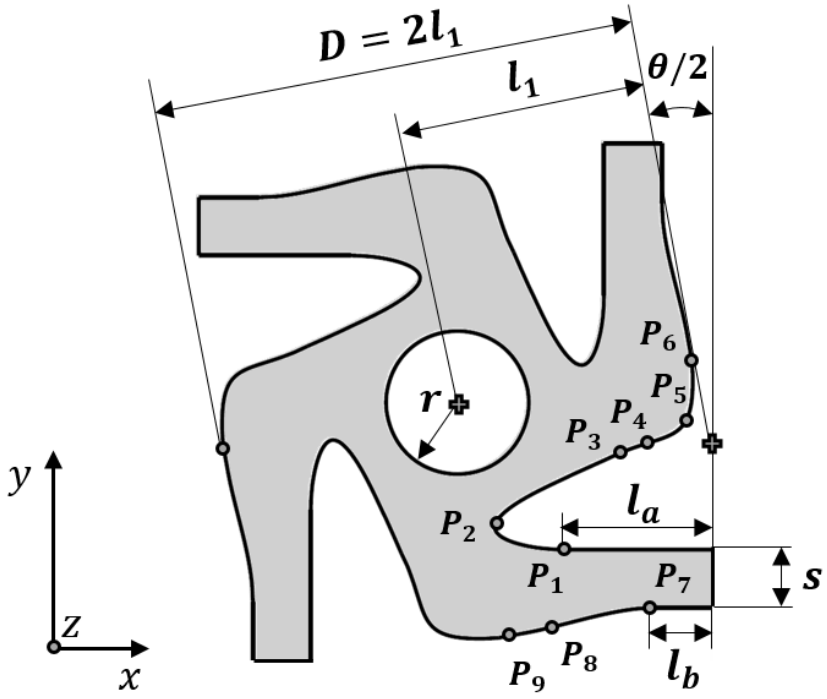

(b)

Figure 42 RUC of the rotating squares system with spline curves profile at the interconnection regions (a) and detailed unit cell (b).

5.3.3 The FE analysis

The FE analysis applied the same loading method, material properties and the prescribed boundary conditions [112, 113] as for the previous basic fillet geometries investigated (see Section 5.2.2). However, the average element side length in the interconnecting regions was set equal to 0.02 mm, while an average side length equal to 0.085 mm was used for the remaining part of the model, see Figure 43.

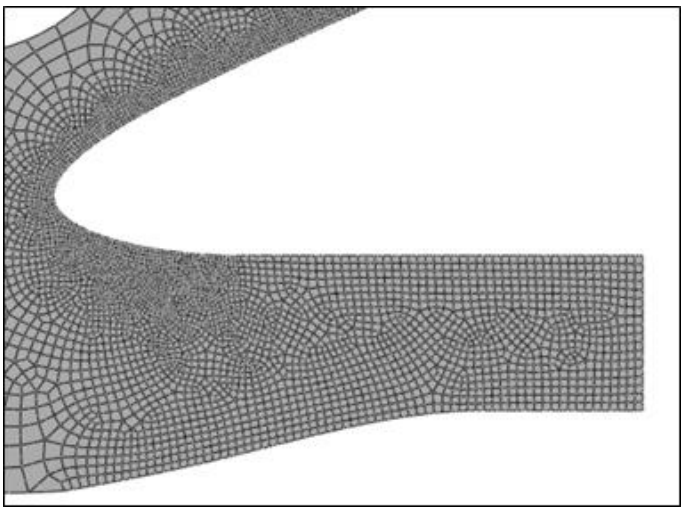

Figure 43 Detail on the FE model mesh with the spline curves profile.

As for the case of the basic fillet geometry solutions, we performed a nonlinear static analysis and calculated the apparent Poisson's ratio, v_{yx}^{*}, the apparent Young's modulus, E_{y}^{*}, and the maximum von Mises stress in the structure, σ_{vm}^{max}.

5.3.4 Numerical results and discussion

Table 20 compares the mechanical properties and the maximum von Mises stress, σ_{vm}^{max}, of the optimal ligament-based metamaterial proposed with the basic fillet shape geometries in Section 5.2: E_{y}^{*} and v_{yx}^{*} were calculated using Eq. 4 and Eq. 5, and $R_s = 1013$ MPa is the yield stress of the titanium alloy [111].

As shown in Table 20, the advance rotating architecture has a PR grather than -0.95, but very low respect to the ligamented auxetic structures. This is given by two reasons. First, by the amount of material removed from the rotating unit cell. Second, by the introduction of ligaments at the interconnection regions in combination to the spline curves profile.

Table 20 Mechanical properties comparison for the 2D auxetic geometries investigated.

Geometry fillet	$\boldsymbol{v_{yx}^{*}}$ [adm]	$\boldsymbol{E_{y}^{*}}$ [MPa]	$\boldsymbol{\sigma_{vm}^{max}}$ [MPa]
Double circular arc	-0.99	42.70	$> R_s$
Combined elliptical and circular fillet	-0.99	31.22	864
Spline curves fillet geometry	-0.93	299	890

Conversely, the system presents high values of the elastic modulus, E_y^*. The increase in stiffness of the structure is mainly attributable to:

- The reduced size of the square lattice;
- By the form of the ligaments.

Specifically, the ligament-based auxetic structure allows an 85% increase of the elastic modulus, E_y^*, compared to the double circular fillet, and an 89% compared to the combined elliptical and circular arcs fillet (see Table 20).

As shown in Figure 44, the optimized ligament-based auxetic structure shown a strength-to-mass ratio higher with respect to the basic fillet geometries, where C_{dc}, C_{ec} and C_s, represent the double circular configuration, the combined elliptical and circular configuration and the spline curves rotating system, respectively.

It comes that the spline curve fillet solution grants a reduction of the structure dimension (i.e. L_0) of 93% compared with the double circular fillet, and of 89% compared to the combined solution (see Figure 44).

Moreover, the peak of the stress is slightly higher than in the combine fillet solution for global elastic strain equal to 3%, but with an higher stiffness of the structure (see Figure 45).

Thus, Figure 46 shows the von Mises stress contour acting on a unit cell for the optimized spline curve fillet profile.

In this regard, the stress contours in Figure 46 highlight increasing local deformations on the whole rotating structure, which is due to the reduced dimensions of the unit cell and by the spline fillet profile introduced.

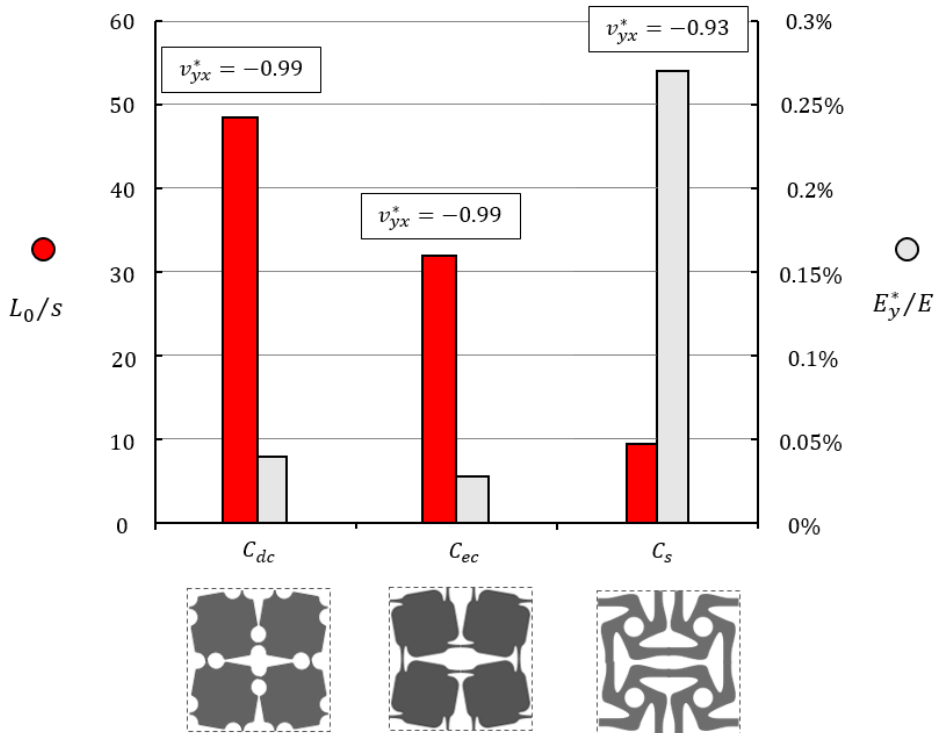

Figure 44 Normalized unit cell dimension, L_0/s, and normalized apparent Young's modulus, E_y^*/E, for the different planar auxetic geometries investigated; where C_{dc}, C_{ec} and C_s, represent the double circular configuration, the combined elliptical and circular configuration and the spline curves rotating system, respectively.

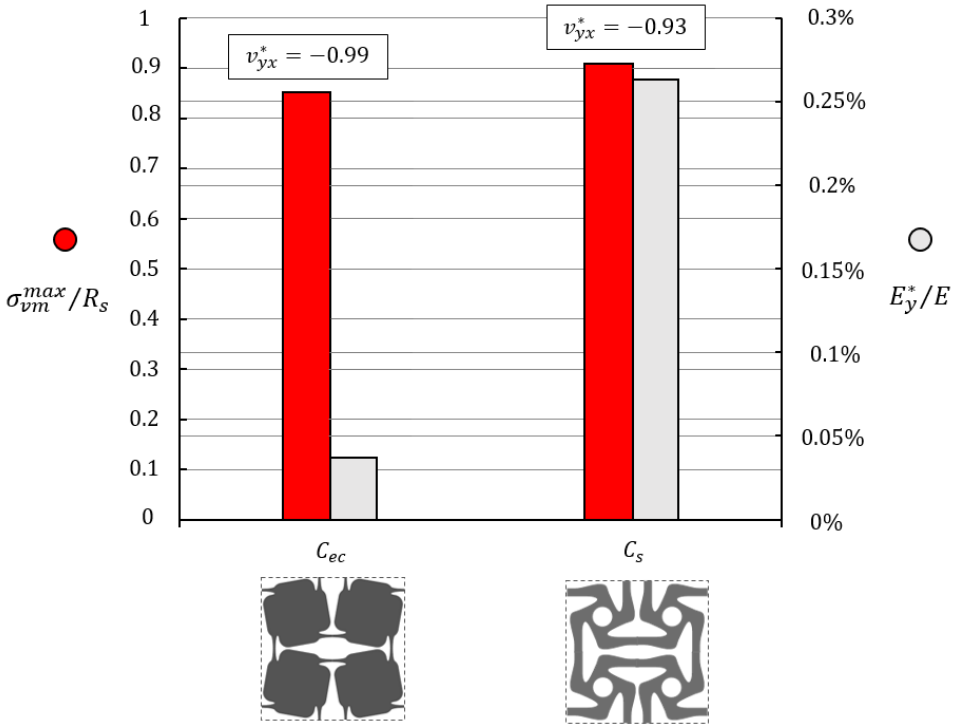

Figure 45 Normalized peak von Mises stress, σ_{vm}^{max}/R_s, and normalized apparent Young's modulus, E_y^*/E, for the optimal basic planar geometry (i.e. the combined elliptical and circular solution, namely C_{ec}) and for the ligamented rotating squares auxetic structure (i.e. C_s).

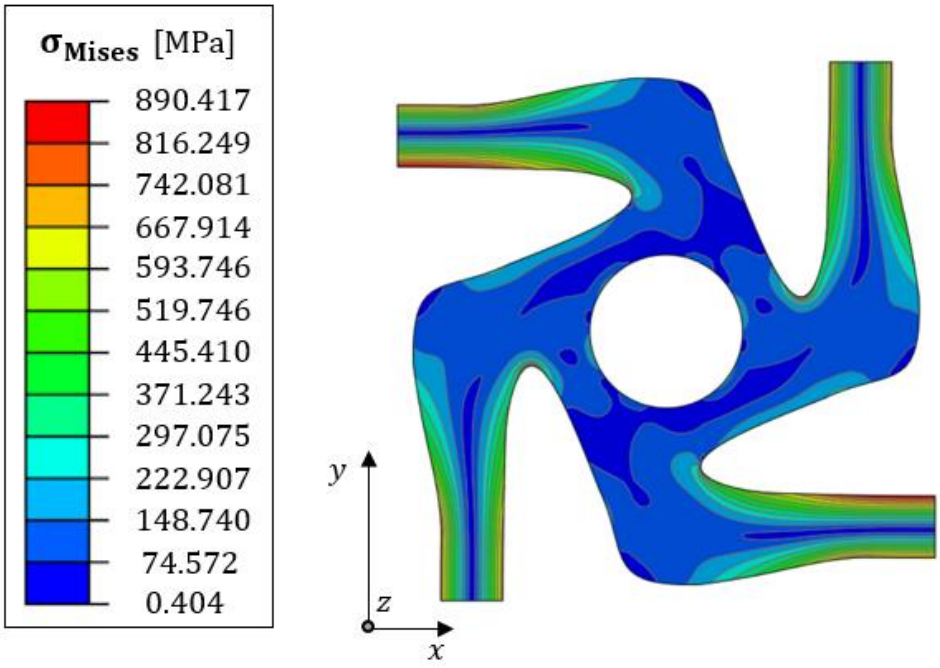

Figure 46 von Mises stress contour for the case of spline curves profile.

Hence, the introduction of these novel ligaments at the "joint regions" can be used for construct the 3D lattice structure for the vertebral implant.

Specifically, the construction of the 3D model uses this type of fillet to connect the face of cuboids along the vertical direction (see Figure 31 and Figure 32).

5.4 Concluding remarks

The chapter examined how an innovative variables arcs fillet solution can improve the structural response of a titanium alloy-based rotating squares metamaterial which is the basis to develop a new vertebral lattice structure.

General considerations and results are summarized as follows:

- Different shape fillet profiles at the interconnection regions of the rotating units have been investigated;
- A novel ligament-based rotating model was developed with the aim to increase the stiffness of the structure and to reduce the dimensions of the system;
- This fillet solution can be used for connect the regions of a 3D auxetic lattice structure ensuring lower stress concentrations due to normal loads for strains up to 3% of the structure.

6 MODELLING, ANALYSIS AND OPTIMIZATION OF 3D ROTATING CUBES AUXETIC GEOMETRY

6.1 Three-dimensional auxetic cubes structure

In this chapter the modelling and the numerical analysis of a novel titanium auxetic lattice structure for vertebral implant is presented and explained.

Once defined the 2D planar rotating metamaterial configuration, the 3D lattice structure with cubes [124] can be developed (see Figure 32).

In order to accomplish the product concept and specifications defined in the conceptual design process, the modelling of the vertebral structure aims to:

- Minimize the dimensions of the unit cells that compose the 3D architecture;
- Maximize the elastic modulus of the system;
- Increase the porosity of the scaffold;
- Maximize the stain tolerance of the mechanism.

However, there are two critical aspects to consider:

- The types of connections between the remaining four vertices of the unit cell (see Figure 31.b);
- The limits of the manufacturing process.

As in the above chapter (i.e. for the planar auxetic systems), the innovative rotating structure can be modelled by the introduction of novel ligaments at the interconnection regions of the auxetic cubes.

With this in mind, it is useful to underline that for mimicking the behavior of the cancellous bones we must balance the geometrical features of the system and optimize the shape fillets at the interconnection regions of the structure.

In particular, the optimal unit cells of the 3D construct are modeled with the commercial CAD/CAE software *Solidworks*.

Thus, an optimized model of the system is presented in the following sections.

6.2 The optimal 3D spline curves fillet model

An optimal representative unit cell (RUC) of the rotating auxetic mechanism based on the 3D construction with cuboids [107] is shown in Figure 47.

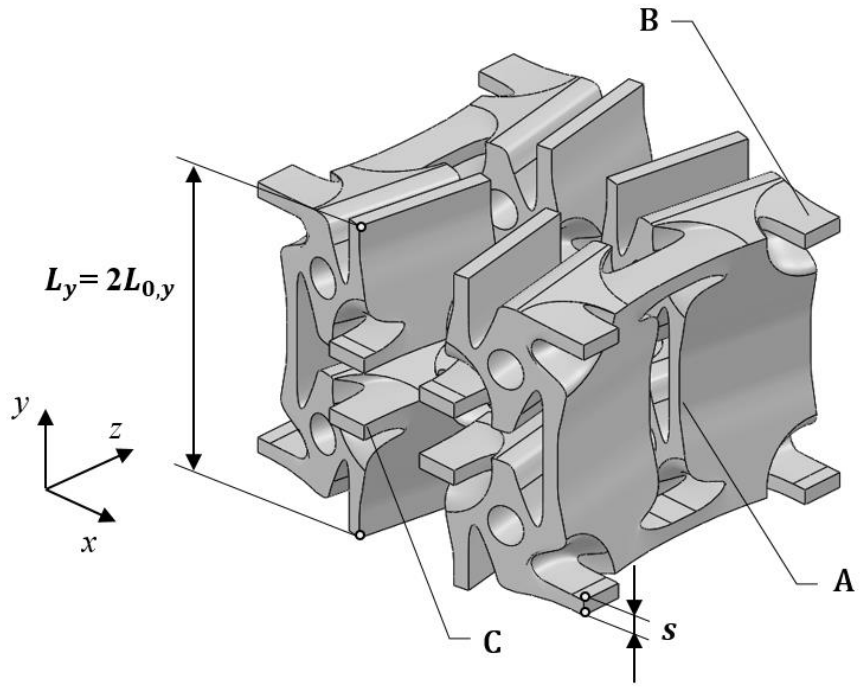

(a)

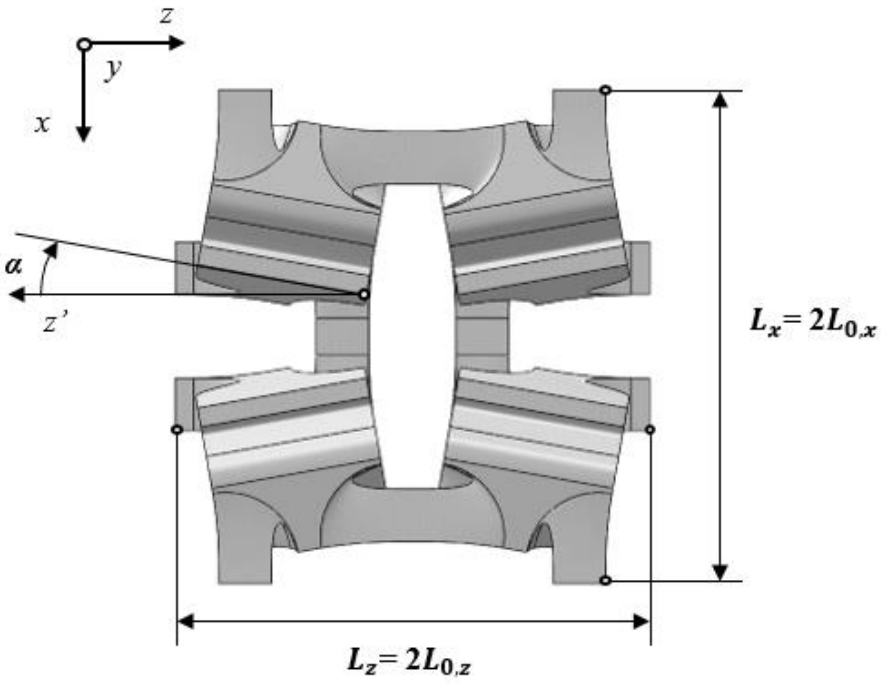

(b)

Figure 47 RUC of the 3D auxetic lattice structure based on cuboids: oblique view (a) and upper view (b).

The RUC consists of eight rotating cubes which are connected as follows.

The ligament s in Figure 47.a connects each cube with three different type of fillets at its vertices and along its shared faces (ligament A, B and C in Figure 47.a).

On one hand, ligament A has the same shape profile (i.e. the spline curve fillet shape geometry) defined previously (see Section 5.3). On the other hand, ligaments B and C were obtained by the introduction of variable spline curves fillets at the interconnection regions.

Specifically, the RUC of the rotating auxetic metamaterial is defined by the volume of the unit cell (see Figure 47), namely:

$$V = L_x L_y L_z \tag{6}$$

Where:

$$L_i = 2 * L_{0,i} \tag{7}$$

and where $L_{0,i}$ is the *i*-th side length of one eighth of the RUC in *x*, *y* and *z*-direction (Figure 47).

The orientation of the each cuboid of the unit cell (i.e. of the RUC) is defined by two angles: first, the angle θ (i.e. the angle between the semi-rigid cubes, see Figure 48); second, the angle α (resulting from a rotation around the *y*-axis in Figure 47.b).

Additionally, each cube is perforated at its center through a circular hole, with $r = 0.45$ mm (see Figure 48).

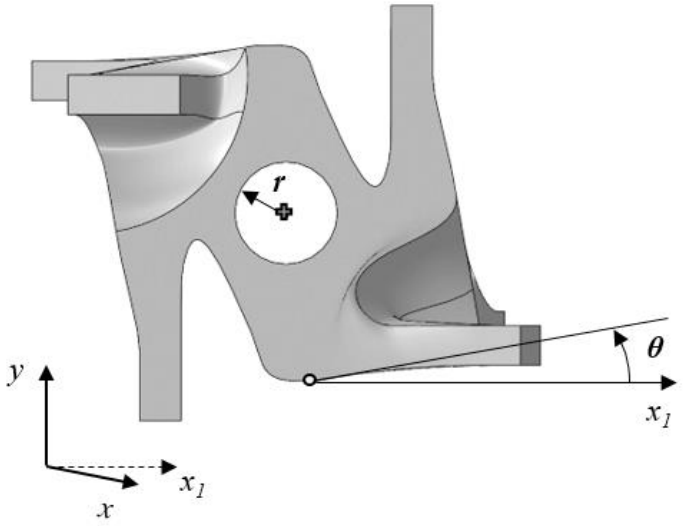

Figure 48 Detail on the angle θ of the auxetic cube.

6.2.1 The FE analysis

Considering that the auxetic structure has three planes of symmetry aligned along each of the three main cartesian planes, xy, yz and xz (see Figure 47); the system was simulated as on eighth of the RUC [113], where s is set equal to 0.35 mm (see Figure 47.a).

Due to the complexity of the geometry, the type of element selected for the mesh was a ten-node tetrahedral element (C3D10 [110]), after conducting the relevant sensitivity tests.

Specifically, mesh refinement was conducted along the relevant stress points of the system, where an average side length equal to 0.04 mm was used, Figure 49.

Figure 49 Rotating cube element with FE mesh.

The material used (i.e. titanium alloy Ti6Al4V) is the same described in Section 5.2.2 (i.e. Young's modulus, E, equal to 110000 MPa, and a Poisson's ratio, ν, equal to 0.3), where the maximum allowable stress (i.e. yield stress), R_s, is equal to 1013 MPa [111].

With reference to Figure 50, boundary conditions were applied to the model based on the same approach implemented for the 2D geometries [113] (see Chapter 5).

In particular, the system was loaded through the application of a displacement, u_y, on the top horizontal nodes (s_h^t in Figure 50). The displacement was proportional to the original side length of the rotating cuboid (i.e. $L_{0,y}$ in Figure 47), according to the following relationship:

$$u_y = L_{0,y}\,\varepsilon_y \tag{8}$$

where $\varepsilon_y = 3\%$ is the global strain applied on the cuboid in the y-direction, as defined in the target specifications in Table 13.

In order to implement the periodic symmetry of the rotating cube of the RUC [113], the auxetic cuboid is simply supported in the nodes at the bottom horizontal face (s_h^b in Figure 50), on the top vertical face (s_v^t in Figure 50) and on the right vertical face (s_v^r in Figure 50). Additionally, the nodes of the remaining faces are coupled to retain their planar shapes.

Specifically, the nodes on bottom vertical face (s_v^b in Figure 50) were coupled for equal displacement in *x*-direction; and the nodes on the left vertical face (s_v^l in Figure 50) were coupled for equal displacement in *z*-direction.

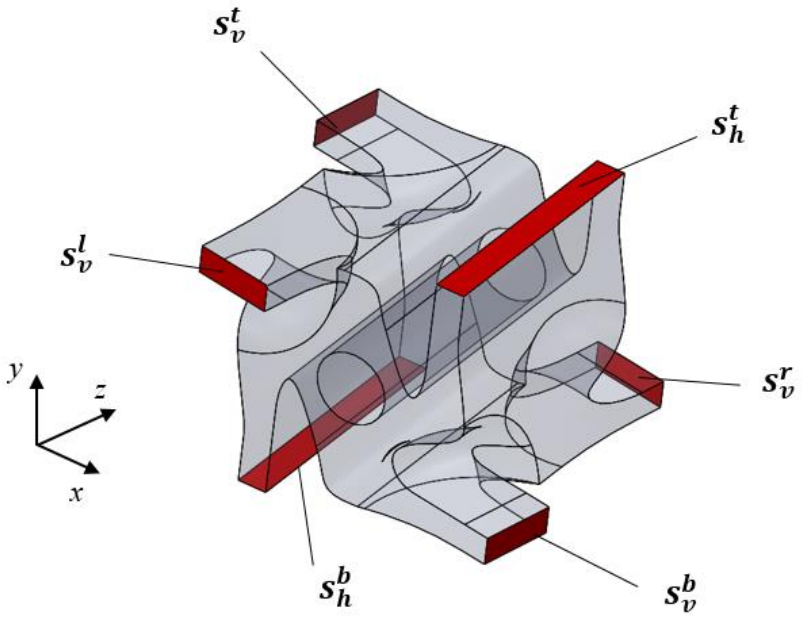

Figure 50 Face sets of the FE model.

Then, the nonlinear static analysis calculated the apparent Young's modulus of the system, E_y^*, namely:

$$E_y^* = \frac{\sum RF_{y,i}}{L_{0,x}\, L_{0,z}\, \varepsilon_y} \tag{9}$$

where $RF_{y,i}$ is the reaction force in the y-direction of the *i*-th node in the loaded face ligament (s_h^t in Figure 50); and where $L_{0,x}$ and $L_{0,z}$ are the original side lengths of an eighth of the RUC in *x* and *z*-direction, respectively (see Figure 47).

However, due to the anisotropy of the cuboids [124], the analysis calculated the apparent Poisson's ratios as:

$$v_{yx}^{*} = -\frac{u_x L_{0,y}}{u_y L_{0,x}} \tag{10}$$

And

$$v_{yz}^{*} = -\frac{u_z L_{0,y}}{u_y L_{0,z}} \tag{11}$$

where u_x and u_z represent the resultant displacements of the nodes on the bottom vertical face in the *x*-direction (s_v^b in Figure 50) and of the nodes on the left vertical face in *z*-direction (s_v^l in Figure 50), respectively.

Finally, the nonlinear static analysis calculated the maximum von Mises stress in the system, σ_{vm}^{max}.

6.2.1.1 Lattice structure configurations

An increase of stiffness of the structure can be obtained by reducing the dimensions of the cuboids (see Eq. 6-7) which are defined by the value of $L_{0,x}$, $L_{0,y}$ and $L_{0,z}$ of the rotating unit (see Figure 47). Once reducing the dimension of the system to be as small as possible to push the limits of the additive manufacturing while avoiding peak of the stress on the system, we considered a fixed value of the angle θ equal to $20°$ between the rotating units as defined in Section 5.3 (see Figure 48).

In order to assess the mechanical properties of the auxetic system, we investigated three levels of the angle α of the lattice structure, from $10°$ to $30°$ [125] (see Figure 47.b).

Then, for each configuration investigated we calculated the porosity, P, of the lattice structure as:

$$P = \left(1 - \frac{\rho}{\rho_o}\right) * 100 \tag{12}$$

where ρ is the apparent density and ρ_o is the bulk alloy density of the titanium (i.e. $4.42\ \mathrm{g/cm^3}$).

Table 21 reports the main geometrical parameters and features of the cuboids investigated through the FE analysis, where the porosity (i.e. P) was calculated using Eq. 12.

Table 21 Rotating model configurations investigated through FE analysis.

Geometry configuration	$\boldsymbol{\theta}$ [deg]	$\boldsymbol{\alpha}$ [mm]	$\boldsymbol{L_{0,x}}$ [mm]	$\boldsymbol{L_{0,y}}$ [mm]	$\boldsymbol{L_{0,z}}$ [mm]	$\boldsymbol{P}$ [%]
$\boldsymbol{C_{3D,1}}$	20	10	4.51	3.65	4.69	72
$\boldsymbol{C_{3D,2}}$	20	20	4.65	3.65	4.88	74.5
$\boldsymbol{C_{3D,3}}$	20	30	4.96	3.65	5.14	77

6.2.2 Numerical results and discussion

Table 22 compares the mechanical properties of the rotating model configurations investigated through FE analysis (see Table 21); where, E_y^*, v_{yx}^* and v_{yz}^* were calculated using Eq. 9-11.

Table 22 Mechanical properties comparison for the 3D auxetic geometries investigated.

Geometry configuration	$\boldsymbol{v_{yx}^*}$ [adm]	$\boldsymbol{v_{yz}^*}$ [adm]	$\boldsymbol{E_y^*}$ [MPa]	$\boldsymbol{\sigma_{vm}^{max}}$ [MPa]
$\boldsymbol{C_{3D,1}}$	-0.789	-0.127	101.2	867
$\boldsymbol{C_{3D,2}}$	-0.726	-0.247	97.3	870
$\boldsymbol{C_{3D,3}}$	-0.635	-0.329	90.0	872

In particular, three observations can be made from Table 22.

First, the Poisson's ratio, v_{yx}^***,** is very close to -0.8 for small values of the angle α, which corresponds to an higher value of the Poisson's ratio in the other transverse direction, namely v_{yz}^* (first line in Table 22).

Otherwise, the increase of the angle α corresponds to an increase of v_{yx}^* and consequently to a decrease of the PR in the opposite transverse direction, v_{yz}^* (second and third line in Table 22).

Second, Table 22 highlights that the apparent Young's modulus, E_y^*, is very similar between the three geometry configurations: 101.2 MPa for the configuration $C_{3D,1}$, and 90 MPa for the configuration $C_{3D,3}$. Those values were within the range of the Young's moduli of human trabecular bone [23].

Three are the geometrical parameters that affect the value of E_y^*: first, the volume of the cuboid (which is depended by the *i*-th side length of the rotating unit); second, the angle α; and third, the shape of the ligaments at the interconnection regions between the rotating units.

Moreover, in order to further increase of the elastic modulus of the lattice structure, one may change the angle θ between the rotating units for fixed value of α.

Third, the peak of the stress are nearly the same for the all the configurations investigated for global elastic strain equal to 3%, see Table 22.

In this regard, the increase of the angle α does not change the value of the peak stress on the structure, although the stiffness of the system decrease (see Figure 51).

Thus, the porosity of the lattice geometries investigated (i.e. P in Table 21) are about the same (or higher) respect to the target specifications defined in the design process in Section 4.3 (see Table 13). These values of porosity are within the range of porosity of the actual lattice structure with gyroids scaffold [13, 76].

However, the variation of Poisson's ratios are strongly related to angle α (see Figure 52).

Specifically, this variation can be summarized as follow:

- Increase of angle α leads to increase of the PR in the *yx* plane (i.e. v_{yx}^*);
- Increase of angle α leads to decrease of the PR in the *yz* plane (i.e. v_{yz}^*).

Thus, Figure 53 shows the von Mises stress contour acting on the 3D lattice structure for different values of angle α.

Specifically, the changing the dimension of the cuboids in one direction, and of angle α, leads to an increase of the stress in the corresponding ligaments of the rotating unit (see Figure 53).

As a result, the stress contours in Figure 53 highlight increasing local deformations on the whole rotating structure, especially in the case of high value of the angle α.

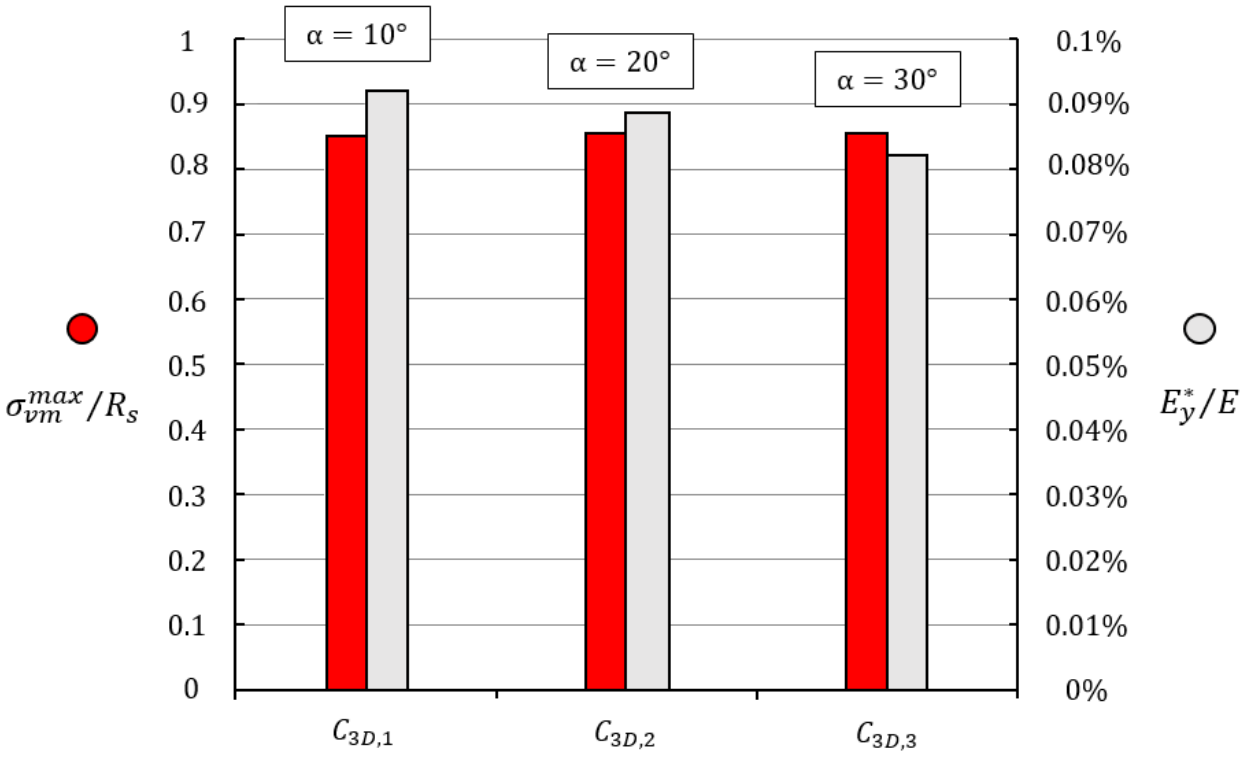

Figure 51 Normalized peak von Mises stress, σ_{vm}^{max}/R_s, and normalized apparent Young's modulus, E_y^*/E, for the 3D rotating model configurations of the lattice structure in Table 21.

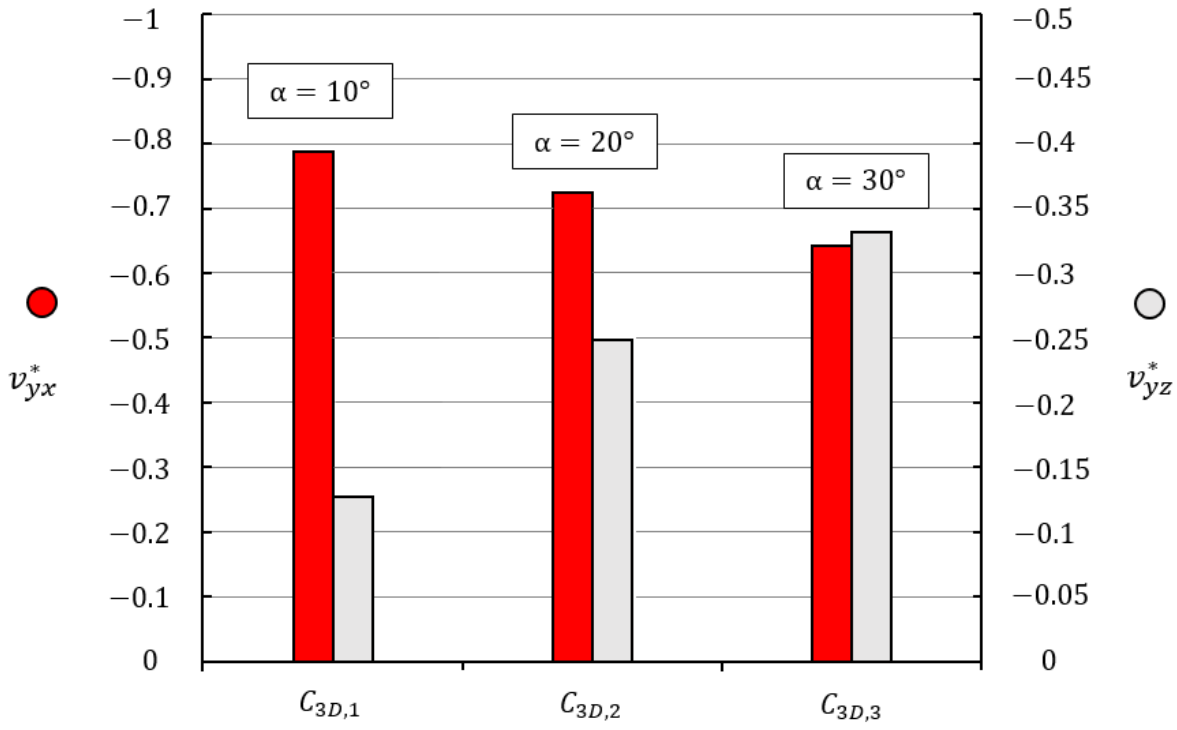

Figure 52 Variation of the apparent Poisson's ratios, v_{yx}^* and v_{yz}^*, of the 3D rotating model configurations of the lattice structure in Table 21.

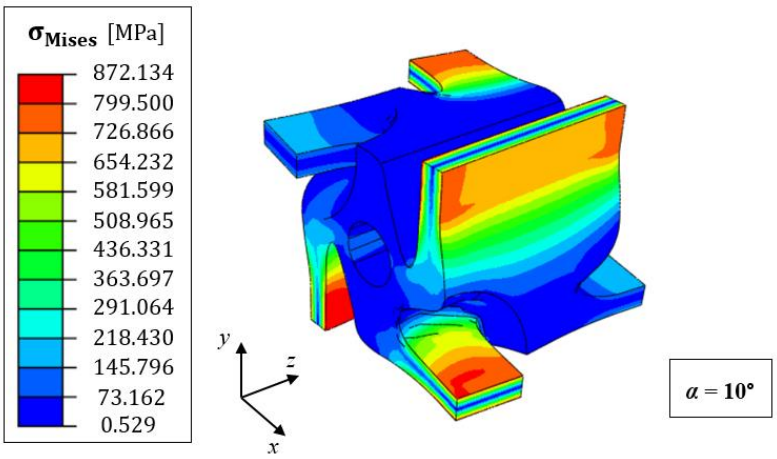

(a)

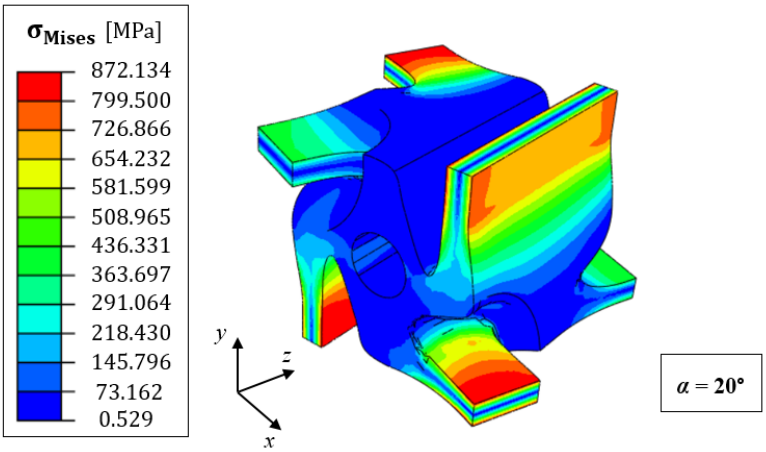

(b)

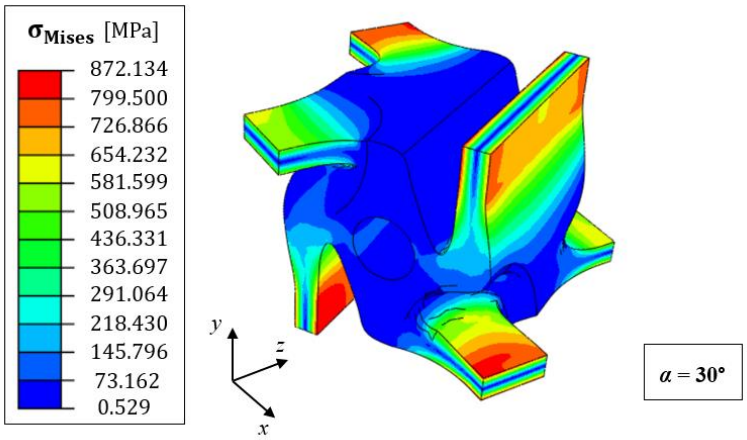

(c)

Figure 53 von Mises stress contour of the lattice structures investigated in Table 21 for different value of angle α: 10° (a), 20° (b) and 30° (c).

6.3 Concluding remarks

General considerations and results of modeling and analysis of a new vertebral lattice structure are summarized as follows:

- The 3D model of the vertebral lattice structure can be obtained by the combination of different types of ligaments and fillets at the interconnection regions of the structure;
- Numerical results show that a novel ligament-based rotating structure can reduce the size of the system, while maximizing the stiffness of the lattice structure for strains up to 3%.

However, the new lattice structure consists of a ligament-based auxetic cuboids with optimized mechanical properties which mimic the behavior of the vertebral cancellous bone.
Thus, the mechanical properties of the system designed satisfy the target specifications defined previously (see Table 12). In particular, Table 23 compares the main mechanical properties (obtained through numerical analysis) of this new lattice structure (our final product design) with the final target specifications of the system of Table 12.

Table 23 Mechanical properties comparison between the final product design and the target specifications of Table 12.

	E_y^* [MPa]	ε_y [%]	P^* [%]
Target specifications	≥ 75	3	70
Final product design	$90 \div 102$	≥ 3	$72 \div 77$

Once defined the lattice structure configuration, a prototype of the scaffold can be fabricated and tested, that is the subject of the next chapter (the "*Experimental validation"* Chapter).

7 EXPERIMENTAL VALIDATION

In this chapter, the prototyping and the experimental validation of a novel titanium auxetic lattice structure for vertebral implant is presented and discussed.

Specifically, the validation focuses on the optimal 3D lattice structure identified through the FE analysis in the previous chapter.

However, in order to avoid poorly fabricated solutions and failures, the experimental validation focused on the lattice structure geometry with an angle $\alpha = 30°$ (see Table 21), which has more homogeneous mechanical properties (i.e. v_{yx}^{*} and v_{yz}^{*}) respect to the other lattice structure configurations investigated (see Table 22).

In particular, the prototype of the lattice structure was developed in collaboration with the additive manufacturing company *ZARE Prototipi* ("*BEAMIT-ZARE*" group) in Reggio Emilia.

7.1 Prototype development

Using the optimal dimensions of the RUC reported in Table 21 (i.e. the configuration $C_{3D,3}$), we manufactured a prototype from the biological-grade titanium alloy (Ti6Al4V ELI) through the selective laser melting (SLM) 3D-printing technique using a *M2 Dual Laser* machine (Concept Laser), where the size of the powder is equal to 25 μm.

Specifically, the prototype is composed by a $9x5x5$ RUC of the system with a rectangular cross-section according to the standard ISO 13314 [126] (see Figure 54.a and Figure 54.b).

After manufacturing, the sample was removed from its build plate and a sandblasted process was performed in order to remove excessive powder.

The size of the ligaments was measured through an optical microscope, and the measurements were processed through the software *Image J* [127], in order to obtain the dimension of the ligaments (see Figure 54.c). Specifically, the dimensions measured values differ less than 5% from the nominal value of the ligament, that is equal to 350 μm.

Thus, in order to obtain the porosity of the lattice structure, P in Eq. 12, the prototype was measured and weighted on a precision balance scale.

Table 24, shows the porosity (i.e. P) and the prototype dimensions of the lattice structure compared to those one obtained from the CAD model: $L_{i,s}$ represents the i-th side length of the sample in x, y and z-direction (see Figure 55), and $A_{xz,s}$ represents the cross-section area of the prototype.

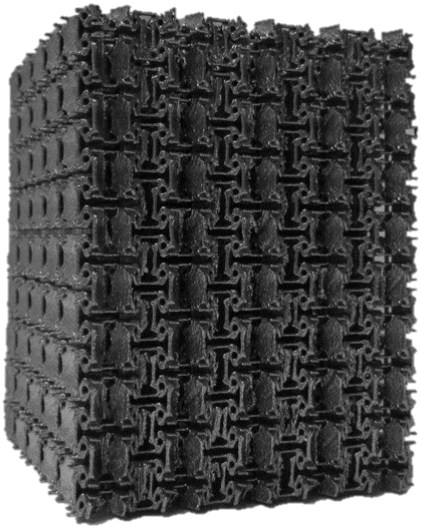

(a)

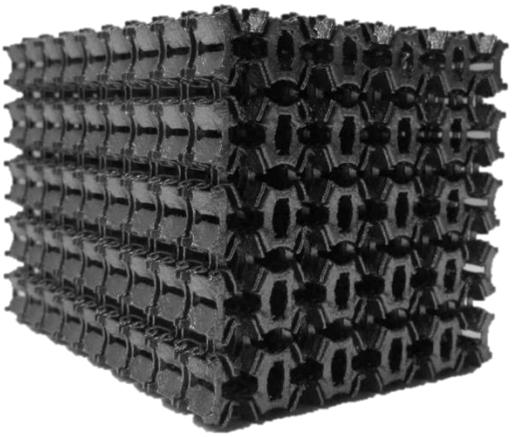

(b)

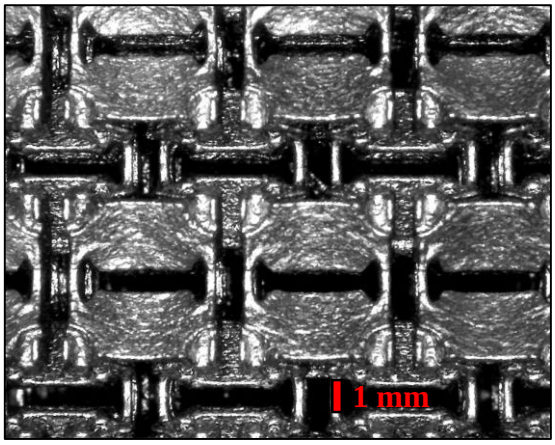

(c)

Figure 54 3D-printed prototype of the lattice structure: oblique view (a), upper and lateral view (b) and detail on the ligaments of the rotating cuboids (c).

Table 24 Comparison between the CAD model and the prototype manufactured.

	$L_{x,s}$ [mm]	$L_{y,s}$ [mm]	$L_{z,s}$ [mm]	$A_{xz,s}$ [mm^2]	P [%]
CAD	51.39	65.70	49.60	2548	76
Prototype	51.02	65.04	49.04	2500	74

As shown in Table 24, the relative difference in the porosity between the CAD model and the prototype is lower than 3%.

7.2 Experimental procedure

In order to assess the elastic modulus, E_y^*, of the lattice structure, the prototype was uniaxially compressed using a *MTS Bionix* servohydraulic testing machine with a 25 kN loadcell, controlled by a PC equipped with the proprietary software (see Figure 55).

The quasi-static tensile test applied a 1.97 mm stroke to the sample at a rate of 1 mm/min, which corresponds to an overall global strain of the sample equal to 3%.

Since we focused on the Poisson's ratios of the lattice structure, the digital image correlation (DIC) technique was used for measuring the displacement field of the central RUCs of the sample along the two planes of the structure (plane *yx* and plane *yz* in Figure 55).

DIC images were acquired using a *Dantec Dynamics* camera and analyzed the response through the *GOM Correlate* software and *Python* scripts [116].

In particular, the speckle patterns required for DIC measurements were created by initially painting the specimens in black, then applying a white paint on the front surface of the specimens, and ultimately spraying random black dots, Figure 56 [128].

Three replications of the test were performed for both the planes of the structure evaluated on the same sample, according to the standard ISO 13314 [126], for a total of six tests.

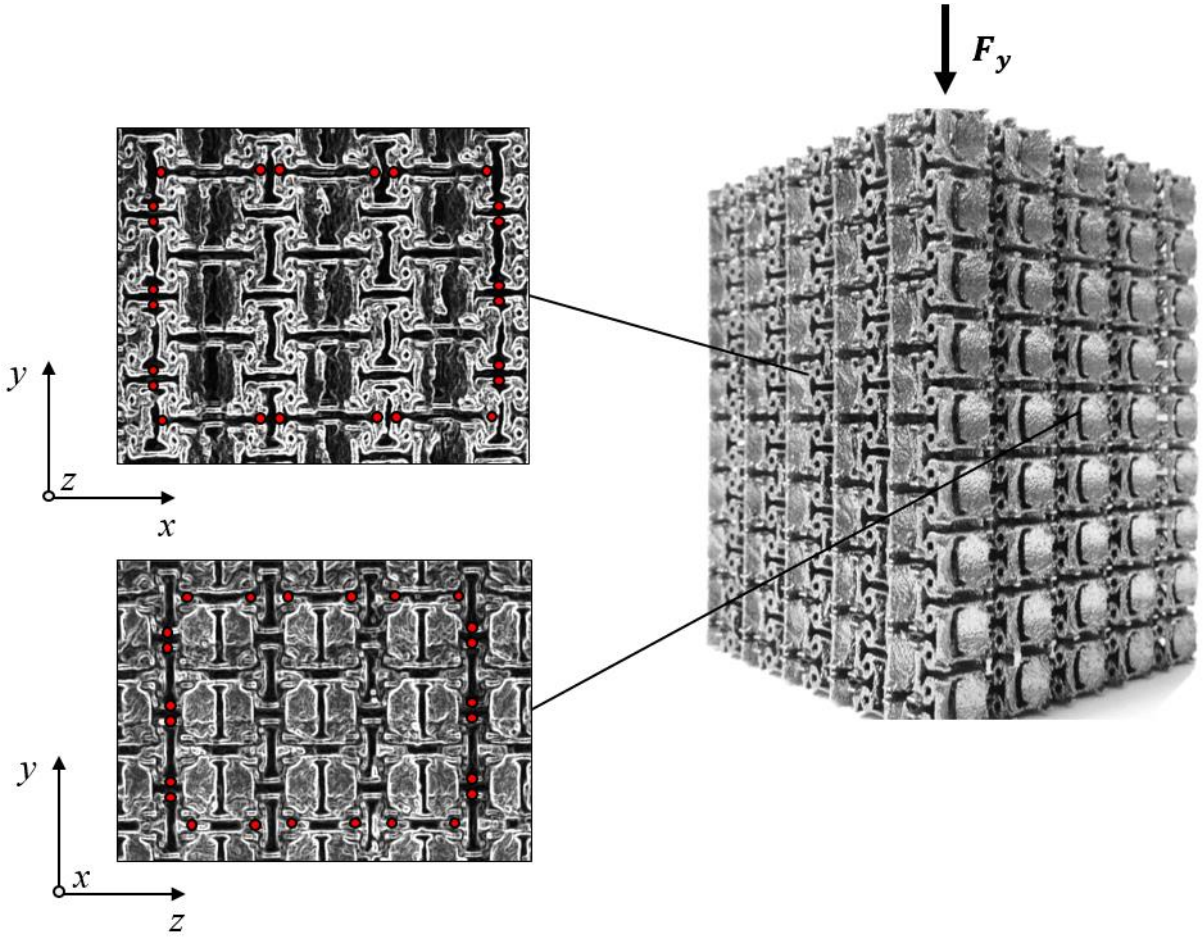

Figure 55 Central RUCs of the sample on the two planes of symmetry with the points used for tracking the displacement.

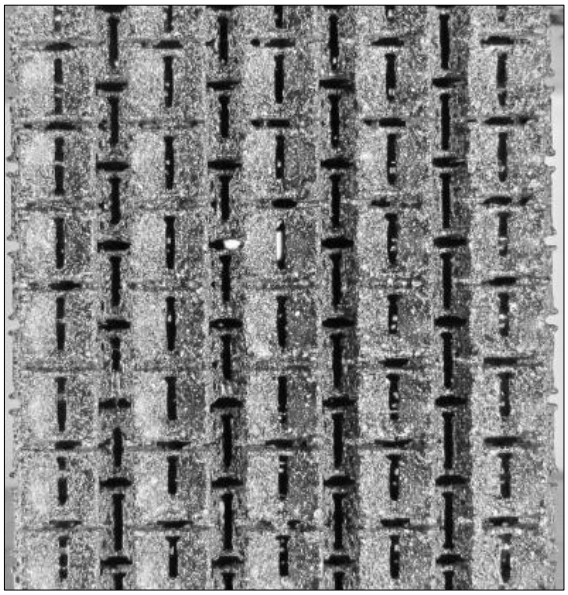

Figure 56 Speckle pattern added with airbrush.

7.3 Experimental results and discussion

7.3.1 Elastic modulus

The apparent Young's modulus of the system (E_y^*) was obtained with graphic method [129].

In particular, from force versus displacement data obtained from the compressive tests acquisitions (see Figure 57), it is possible to calculate the elastic modulus of the system as the gradient of the most linear part of each curve, in accordance with the initial cross sectional area and the initial length of the structure (see Table 24).

In this regard, Table 25 compares the experimental and numerical value of E_y^* of the lattice structure investigated.

Table 25 Numerical and experimental elastic modulus of the lattice structure.

	Numerical	**Experimental**
$\boldsymbol{E_y^*}$ [MPa]	90	116 ± 9.3

As shown in Table 25, the experimental results exhibit a good agreement with the numerical predictions, where the relative difference between the experimental measurements and numerical values of the elastic modulus is lower than 23%.

In particular, the elastic modulus obtained experimentally is similar to that of the human trabecular bone [19], that is one of the target specification of the conceptual design in Chapter 3.

Except in the first stretch of the curve in Figure 57, the lattice structure exhibits a linear elastic behavior up to a 3% overall strain; that is significantly higher than the allowable elastic strain of the titanium alloy.

However, the lattice structure tested experimentally is stiffer respect to the numerical model (see Figure 57).

The differences between the FE method and the compression tests are not attributable to a single parameter, but to several of them. Specifically, a small variation on the dimensions of the lattice structure, can leads to increase of the elastic modulus of the system (see Table 21 and Table 22), as well the effects due to the boundary conditions.

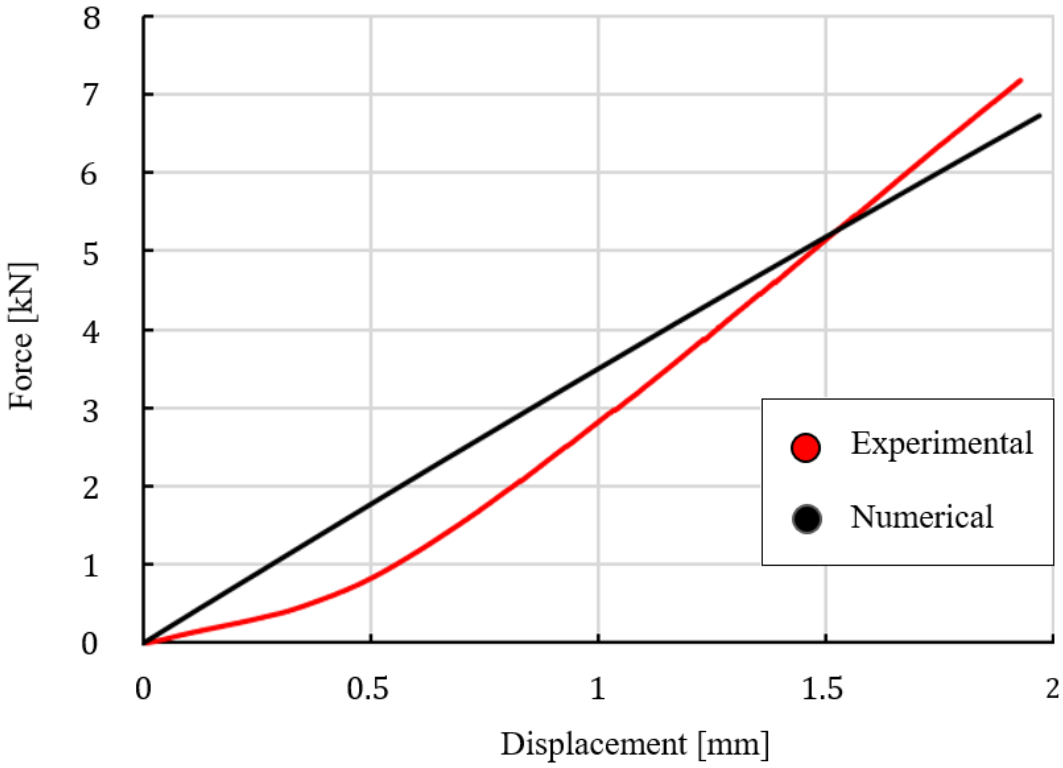

Figure 57 Comparison between the numerical and experimental force-displacement curve of the lattice structure up to a 3% overall strain.

Then, the size of the specimen becomes critical in order to estimate the correct elastic modulus of the scaffold. Hence, the surface roughness or variations in the volume of the cuboids randomly produced in the manufacturing process are not found in the FE model. Thus, some of those imperfections, inherent to the manufacturing process, might be improved by heat treatment.

Additionally, the value of the elastic modulus of the material used in the FE models, may not match the real modulus of the alloy.

In this regard, the increase of the elastic modulus of titanium (E) in the numerical models, corresponds to an increase of the apparent modulus (E_y^*) up to 100 MPa, where the relative difference between the experimental measurements and numerical values of the apparent elastic modulus is lower than 14%.

Furthermore, the porosity of the sample (i.e. P in Table 24) is about the same respect to the target specifications defined in the design process in Section 4.3 (see Table 13), which leads to an increase of the bone ingrowth inside the scaffold.

7.3.1 Poisson's ratios

Figure 58 and Figure 59 compares the initial configuration (Figure 58.a and Figure 59.a) with the final configuration (Figure 58.b and Figure 59.b) of the sample along the two planes of the structure. As one may observe, by comparing the initial and final step of the test in Figure 58 and Figure 59, it clearly appears the auxetic response of the prototype.

However, by tracking the displacements components (axial and transverse direction) of the markers point on the central RUCs for both the planes (red dots in Figure 55), the DIC calculated the Poisson's ratios of the sample [120].

Specifically, Table 26 compares the numerical and experimental apparent Poisson's ratios of the lattice structure.

Table 26 Comparison between the numerical and experimental PRs of the lattice structure.

	Numerical	**Experimental**
$\boldsymbol{\nu_{yx}^{*}}$ [adm]	-0.635	-0.615
$\boldsymbol{\nu_{yz}^{*}}$ [adm]	-0.329	-0.319

As shown in Table 26, the experimental PRs obtained through the DIC analysis were in accordance with the FE results, for global strains of the structure up to 3%.

This is not surprising considering the peculiar kinematic response of the lattice structure and the way in which the ligaments connects the rotating cuboids [107].

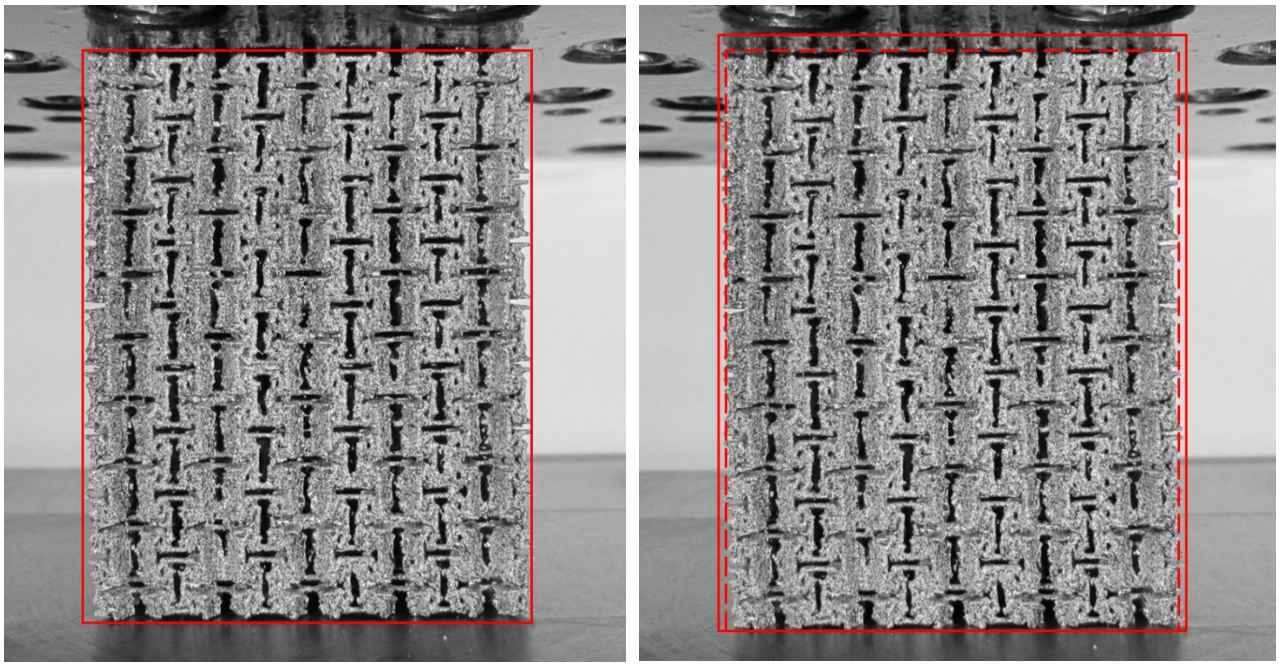

(a) (b)

Figure 58 Initial (a) and final (b) configuration of the sample in *yx* plane.

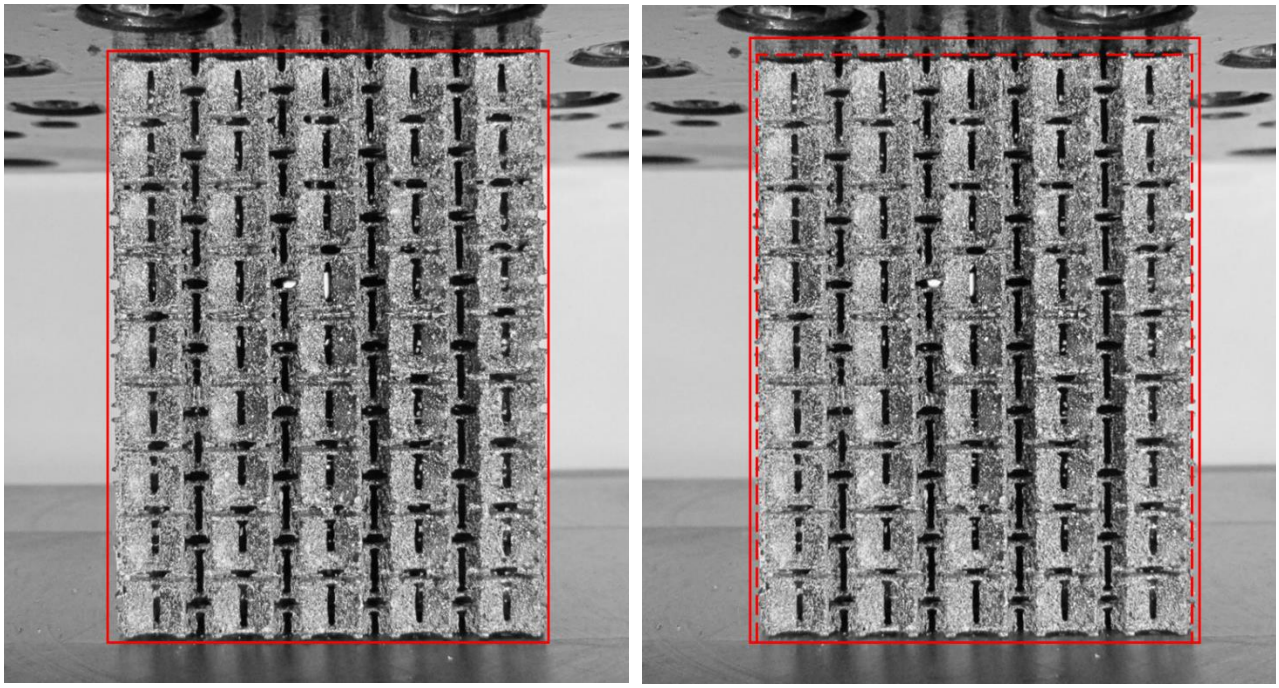

(a) (b)

Figure 59 Initial (a) and final (b) configuration of the sample in *yz* plane.

7.4 Concluding remarks

In this chapter, we experimentally investigated the mechanical behavior of a novel auxetic lattice structure for human cancellous bone vertebral implants.

To assess the structural response of the proposed architecture, we manufactured a prototype in titanium alloy material (Ti6Al4V ELI) through the SLM 3D-printing technique and performed a compressive test by measuring the displacement field of the specimen through digital image correlation (DIC).

The main results and considerations can be summarized as follow:

- The experimental results exhibit a good agreement respect to the numerical models, in terms of stiffness and Poisson's ratios;
- This new lattice structure allows an overall 3% elastic strain of the system due to normal loads;
- The elastic modulus of the system is similar of Young's moduli of human trabecular vertebral bones, which allows to reduce the stress shielding phenomena, in accordance to the target specifications defined in the conceptual design;
- Additionally, the system can withstand to compressive loads more than 2000 N, while mimicking the spongy bone behavior of the human vertebral bones;
- Then, the system has a great pore size that increase the bone tissue regeneration inside the scaffold.

8 GENERAL DISCUSSION

The chapter briefly describes and discuss the methods and the results of the design and the additively manufactured of a novel lattice structure for lumbar vertebral implants.
In particular, it is interesting to evaluate the final concept specifications in relation to the target values defined in the conceptual design process.
It is worth pointing out that the presented results are strongly correlated to a specific design concept of a vertebral cage with peculiar features and architecture, which has been defined during the conceptual design process.
However, the rational design methodology employed in the work promotes the generation of new concepts and consider the most critical factors during the design and development of this innovative product.
Thus, specific considerations and performances of the system are summarized below.

8.1 The conceptual design process

The rational design of a novel titanium lattice structure for vertebral cages regards an efficient and robust design process, which takes into account the most critical factors of the vertebral body resection and the interactions between the different parts that compose the vertebral prosthetics (or cage).
Moreover, the methodology adopted can be divided in three macro-steps:

- How to structure the design process;
- Generating new ideas;
- Evaluate and make decisions.

Thus, in order to avoid poor design solutions for the vertebral scaffold (i.e. our objective problem), we need to focus on the entire vertebral prosthetic (i.e. our macro-objective problem) during the conceptual design.
In this way, the design reveals two fundamental aspects:

- The biomechanical behavior of a general vertebral cage is strongly affected by the typology of implant (e.g. 3D-printed cages or distractible implants);
- The surgery approach and post-operative complications are varied.

Consequently, in consideration of the mechanical problem defined, the target specifications for the vertebral scaffold are a subclass of the target specifications of the prosthesis (e.g. the elastic modulus, the size of the lattice configuration or the strain tolerance).
This is particularly pertinent in the case of titanium vertebral prosthetics fabricated via AM.
However, since the constraints of the problems seem to reduce the design solutions space, the final concept of the lattice system is generated from the combination of different type of ideas and design solutions, that are, generally, in conflict with one other.
Specifically, the final product retrieved from decision making matrices, consists of a semi-modular system that can be divided into three parts:

- An auxetic lattice structure (the objective of this work and design);
- An additional outer shell (likewise auxetic);
- And a removable part which has the function to avoids any tissue migrations inside the scaffold.

In this regard, the auxetic solution help us to increase the biomechanical behavior of the scaffold, and at the same time, to design a minimally invasive vertebral prosthetic which mimic the behavior of the vertebral cancellous bones.
Then, the identification of a new auxetic lattice system is focused on the rotating auxetic metamaterials, which show more prospective mechanical properties and functionalities respect to the ligamented auxetic structures.
Furthermore, the final target specifications for the scaffold are fixed at this stage.

8.2 Modeling, analysis and prototype of a novel lattice structure

The modelling and analysis of this new type of structure was quite a challenge, and focuses on the types of connections at the interconnection regions between the rotating units that composes the 3D construct which consists of auxetic cuboids made of titanium.
In this sense, the final lattice structure of the system can be constructed by the combination of different type of geometric fillet profiles and involves both planar (2D) and 3D models of the auxetic metamaterials. In order to increase the strain tolerance of the structure, the modelling and the numerical analysis of the 2D rotating squares system investigates three different types of fillet at the interconnection regions: first, a double circular profile; second, a combined elliptical and circular fillet; and third, a ligament-based “joint” with a spline curves profile.

Since the basic fillet geometries investigated (i.e. the double circular fillet and the combined arcs solution) have higher stiffness compared to the chiral systems and re-entrant auxetic structures, only the novel proposed ligamented rotating units can simultaneously:

- Strongly reduce the dimensions of the lattice structure (that is crucial for accomplish the target values and constraints of the system);
- Increase the strain tolerance of the scaffold for global strain up to 3%.

Thus, the 3D vertebral lattice structure of the system consists of a ligament-based rotating cuboids with optimized mechanical properties.

According to the FE results, the optimal configuration identified allows an overall 3% elastic strain of the metamaterial, with an elastic modulus similar to that of vertebral trabecular bone.

However, the final milestone of this design was to fabricate a prototype of the scaffold made of titanium (Ti6Al4V ELI) through the SLM 3D-printing technique with the aim to push the limits of the additive process.

The sample was tested with a tensile loading device and digital image correlation measurements were performed.

Specifically, Table 27 compares the main mechanical properties of the lattice structure obtained numerically and experimentally with the final target values defined in the conceptual design process.

Table 27 Comparison between the numerical, experimental and target values of the auxetic metamaterial lattice structure.

Parameters	Target value	Numerical	Experimental
Maximum compressive load [N]	1888	≥ 2000*	≥ 2000*
Compression [%]	3	3.5	≥ 3
Elastic modulus [MPa]	≥ 75	90-100	116
Porosity [%]	≥ 70	76	74

As shown in Table 27, the experimental results confirmed the numerical predictions in terms of mechanical properties, such as elastic modulus and global strain. By comparing the proposed solution with the actual VBR lattice structures from the literature, it appears a noticeable stress reduction with improved biomechanical properties that mimic the cancellous bone behavior and with great pore size that increase the bone tissue regeneration inside the scaffold.

*Considering a minimum cross-section area composed by a 3x3 RUC system (see Table 21).

8.3 Perspectives

As mentioned earlier, in order to develop a new vertebral implant, we must to consider the integration of an auxetic shell surrounding the lattice structure, in combination with a protective oval-shaped part which prevents any tissue migrations inside the implant (see Figure 60).

In consideration of the design product obtained and of mechanical constraints, the vertebral prosthetic can be made by assembling the different parts of the implant, which may be of different materials.

Specifically, the main idea is to design an auxetic shell which has the same configuration and architecture of the ligament-based planar rotating metamaterials (see Section 5.3), connected to the removable part made of PEEK (see Figure 60).

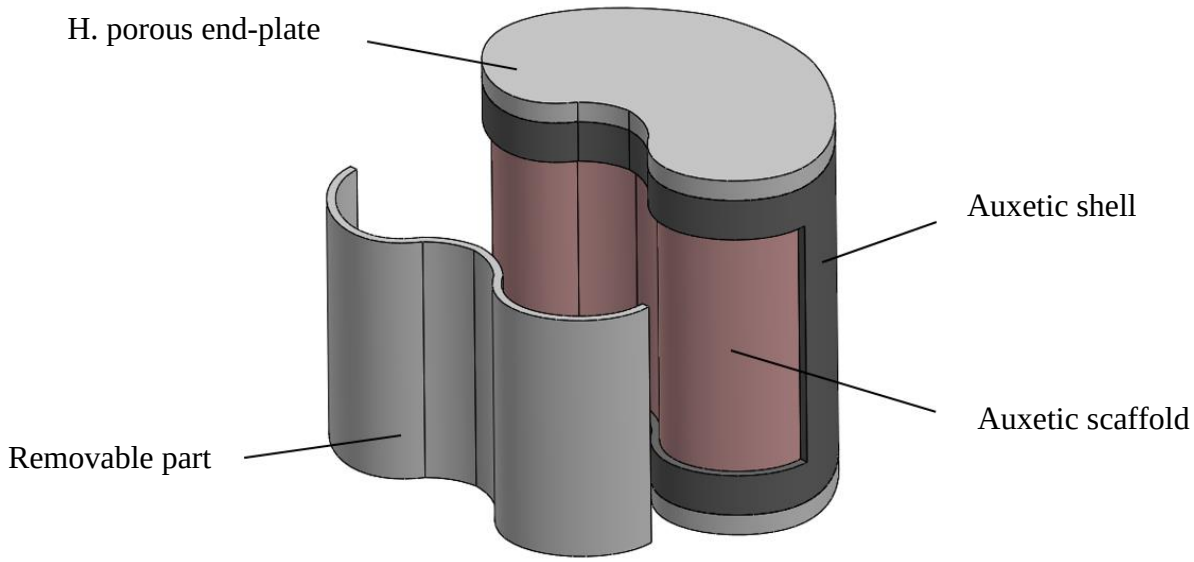

Figure 60 Schematic of the vertebral implant.

In this sense, the additional auxetic structure (i.e. the shell) can be created by oval-shaped tubular system arranged in the way to accomplish the natural form of the vertebral bone.

The great advantages of the use of a tubular axetic system are:

- Accomplish the same deformation behavior of the internal scaffold of the prosthesis;
- Promote the tissue regeneration;
- Prevents any contact between the prosthesis and the spinal cord.

In addition, the use of the PEEK can simultaneously reduce the costs, and increase the radiographic properties of the implant that allow surgeons to monitor possible migration of the implant and presence of reoccurrences.

Then, the fatigue behavior of the proposed auxetic meta-biomaterial should, therefore, be studied as well [130, 131].

These research activities are under development.

9 CONCLUSIONS

The thesis investigated a novel titanium lattice structure for vertebral prosthetics with advanced functionalities in case of total vertebral body replacement (VBR).

In order to avoid the major limitations of the actual trabecular scaffolds, the work designs, optimizes and experimentally validates a new generation of 3D printed titanium lattice structure by exploiting the unusual properties of auxetic metamaterials.

Specifically, we rationally design an innovative meta-biomaterial that consists of a high porous auxetic rotating cubes geometry with the aim of developing a minimally invasive vertebral prosthetics which mimic the cancellous bone behavior.

The structural design of this scaffold is based on a robust conceptual design process, which considers the most critical factors of the vertebral body resection and major complications associated to the implantation and the manufacturing of general vertebral prosthetics.

Modelling and optimization of the lattice structure were carried out by employing 2D and 3D finite element (FE) model of the auxetic configurations by combining different bio-inspired geometries of the system.

The numerical optimization identified some peculiar configurations of the auxetic lattice structure that can reduce the maximum stresses for global strains up to 3%.

Finally, we additively manufactured a prototype of the proposed meta-biomaterials in titanium alloy (Ti6Al4V ELI) through the SLM 3D-printing technique and mechanical testing was performed.

The experimental results confirmed the numerical predictions in terms of Poisson's ratio and elastic properties of the lattice structure for high values of porosity.

The proposed solution could potentially improve implant longevity compared with the actual VBR lattice structures from the literature, and preventing lowering stress-shielding and unexpected collapse of 3D-printed implants.

REFERENCES

[1] Riaz S, Fox R, Lavoie M V., et al. Vertebral body reconstruction for thoracolumbar spinal metastasis--a review of techniques. *Journal of Ayub Medical College, Abbottabad : JAMC* 2006; 18: 70–77.

[2] Alvarez K, Nakajima H. Metallic Scaffolds for Bone Regeneration. 2009; 790–832.

[3] Burnard JL, Parr WCH, Choy WJ, et al. 3D - printed spine surgery implants : a systematic review of the efficacy and clinical safety profile of patient - specific and off - the - shelf devices. 2020; 1248–1260.

[4] Singh R, Lee PD, Dashwood RJ, et al. Titanium foams for biomedical applications : a review. 2010; 25: 127–136.

[5] Challis VJ, Xu X, Zhang LC, et al. High specific strength and stiffness structures produced using selective laser melting. *Materials and Design* 2014; 63: 783–788.

[6] Parthasarathy J, Starly B, Raman S, et al. Mechanical evaluation of porous titanium (Ti6Al4V) structures with electron beam melting (EBM). *Journal of the Mechanical Behavior of Biomedical Materials* 2010; 3: 249–259.

[7] Abd-el-barr AVMM. Initial experience with the use of an expandable titanium cage as a vertebral body replacement in patients with tumors of the spinal column : a report of 95 patients. 2012; 84–92.

[8] Hussein A, Hao L, Yan C, et al. Journal of Materials Processing Technology Advanced lattice support structures for metal additive manufacturing. *Journal of Materials Processing Tech* 2013; 213: 1019–1026.

[9] Cheng XY, Li SJ, Murr LE, et al. Compression deformation behavior of Ti – 6Al – 4V alloy with cellular structures fabricated by electron beam melting. 2012; 16: 153–162.

[10] Campoli G, Borleffs MS, Yavari SA, et al. Materia ls and Design Mechanical properties of open-cell metallic biomaterials manufactured using additive manufacturing. *Materials and Design* 2013; 49: 957–965.

[11] de Jonge CP, Kolken HMA, Zadpoor AA. Non-auxetic mechanical metamaterials. *Materials*; 12. Epub ahead of print 2019. DOI: 10.3390/ma12040635.

[12] Cuadrado A, Yánez A, Martel O, et al. In fl uence of load orientation and of types of loads on the mechanical properties of porous Ti6Al4V biomaterials. *Materials & Design* 2017; 135: 309–318.

[13] Yánez A, Cuadrado A, Martel O, et al. Gyroid porous titanium structures : A versatile solution to be used as scaffolds in bone defect reconstruction. *Materials & Design* 2018; 140: 21–29.

[14] Yánez A, Herrera A, Martel O, et al. Compressive behaviour of gyroid lattice structures for human cancellous bone implant applications. *Materials Science & Engineering C* 2016; 68: 445–448.

[15] Yan C, Hao L, Hussein A, et al. Advanced lightweight 316L stainless steel cellular lattice structures fabricated via selective laser melting. *Materials and Design* 2014; 55: 533–541.

[16] Niinomi M, Nakai M. Titanium-Based Biomaterials for Preventing Stress Shielding between

Implant Devices and Bone. 2011. Epub ahead of print 2011. DOI: 10.1155/2011/836587.

[17] Provaggi E, Leong JJH, Kalaskar DM. Applications of 3D printing in the management of severe spinal conditions. Epub ahead of print 2016. DOI: 10.1177/0954411916667761.

[18] Liu S, Shin YC. Additive manufacturing of Ti6Al4V alloy : A review. *Materials & Design* 2019; 164: 107552.

[19] Masri F El, Brosses ES De, Rhissassi K, et al. Computer Methods in Biomechanics and Biomedical Engineering Apparent Young ' s modulus of vertebral cortico- cancellous bone specimens. 5842. Epub ahead of print 2012. DOI: 10.1080/10255842.2011.565751.

[20] White A. Clinical biomechanics of the spine. *Clinical Biomechanics of the Spine*, https://ci.nii.ac.jp/naid/10015787446/en/ (1990).

[21] An Y, Draughn R. *Mechanical Testing of Bone and the Bone–Implant Interface*. 2000. Epub ahead of print 2000. DOI: 10.1201/9781420073560.

[22] Bell GH, Dunbar O, Beck JS, et al. Variations in strength of vertebrae with age and their relation to osteoporosis. *Calcified Tissue Research* 1967; 1: 75–86.

[23] Keaveny TM, Buckley JM. Chapter 4 - Biomechanics of Vertebral Bone. In: Kurtz SM, Edidin AA (eds) *Spine Technology Handbook*. Burlington: Academic Press, pp. 63–98.

[24] Rockoff SD, Sweet E, Bleustein J. The relative contribution of trabecular and cortical bone to the strength of human lumbar vertebrae. *Calcified Tissue Research* 1969; 3: 163–175.

[25] Silva MJ, Keaveny TM, Hayes WC. Load sharing between the shell and centrum in the lumbar vertebral body. *Spine* 1997; 22: 140–150.

[26] Homminga J, Weinans H, Gowin W, et al. Osteoporosis changes the amount of vertebral trabecular bone at risk of fracture but not the vertebral load distribution. *Spine* 2001; 26: 1555–1560.

[27] Koch J. The Laws of Bone Architecture. *American Journal of Anatomy* 2005; 21: 177–298.

[28] Hansonn T, Keller T, Panjabi MM. A Study of the Compressive Properties of Lumbar Vertebral Trabeculae: Effects of Tissue Characteristics. *Spine*; 12, https://journals.lww.com/spinejournal/Fulltext/1987/01000/A_Study_of_the_Compressive_Properties_of_Lumbar.11.aspx (1987).

[29] Kopperdahl DL, Keaveny TM. Yield strain behavior of trabecular bone. *Journal of Biomechanics* 1998; 31: 601–608.

[30] Rho J. Mechanical properties and the hierarchical structure of bone. 1998; 20: 92–102.

[31] Dequeker J, Perre G Van Der, Jones R, et al. Structural and material mechanical properties of human vertebral cancellous bone. 1997; 19: 729–737.

[32] Lavecchia CE, Espino DM, Moerman KM, et al. Lumbar model generator: A tool for the automated generation of a parametric scalable model of the lumbar spine. *Journal of the Royal Society Interface*; 15. Epub ahead of print 2018. DOI: 10.1098/rsif.2017.0829.

[33] Reilly DT, Burstein AH, Frankel VH. The elastic modulus for bone. *Journal of Biomechanics* 1974; 7: 271–275.

[34] Burstein AH, Reilly DT, Martens M. Aging of bone tissue: mechanical properties. *JBJS*; 58,

https://journals.lww.com/jbjsjournal/Fulltext/1976/58010/Aging_of_bone_tissue__mechanical_properties.15.aspx (1976).

[35] Dreischarf M, Shirazi-Adl A, Arjmand N, et al. Estimation of loads on human lumbar spine: A review of in vivo and computational model studies. *Journal of Biomechanics* 2016; 49: 833–845.

[36] Nachensom A, Morris JM. in Vivo Measurements of Intradiscal Pressure. Discometry, a Method for the Determination of Pressure in the Lower Lumbar Discs. *The Journal of bone and joint surgery American volume* 1964; 46: 1077–1092.

[37] Rohlmann A, Dreischarf M, Zander T, et al. Monitoring the load on a telemeterised vertebral body replacement for a period of up to 65 months. *European Spine Journal* 2013; 22: 2575–2581.

[38] Rajaee MA, Arjmand N, Shirazi-Adl A, et al. Comparative evaluation of six quantitative lifting tools to estimate spine loads during static activities. *Applied Ergonomics* 2015; 48: 22–32.

[39] Stokes IAF, Gardner-Morse M. Lumbar spinal muscle activation synergies predicted by multi-criteria cost function. *Journal of Biomechanics* 2001; 34: 733–740.

[40] Merryweather AS, Loertscher MC, Bloswick DS. A revised back compressive force estimation model for ergonomic evaluation of lifting tasks. *Work* 2009; 34: 263–272.

[41] Han KS, Rohlmann A, Zander T, et al. Lumbar spinal loads vary with body height and weight. *Medical Engineering and Physics* 2013; 35: 969–977.

[42] Buttermann GR, Freeman AL, Beaubien BP. In vitro biomechanics of an expandable vertebral body replacement with self-adjusting end plates. *Spine Journal* 2010; 10: 1024–1031.

[43] Trieb K, Koch S. Failure of an expandable cage-plate cervical vertebral body replacement: Case report of a device related complication. *Eklem Hastaliklari ve Cerrahisi* 2017; 28: 214–218.

[44] Fourney DR, Abi-Said D, Rhines LD, et al. Simultaneous anterior-posterior approach to the thoracic and lumbar spine for the radical resection of tumors followed by reconstruction and stabilization. *Journal of neurosurgery* 2001; 94: 232–244.

[45] W MM, L SR. *Box cage for intervertebral body fusion*, http://europepmc.org/patents/PAT/US6159245%0Ahttps://www.surechembl.org/document/US-6159245-A%0Ahttp://v3.espacenet.com/textdoc?DB=EPODOC&amp%0AIDX=US6159245 (1999).

[46] Jain P, Rana M, Biswas JK, et al. Biomechanics of spinal implants-a review. *Biomedical Physics and Engineering Express*; 6. Epub ahead of print 2020. DOI: 10.1088/2057-1976/ab9dd2.

[47] Girolami M, Boriani S, Bandiera S, et al. Biomimetic 3D-printed custom-made prosthesis for anterior column reconstruction in the thoracolumbar spine: a tailored option following en bloc resection for spinal tumors: Preliminary results on a case-series of 13 patients. *European Spine Journal* 2018; 27: 3073–3083.

[48] Lange U. Anterior vertebral body replacement with a titanium implant of adjustable height : a prospective clinical study. 2007; 161–172.

[49] Arts MP, Peul WC. Vertebral body replacement systems with expandable cages in the

treatment of various spinal pathologies: A prospectively followed case series of 60 patients. *Neurosurgery* 2008; 63: 537–544.

[50] Ernstberger T, Kögel M, König F, et al. Expandable vertebral body replacement in patients with thoracolumbar spine tumors. *Archives of Orthopaedic and Trauma Surgery* 2005; 125: 660–669.

[51] Glennie RA, Rampersaud YR, Boriani S, et al. A Systematic Review With Consensus Expert Opinion of Best Reconstructive Techniques After Osseous En Bloc Spinal Column Tumor Resection. *Spine* 2016; 41 Suppl 2: S205–S211.

[52] Kluba T, Giehl JP. Distractible vertebral body replacement in patients with malignant vertebral destruction or osteoporotic burst fractures. *International Orthopaedics* 2004; 28: 106–109.

[53] Etrick ANTP, Uketich JADL. M Inimally I Nvasive E Sophagectomy. *Construction* 1913; 61: 798–809.

[54] Sattler M, Goesling T, Busche M, et al. Secondary collapse of an expandable cage after vertebral corpectomy. *European Journal of Trauma and Emergency Surgery* 2007; 33: 659–661.

[55] Mohammad-shahi MH, Nikolaou VS. The Effect of Angular Mismatch Between Vertebral Endplate and Vertebral Body Replacement Endplate on Implant Subsidence. 2013; 26: 268–273.

[56] Uchida K, Kobayashi S, Matsuzaki M, et al. Anterior versus posterior surgery for osteoporotic vertebral collapse with neurological deficit in the thoracolumbar spine. *European spine journal : official publication of the European Spine Society, the European Spinal Deformity Society, and the European Section of the Cervical Spine Research Society* 2006; 15: 1759–1767.

[57] Uchida K, Kobayashi S, Nakajima H, et al. Anterior expandable strut cage replacement for osteoporotic thoracolumbar vertebral collapse. *Journal of neurosurgery Spine* 2006; 4: 454–462.

[58] Chen PQ, Lin SJ, Wu SS, et al. Mechanical performance of the new posterior spinal implant: Effect of materials, connecting plate, and pedicle screw design. *Spine* 2003; 28: 881–886.

[59] Kovacl H, Yetim AF, Çelik A. Biomechanical analysis of spinal implants with different rod diameters under static and fatigue loads: An experimental study. *Biomedizinische Technik* 2019; 64: 339–346.

[60] Lucas GL, Cooke FW, Friis EA. Stress Shielding of Bone BT - A Primer of Biomechanics. In: Lucas GL, Cooke FW, Friis EA (eds). New York, NY: Springer New York, pp. 79–88.

[61] Warburton A, Girdler SJ, Mikhail CM, et al. Biomaterials in spinal implants: A review. *Neurospine* 2020; 17: 101–110.

[62] Dobbs MB, Lenke LG, Kim YJ, et al. Anterior/posterior spinal instrumentation versus posterior instrumentation alone for the treatment of adolescent idiopathic scoliotic curves more than 90 degrees. *Spine* 2006; 31: 2386–2391.

[63] Vadapalli S, Sairyo K, Goel VK, et al. Biomechanical rationale for using polyetheretherketone (PEEK) spacers for lumbar interbody fusion-A finite element study. *Spine* 2006; 31: E992-8.

[64] Martelli N, Serrano C, van den Brink H, et al. Advantages and disadvantages of 3-dimensional

printing in surgery: A systematic review. *Surgery* 2016; 159: 1485–1500.

[65] Lee Ventola C. Medical applications for 3D printing: Current and projected uses. *P and T* 2014; 39: 704–711.

[66] Liebsch C, Aleinikov V, Kerimbayev T, et al. In vitro comparison of personalized 3D printed versus standard expandable titanium vertebral body replacement implants in the mid-thoracic spine using entire rib cage specimens. *Clinical Biomechanics* 2020; 78: 105070.

[67] Ngo TD, Kashani A, Imbalzano G, et al. Additive manufacturing (3D printing): A review of materials, methods, applications and challenges. *Composites Part B: Engineering* 2018; 143: 172–196.

[68] Ernstberger ST. Expandable vertebral body replacement in patients with thoracolumbar spine tumors. 2005; 660–669.

[69] Hasegawa K, Abe M, Washio T, et al. An Experimental Study on the Interface Strength Between Titanium Mesh Cage and Vertebra in Reference to Vertebral Bone Mineral Density. 2001; 26: 957–963.

[70] Lange U, Bastian L. Three-dimensional motion analysis with Synex Comparative biomechanical test series. 2000; 472–485.

[71] Surgery N, Francisco CS. Adjacent-level vertebral body fractures after expandable cage reconstruction. 2008; 8: 584–588.

[72] Brenke C, Fischer S, Carolus A, et al. Complications associated with cervical vertebral body replacement with expandable titanium cages. *Journal of Clinical Neuroscience* 2016; 32: 35–40.

[73] Deml MC, Mazuret Sepulveda CA, Albers CE, et al. Anterior column reconstruction of the thoracolumbar spine with a new modular PEEK vertebral body replacement device: retrospective clinical and radiologic cohort analysis of 48 cases with 1.7-years follow-up. *European Spine Journal*. Epub ahead of print 2020. DOI: 10.1007/s00586-020-06464-x.

[74] Raslan F, Koehler S, Berg F, et al. Vertebral body replacement with PEEK-cages after anterior corpectomy in multilevel cervical spinal stenosis: a clinical and radiological evaluation. *Archives of Orthopaedic and Trauma Surgery* 2014; 134: 611–618.

[75] Boriani S, Bandiera S. Clinical experience about stackable carbon- fiber prosthetic replacement of vertebral bodies (115 implants on 114 patients).

[76] Herrera A, Yánez A, Martel O, et al. Computational study and experimental validation of porous structures fabricated by electron beam melting : A challenge to avoid stress shielding. *Materials Science & Engineering C* 2014; 45: 89–93.

[77] Kadkhodapour J, Montazerian H, Darabi AC, et al. Failure mechanisms of additively manufactured porous biomaterials : Effects of porosity and type of unit cell. *Journal of the Mechanical Behavior of Biomedical Materials* 2015; 50: 180–191.

[78] Ullman D. The Mechanical Design Process. 1992.

[79] Dragoni E, Mammano GS, Esculapio SE. *Lezioni di Progetto di Sistemi Meccatronici*. Esculapio, https://books.google.it/books?id=lN05BAAAQBAJ (2013).

[80] Ledoux Y, Mesnard M, Sandoval JAP, et al. Optimization of a Dynamic Intervertebral Lumbar

Implant. *Procedia CIRP* 2016; 50: 192–197.

[81] Polikeit A, Ferguson SJ, Nolte LP, et al. Factors influencing stresses in the lumbar spine after the insertion of intervertebral cages: Finite element analysis. *European Spine Journal* 2003; 12: 413–420.

[82] Hogan JM. Chapter 15 - FDA Regulation of Spinal Implants. In: Kurtz SM, Edidin AA (eds) *Spine Technology Handbook*. Burlington: Academic Press, pp. 473–508.

[83] Evans KE, Nkansah MA, Hutchinson IJ, et al. Molecular network design [7]. *Nature* 1991; 353: 124.

[84] Ren X, Das R, Tran P, et al. Auxetic metamaterials and structures: A review. *Smart Materials and Structures*; 27. Epub ahead of print 2018. DOI: 10.1088/1361-665X/aaa61c.

[85] Lakes R. Deformation mechanisms in negative Poisson's ratio materials: structural aspects. *Journal of Materials Science* 1991; 26: 2287–2292.

[86] Wojciechowski KW. Two-dimensional isotropic system with a negative poisson ratio. *Physics Letters A* 1989; 137: 60–64.

[87] Lakes R. Foam Structures with a Negative Poisson's Ratio. *Science* 1987; 235: 1038–1040.

[88] Choi JB, Lakes RS. Non-linear properties of metallic cellular materials with a negative Poisson's ratio. *Journal of Materials Science* 1992; 27: 5375–5381.

[89] Argatov II, Guinovart-Díaz R, Sabina FJ. On local indentation and impact compliance of isotropic auxetic materials from the continuum mechanics viewpoint. *International Journal of Engineering Science* 2012; 54: 42–57.

[90] Scarpa F, Giacomin JA, Bezazi A, et al. Dynamic behavior and damping capacity of auxetic foam pads. *Smart Structures and Materials 2006: Damping and Isolation* 2006; 6169: 61690T.

[91] Evans KE. Auxetic polymers: a new range of materials. *Endeavour* 1991; 15: 170–174.

[92] Hou W, Yang X, Zhang W, et al. Design of energy-dissipating structure with functionally graded auxetic cellular material. *International Journal of Crashworthiness* 2018; 23: 366–376.

[93] Choi JB. Fracture toughness of re-entrant foam materials with a negative Poisson's ratio: Experiment and analysis. *International Journal of Fracture* 1996; 80: 73–83.

[94] Scarpa F, Ciffo LG, Yates JR. Dynamic properties of high structural integrity auxetic open cell foam. *Smart Materials and Structures* 2004; 13: 49–56.

[95] Panico M, Langella C, Santulli C. Development of a Biomedical Neckbrace through Tailored Auxetic Shapes. *Italian Journal of Science & Engineering* 2017; 1: 105–117.

[96] Kapnisi M, Mansfield C, Marijon C, et al. Auxetic Cardiac Patches with Tunable Mechanical and Conductive Properties toward Treating Myocardial Infarction. *Advanced Functional Materials*; 28. Epub ahead of print 2018. DOI: 10.1002/adfm.201800618.

[97] Duncan O, Shepherd T, Moroney C, et al. Review of auxetic materials for sports applications: Expanding options in comfort and protection. *Applied Sciences (Switzerland)*; 8. Epub ahead of print 2018. DOI: 10.3390/app8060941.

[98] Li Q, Kuang Y, Zhu M. Auxetic piezoelectric energy harvesters for increased electric power output. *AIP Advances*; 7. Epub ahead of print 2017. DOI: 10.1063/1.4974310.

[99] Kolken HMA, Zadpoor AA. Auxetic mechanical metamaterials. *RSC Advances* 2017; 7: 5111–5129.

[100] Yang L, Harrysson O, West H, et al. Compressive properties of Ti-6Al-4V auxetic mesh structures made by electron beam melting. *Acta Materialia* 2012; 60: 3370–3379.

[101] Warmuth F, Osmanlic F, Adler L, et al. Fabrication and characterisation of a fully auxetic 3D lattice structure via selective electron beam melting. *Smart Materials and Structures*; 26. Epub ahead of print 2017. DOI: 10.1088/1361-665X/26/2/025013.

[102] Mitschke H, Schwerdtfeger J, Schury F, et al. Finding auxetic frameworks in periodic tessellations. *Advanced Materials* 2011; 23: 2669–2674.

[103] Grima JN, Evans KE. Auxetic behavior from rotating squares. *Journal of Materials Science Letters* 2000; 19: 1563–1565.

[104] Slann A, White W, Scarpa F, et al. Cellular plates with auxetic rectangular perforations. *Physica Status Solidi (B) Basic Research* 2015; 252: 1533–1539.

[105] Wang G, Sun S, Li M, et al. Large deformation shape optimization of cut-mediated soft mechanical metamaterials. *Materials Research Express*; 6. Epub ahead of print 2019. DOI: 10.1088/2053-1591/aaeabc.

[106] Attard D, Grima J. A three-dimensional rotating rigid units network exhibiting negative Poisson's ratios. *physica status solidi (b)*; 249. Epub ahead of print July 1, 2012. DOI: 10.1002/pssb.201084223.

[107] Rueger Z, Ha CS, Lakes RS. Flexible Cube Tilt Lattice with Anisotropic Cosserat Effects and Negative Poisson's Ratio. *Physica Status Solidi (B) Basic Research* 2019; 256: 1–6.

[108] Sorrentino A, Castagnetti D, Spaggiari A, et al. Shape optimization of the fillet under a bolt's head. *Journal of Strain Analysis for Engineering Design* 2019; 54: 247–253.

[109] Pedersen NL. Overall bolt stress optimization. *Journal of Strain Analysis for Engineering Design*. Epub ahead of print 2013. DOI: 10.1177/0309324712470233.

[110] Smith M. *ABAQUS/Standard User's Manual, Version 6.9*. United States: Dassault Systèmes Simulia Corp, 2009.

[111] Rafi HK, Karthik N V., Gong H, et al. Microstructures and mechanical properties of Ti6Al4V parts fabricated by selective laser melting and electron beam melting. *Journal of Materials Engineering and Performance* 2013; 22: 3872–3883.

[112] Poźniak AA, Wojciechowski KW, Grima JN, et al. Planar auxeticity from elliptic inclusions. *Composites Part B: Engineering* 2016; 94: 379–388.

[113] Mizzi L, Attard D, Gatt R, et al. Implementation of periodic boundary conditions for loading of mechanical metamaterials and other complex geometric microstructures using finite element analysis. *Engineering with Computers*. Epub ahead of print 2020. DOI: 10.1007/s00366-019-00910-1.

[114] Mirjalili S. Particle swarm optimisation. *Studies in Computational Intelligence* 2019; 780: 15–31.

[115] Vanderplaats Research Development. VisualDOC 8.0.

[116] Van Rossum G, Drake Jr FL. *Python reference manual*. Centrum voor Wiskunde en Informatica Amsterdam, 1995.

[117] Grima JN, Alderson A, Evans KE. Auxetic behaviour from rotating rigid units. *Physica Status Solidi (B) Basic Research* 2005; 242: 561–575.

[118] Grima JN, Zammit V, Gatt R, et al. Auxetic behaviour from rotating semi-rigid units. *Physica Status Solidi (B) Basic Research* 2007; 244: 866–882.

[119] Sorrentino A, Castagnetti D, Mizzi L, et al. Rotating squares auxetic metamaterials with improved strain tolerance. *Smart Materials and Structures*, http://iopscience.iop.org/article/10.1088/1361-665X/abde50 (2021).

[120] Mizzi L, Salvati E, Spaggiari A, et al. Highly stretchable two-dimensional auxetic metamaterial sheets fabricated via direct-laser cutting. *International Journal of Mechanical Sciences* 2020; 167: 105242.

[121] Taylor D, Kelly A, Toso M, et al. The variable-radius notch: Two new methods for reducing stress concentration. *Engineering Failure Analysis* 2011; 18: 1009–1017.

[122] Mattheck C, Burkhardt S. A new method of structural shape optimization based on biological growth. *International Journal of Fatigue* 1990; 12: 185–190.

[123] Mattheck C. Teacher tree: The evolution of notch shape optimization from complex to simple. *Engineering Fracture Mechanics* 2006; 73: 1732–1742.

[124] Andrade C, HA CS, Lakes RS. Extreme cosserat elastic cube structure with large magnitude of negative CPoisson's ratio. 13.

[125] Kim J, Shin D, Yoo DS, et al. Structures with polygonal prisms for three-dimensional auxetic behaviour. *Proceedings of the Royal Society A: Mathematical, Physical and Engineering Sciences*; 473. Epub ahead of print 2017. DOI: 10.6084/m9.figshare.c.3790000.

[126] Standard I. INTERNATIONAL STANDARD Mechanical testing of metals —Ductility testing —Compression test for porous and cellular metals. *International Standard*; ISO 13314.

[127] Rueden CT, Schindelin J, Hiner MC, et al. ImageJ2: ImageJ for the next generation of scientific image data. *BMC Bioinformatics* 2017; 18: 1–26.

[128] Kolken HMA, Janbaz S, Leeflang SMA, et al. Rationally designed meta-implants: A combination of auxetic and conventional meta-biomaterials. *Materials Horizons* 2018; 5: 28–35.

[129] Method ST. Standard Test Method for Young ' s Modulus , Tangent Modulus , and Chord Modulus 1. *Practice* 1981; 03: 1–7.

[130] Taylor D. The Theory of Critical Distances BT - Fracture of Nano and Engineering Materials and Structures. In: Gdoutos EE (ed). Dordrecht: Springer Netherlands, 2006, pp. 1095–1096.

[131] Zadpoor AA. Mechanics of additively manufactured biomaterials. *Journal of the Mechanical Behavior of Biomedical Materials* 2017; 70: 1–6.

ANNEX

Some of the results reported in the present dissertation were published on peer-reviewed journals or presented at national and international conferences.
A list of the publications produced during the three-years period of Ph.D. is reported below.

- **Shape optimization of the fillet under a bolt's head**
  A. Sorrentino, D. Castagnetti, A. Spaggiari, E. Dragoni
  Journal of Strain Analysis and Design, 2019.

- **Modellazione, prototipazione e convalida sperimentale di un nuovo microfono basato su film di PVDF**
  A. Sorrentino
  Memoria in atti di convegno AIAS, 2019.

- **Experimental and numerical analysis of a liquid aluminium injector for an Al-H_2O based hydrogen production system**
  M. Milani, L. Montorsi, G. Storchi *et al*.
  International Journal of Thermofluids, 2020.

- **Instabilità di pull-in per pinze in nano-tubi di carbonio: formulazione analitica e convalida sperimentale di macro modelli**
  G. Bianchi, A. Sorrentino
  Memoria in atti di convegno AIAS, 2020.

- **Experimental characterization of pull-in parameters of an electrostatically actuated cantilever beam**
  A. Sorrentino, G. Bianchi, D. Castagnetti, E. Radi
  Applications in Engineering Science, 2020.

- **Design and fabrication of a pillar-based piezoelectric microphone exploiting 3D-printing technology**

  Y. Ricci, A. Sorrentino, P. La Torraca *et al.*

  IEEE Sensors Letters, 2021.

- **Rotating square auxetic metamaterials with improved strain tolerance**

  A. Sorrentino, D. Castagnetti, L. Mizzi, A. Spaggiari

  Smart Materials and Structures, 2021.

This page intentionally left blank

ACKNOWLEGDMENTS

A tutte persone che mi vogliono bene, grazie.

Grazie al *Prof. Eugenio Dragoni* e al *Prof. Andrea Spaggiari* per tutto ciò che sono riuscito ad apprendere stando al vostro fianco.
Mi avete sempre fatto sentire un bravo ingegnere.

Grazie *Fulvia* ed *Enrico* per aver contribuito a realizzare questo progetto.
Grazie per la vostra gentilezza.

Grazie *Luke* per quello che abbiamo fatto insieme.

Grazie *Calogero* e *Michele*, grazie *Giovanni*.

Grazie a tutte le persone con le quali ho avuto il piacere di lavorare durante questi ultimi tre anni.

Un doveroso grazie va anche ad *Andrea Pasquali* e al team di *Zare Prototipi* che mi hanno permesso di concludere al meglio tale attività di ricerca.

Ma soprattutto, grazie *Davide*.
Grazie per il tuo supporto in ogni nostra attività.
Grazie per i tuoi insegnamenti e per il metodo di lavoro che mi hai trasmesso.
Grazie per il tuo rigore scientifico.
Grazie per la tua sincerità e per l'atteggiamento sempre propositivo che hai messo in campo dinanzi ad ogni ostacolo che ho incontrato.

Grazie a tutte le persone che mi hanno accompagnato durante quest'incredibile viaggio.
Grazie per l'affetto e la fiducia che mi avete donato.

Grazie *AJ* e *Maru*, siete il "premio" più bello.